

CONCEPTUAL DESIGN REPORT

# Online Time-of-Flight Photoemission Spectrometer for X-Ray Photon Diagnostics

June 2012

*Jens Buck*

*Work Package 74: X-Ray Photon Diagnostics,  
European XFEL Project*

European X-Ray Free-Electron Laser Facility GmbH

Albert-Einstein-Ring 19

22761 Hamburg

Germany



---

# Contents

<b>1</b>	<b>Introduction.....</b>	<b>6</b>
<b>2</b>	<b>Physical foundations .....</b>	<b>10</b>
	2.1 Photoionization of gases .....	10
	2.2 Time-of-flight spectroscopy of photoelectrons.....	17
	2.3 Impact on technical design.....	21
<b>3</b>	<b>System design .....</b>	<b>26</b>
	3.1 Flight tube.....	26
	3.2 Detector unit .....	32
	3.3 Array of flight tubes.....	34
	3.4 Gas injection system .....	38
	3.5 Vacuum system.....	44
	3.6 Compensation of external magnetic fields .....	49
	3.7 Integration into the facility .....	52
	3.8 Strategies and procedures for design optimization .....	57
	3.9 Digitizer and online data processing.....	60
	3.10 Breakdown structure of subsystems and automation.....	71
	3.11 Calibration procedure and planned commissioning.....	75
<b>4</b>	<b>Feasibility.....</b>	<b>82</b>
	4.1 Simulations of the time-of-flight spectrometer.....	82
	4.2 Simulations of space charge .....	94
	4.3 Simulation of data reduction .....	99
	4.4 Polarization analysis.....	102
<b>5</b>	<b>Safety implications .....</b>	<b>110</b>
	5.1 Human safety .....	110
	5.2 Machine protection system.....	111
<b>6</b>	<b>Interfaces to other work packages.....</b>	<b>117</b>
	6.1 DAQ and Control (WP-76) .....	117
	6.2 X-Ray Optics and Transport (WP-73).....	119
	6.3 Detector design (WP-75).....	119
	6.4 Machine status information (Section 3.10) .....	120
	6.5 Accelerator control .....	120

<b>Appendix .....</b>	<b>122</b>
<b>A    Physical reference data .....</b>	<b>122</b>
<b>B    Symbols used in vacuum technology .....</b>	<b>125</b>
<b>C    List of abbreviations.....</b>	<b>126</b>
<b>Bibliography.....</b>	<b>128</b>
<b>Acknowledgement.....</b>	<b>136</b>

---

# Contents



# 1 Introduction

The European X-Ray Free-Electron Laser (XFEL.EU) project is organized in work packages for specific tasks during the construction phase. Work package 74 (“WP-74: X-Ray Photon Diagnostics”) is responsible for the development of a number of devices for the diagnostics of photon beam properties at the future XFEL.EU [1]. According to their foreseen use case and resulting specifications, they can be grouped into smaller sets of related devices. Ref. [37] gives a more general overview of the structure of WP-74. The electron time-of-flight (ToF) spectrometer we introduce in this document is a contribution to the group of non-invasive, gas-based instrumentation for diagnostics that is intended to support user operation (Figure 1.1). Further developments that fall into this category are the X-ray Gas Monitor Detector (XGMD, [43]) and the X-ray Beam Position Monitor (XBPM, [42]). In the scope of this conceptual design report, we give a general overview of the specifications and foreseen features, followed by more specialized considerations concerning the general role of the device at XFEL.EU.

The main purpose of the planned ToF spectrometer is to determine the spectrum of the FEL radiation produced at the future XFEL.EU facility. As will be shown in this document, the device also provides an excellent capability to probe the polarization of the photon beam. Polarization control at XFEL.EU is currently under consideration [10], so this feature might be of high importance for future upgrades of beamline specifications. Any information gained by the proposed spectrometer will be gained by photoelectron spectroscopy from rare gases. All gas-based devices under development have similar general requirements.

The features and specifications of the spectrometer are as follows:

- **Non-invasive operation**

The spectrometer will operate during regular user operation (“online” device). Since it will be located upstream the user experiments, any perturbations of the photon beam produced by diagnostics must be reduced as much as possible. This demands low absorption and scattering of the beam, as well as low perturbation of the coherent wavefront.

- **Suitability for temporal structure of XFEL.EU radiation**

The planned pulse structure of the XFEL.EU is shown in Figure 1.2: 10 pulse trains with up to 2 700 photon pulses each will be produced with an intra-pulse

train repetition rate of 4.5 MHz. The high brilliance of the photon beam calls for the use of extremely resistant materials in order to avoid damage. Moreover, this has a strong impact on the design of the data acquisition system.

- **Shot-to-shot measurements**

The self-amplified spontaneous emission (SASE) process employed at free-electron laser facilities is a statistical process, which results in random fluctuations of parameters of the produced photon beam, especially of the spectrum. Therefore, the spectroscopic characterization of every individual pulse in a pulse train with up to 2 700 pulses is required.

- **Low response time**

Data obtained from diagnostics will not only act as a reference to the user, but might also provide input to automated components of user experiments and the machine. Generally, a low latency between pulse arrival and availability of the output is highly desirable.

- **Work at every configuration of XFEL.EU**

Different bunch charge and electron energies will be produced in the accelerator of XFEL.EU in order to provide, e.g. different photon pulse durations [27]. Photon energies ranging from 260 eV – 25 keV will be produced in the undulators throughout the facility. Both options strongly influence the achieved photon flux ([29] and Figure A.4). At every working point, diagnostics will have to provide reliable information.

- **Absolute calibration**

Absolute measurements of photon energy are intended for the spectrometer, so calibration issues of the device have high priority.

- **Energy-resolving power  $\Delta E/E \leq 10^{-4}$**

The SASE radiation is expected to have a relative spectral bandwidth of  $10^{-3}$  [29]. Useful information can be obtained from diagnostics only if its resolution clearly exceeds this value. Therefore, the minimum design goal can be defined as an energy resolution of  $10^{-4}$ .

- **Polarization accuracy of 1%**

In case polarization control is implemented, the reasonable accuracy requirement for the direction of the polarization vector was stated to amount to 1% [37].

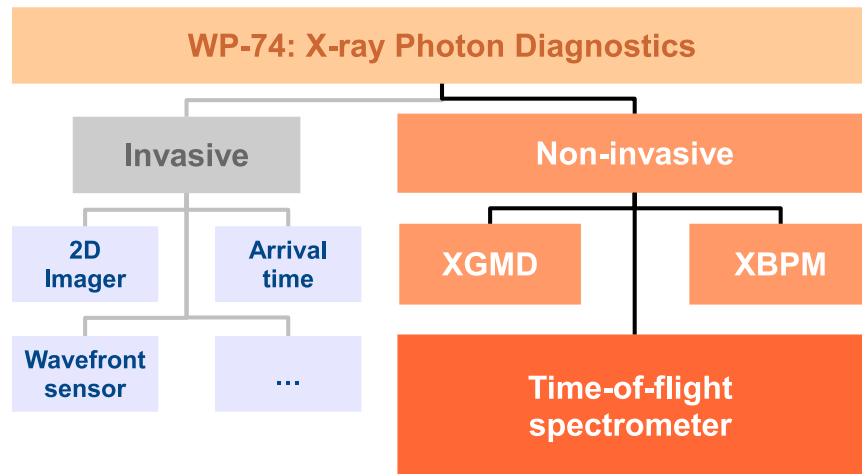


**Figure 1.1:** Work Package 74 (WP-74) of the European XFEL project is responsible for the development of general photon beam diagnostics [37]. Besides the ToF spectrometer introduced in this document, gas-based, non-invasive devices include the XGMD [43] and the XBPM [42].

How the demanded features can be implemented in a device for diagnostics will be discussed throughout this document. Gas-based devices for photon beam diagnostics in general have proven their suitability during operation at free-electron laser facilities such as the “Free-Electron Laser in Hamburg” (FLASH) at DESY. Devices such as the Online Photoionization Spectrometer (OPIS) are still under constant improvement and will also be integrated into the FLASH II upgrade under construction.

The spectrometer design we report here is based on developments by the group of Jens Viefhaus at PETRA III, DESY, who has the responsibility of the P04 beamline at the facility. As will be shown here, the basic design is in general also suitable for application at SASE 3 beamline, and future upgrades developed at XFEL will ensure that diagnostics for SASE 1 and SASE 2 beamlines will also meet the requirements. Prototypes of the design presented here have already been built and optimized for some years, and it has achieved a level of maturity where it can safely be considered for future use at XFEL.EU. The setup has proven its performance during various beamtimes by the P04 group at various synchrotron light sources. It has successfully been applied for scientific studies of the photoemission from rare gases [48] and for general commissioning tasks, such as the calibration of diamond polarizers at the P09 beamline, PETRA III. In both fields, the device demonstrated its excellent angular resolution and the essential feature of a high energy resolution.

In this document, we give an outline of the general technological design of the spectrometer (Chapter 3) and its subsystems as developed earlier and give



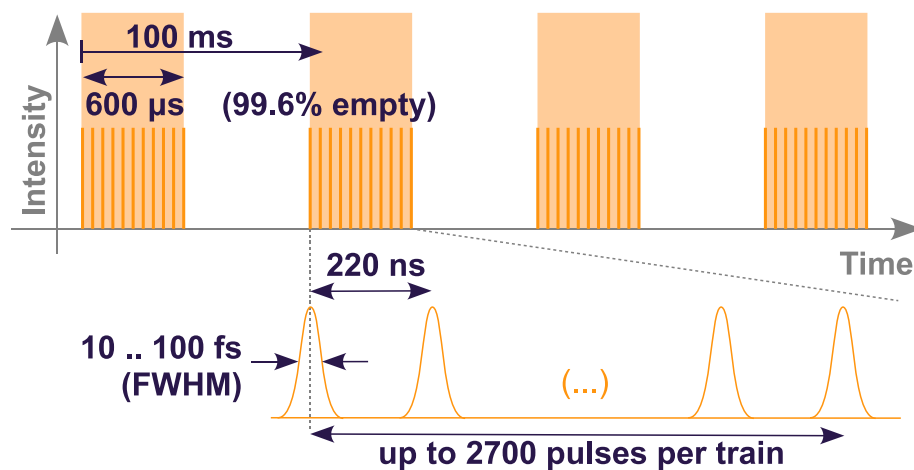


**Figure 1.2:** Schematic pulse structure of the European XFEL according to [1,27].

amendments on specific modifications needed for future use at XFEL.EU. The integration in the facility (Section 3.7) raises general questions such as interfacing (Chapter 6) and safety (Chapter 5), which will be answered according to the current state of planning in the referenced chapters. For some critical points, we present simulations of device performance as expected at XFEL in Chapter 4, which is dedicated to feasibility studies. A general roadmap for future calibration and commissioning procedures related to the spectrometer will be given in Section 3.8.

In general, we summarize the present status of development. For the moment, we are able to contribute specific design options for various details, which will provide a basis for discussions on the final layout. Before going into detail, we provide an introduction to the physical processes exploited in the spectrometer and give an overview of available atomic reference data (Chapter 2). Some details of the design and later operation can already be figured out from atomic physics alone. Details will be discussed in Section 2.3.

---

## 2 Physical foundations

---

### 2.1 Photoionization of gases

Before giving a detailed view at the technical design of the ToF spectrometer in the subsequent chapter, we will outline the relevant physics of photoionization of rare gases and some resulting physical boundary conditions with a relevance to device design. Photoionization is the well-known effect of emission of one electron, the photoelectron, from a bound state in an atom upon absorption of a photon. This effect requires that the photon energy  $h\nu$  exceed the binding energy  $E_B$  of the electron, where the excess energy is transferred to the electron as kinetic energy  $E_{kin}$ :

$$E_{kin} = h\nu - E_B \quad (2.1)$$

Electron binding energies of the atoms are tabulated for every atomic orbital in various (online) resources such as [47, 50]. From Equation 2.1, it becomes clear that the spectral distribution of photon energy is represented by the distribution of kinetic energy, which can be probed by using a photoemission spectrometer.

The probability of absorption of a photon in conjunction with electron emission from a certain electronic state strongly depends on photon energy, the atomic orbital, and the chemical element. This dependency is accounted for by the photoionization cross section  $\sigma$  and can be obtained from literature. A widely used compilation of theoretical cross sections can be found in [46], where the total photoionization cross sections, i.e. the combined cross sections of every subshell, are given. Subshell cross sections are stated only for a small set of light chemical elements with a relevance in astrophysics or for relatively small photon energies from 0–1 500 eV in [46]. For future applications in the field of photon diagnostics at FELs, the precise determination of subshell photoionization cross sections — also for higher photon energies — will be done in a German-Russian collaboration of experimental and theoretical physicists [49]. The tabulated values for the rare gases (from [46]) are shown in Figures A.1 and A.2.

The absorption edges with an abrupt increase of the cross section are located at photon energies where photoemission from an additional electronic state becomes possible (Equation 2.1). The total cross section rapidly decays with increasing energy difference to a bound state, so one can, especially at high photon energy, assume that the process predominantly involves electrons from the innermost available shell and the total cross section is dominated by the subshell cross sections of that shell.

The total amount of photoelectrons created per X-ray pulse is essential for the feasibility of single-shot photoelectron spectroscopy. Here, we give an estimation for the complete range of photon energy for the beamlines SASE 1/2 and SASE 3, taking into account the number of photons per shot as a function of photon energy as simulated by Schneymiller and Yurkov [29] and a realistic partial pressure of a specific rare gas. The number of photoelectrons  $I_0$  created along the beam path in a gas-filled cell per unit length can be written as:

$$I_0 = \frac{N_0 \cdot \sigma \cdot p}{k_B T}, \quad (2.2)$$

where  $N_0$  is the number of photons per pulse,  $\sigma$  is the photoionization cross section, and  $p$  is the partial gas pressure inside the gas cell.

The above-cited reference data applied to Equation 2.2 will be the basis for further estimations of the efficiency of our proposed spectrometer. Here, we considered the highest and lowest estimate of the expected photon number per pulse provided by [29] for different bunch charges. Due to the high variations of photon flux reported there, the expected ionization rate covers many orders of magnitude and becomes very small, especially at very high photon energy and low bunch charge. Since number of detected photoelectrons reflects the size of the statistical sample of the distribution of kinetic energy, statistical noise is expected to limit the experimental precision of the device in extreme cases. In the remaining parts, the signal level can be adjusted to the detector's dynamic range easily by tuning the gas pressure. Here, precise control over several orders of magnitude can be realized without problems. Detailed discussions of the measured signal strength will be given in Section 3.1 and Chapter 4.

For typically  $10^{12}$  photons per pulse, a total cross section of 1 Mb, and a pressure of  $10^{-5}$  mbar,  $\approx 2.4 \cdot 10^7$  photoelectrons are emitted per metre, which is equivalent to an absorption of  $2.4 \cdot 10^{-5} \text{ m}^{-1}$  or an absorption length of  $\lambda = k_B T / (p\sigma) \approx 4 \cdot 10^4 \text{ m}$ .

Since the high-pressure section in the environment of the spectrometer will have a length of approximately one or two metres, the total absorption can be neglected. Therefore, we can safely claim that our design introduces the smallest possible perturbation to the photon beam.

To go into more detail, we will consider the direction dependency of photoemission now. The most common process in photoemission involving a single electron and photon, is usually treated with the so-called dipole approximation (e.g. [58–61], and references therein), from which the angular distribution of photoelectrons is derived. In this scope, the photoelectron distribution is a function of the direction with respect

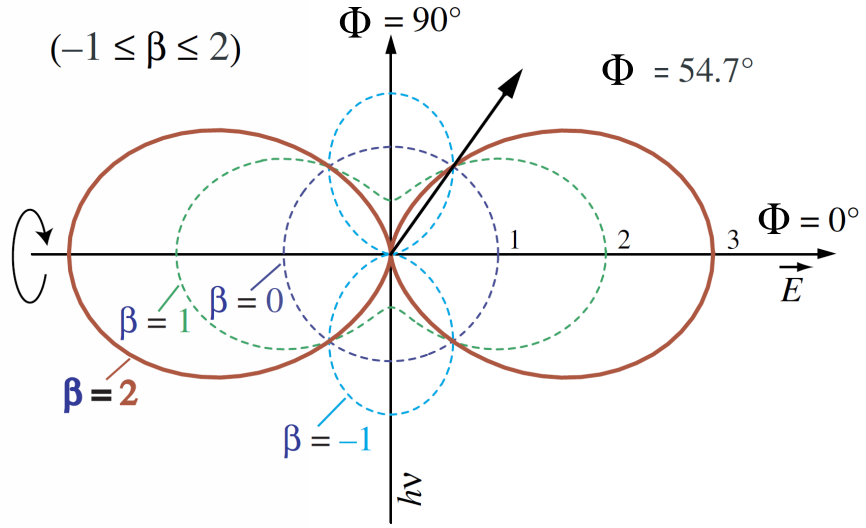


**Figure 2.1:** Transverse angular distribution of photoelectrons as a function of azimuth angle for different values of  $\beta$  (courtesy of J. Viehhaus).

to the direction of linear polarization of the photon beam. The lateral photoelectron distribution, which, in linear regime, is proportional to the lateral intensity of the incident photon beam, is neglected here. For simplicity, we discuss the emission as a function of azimuthal angle in a plane perpendicular to the propagation direction of the photon beam. Here, the angular dependence of emission reads

$$\frac{d\sigma}{d\Omega}(\phi) = \frac{\sigma}{4\pi} \cdot \left( 1 + \frac{\beta}{2} \cdot P_2(\cos(\phi)) \right), \quad (2.3)$$

$$(2.4)$$

$$P_2(x) = 3 \cdot x^2 - 1.$$

$P_2$  is the second Legendre polynomial. For  $\beta > 0$ , maximum emission is found in parallel to the polarization vector (here:  $\phi = 0$ ). Figure 2.1 gives an expression for the fractional cross section, which holds for emission into a certain spatial direction. In the dipole approximation, this distribution is rotational symmetric with respect to the direction of linear polarization. The actually observed photoemission signal is obtained by the integral over a certain solid angle of observation.

The parameter  $\beta$  ( $-1 \leq \beta \leq 2$  in theory), depends on the chemical element, the initial state of the emitted photoelectron (i.e. the atomic orbital) and photon energy.

Tabulated values of  $\beta$  can be found in the literature [45] and are reproduced in Figure A.3. From the reference data, it can be seen that  $\beta > 0$  for any relevant case. As a consequence of Figure 2.1, valuable information on the photon beam can be derived from the angular distribution, namely its direction of polarization. The intention to exploit this effect for diagnostics strongly influences the design of our device (Section 3.3), since it requires to probe the angular dependency of photoemission. The relative intensity for the current geometry is depicted in Figure 2.1 for some exemplary cases. As can be seen from the figure, a determination of the orientation of the polarization vector is possible in principle as long as  $\beta$  is known and different from zero. We find from the references that, as a rule,  $\beta$  is always larger than 0.25 in the relevant energy range, so a reasonable modulation of the measured, angle-resolved intensity can be expected. The observed angular distribution from the absorption of unpolarized or circular polarized light is isotropic. Therefore, at known  $\beta$ , the degree of linear polarization of partially linear polarized light can be determined by analysing the angular intensity modulations. Section 4.4 gives an impression of a suggested method for this task.

Even though recent research projects involving a high-precision, high-resolution determination of  $\beta(h\nu)$  revealed strong, oscillatory deviations from the standard model [48] for specific cases, we can mostly rely on reference data here. Furthermore, a recently founded collaboration [49] aims at providing more precise reference data from experimental data and theoretical models. Ongoing activities of the P04 group at PETRA III will also provide additional experimental reference data. Once a database with all relevant  $\beta$  values is set up, we will be able to apply Figure 2.1 in order to determine the degree and the direction of linear polarization of the photon beam in any SASE beamline. A detailed discussion of the expected performance with an actual electron spectrometer will be given in Section 4.1.

The dipole approximation is known to break down for specific situations which might occur with XFEL.EU radiation. Especially when taking the high photon energy into account, a more sophisticated treatment of the angular distribution will most likely become necessary. In that case, Figure 2.1 is replaced by a more complex expression including not only dipole terms, but also quadrupole terms of the interaction between the photon field and the electronic state (e.g. [58–61]). In this context, the equation for the differential cross section reads

$$\frac{d\sigma}{d\Omega}(\phi, \Theta) = \frac{\sigma}{4\pi} \cdot \left( 1 + \frac{\beta}{2} \cdot P_2(\cos(\phi)) + (\delta + \gamma \cos^2 \Theta) \cdot \sin \Theta \cdot \cos \phi \right). \quad (2.5)$$

In this case, the distribution becomes asymmetric with respect to the azimuthal plane and results in a higher total emission in forward or backward direction. This

can be explained by the fact that the momentum of the photon matters at high energy, while it is ignored in the dipole approximation. A full characterization of the distribution requires the parameters  $\beta$ ,  $\gamma$ , and  $\delta$  here which, again, have to be taken from literature even though not as much data is available for this case as for the dipole approximation. Related studies are going on in the scope of the aforementioned German-Russian collaboration [49] and some experiments in this field will be performed during the calibration and commissioning phase of the spectrometer (see Section 3.11). However, since the determination of the linear polarization basically requires an analysis of the symmetry of the azimuthal photoemission signal, it is still feasible in the discussed case, as the additional non-dipole parameters  $\gamma$  and  $\delta$  vanish in a plane perpendicular to the photon beam.

Moreover, the asymmetry determined by the  $\gamma$ -parameter might have an impact on the design of a spectrometer, since the direction of maximum emission is no longer located in the azimuth plane. Therefore, an increased efficiency of a device measuring outside this plane could be realized. The relevance of this effect will be evaluated by experiments in the end of 2011 and the first half of 2012 in order to confirm the choice of geometry for a spectrometer (see also Section 3.11), even though rather small effects are expected here.

Besides the generation of photoelectrons, further mechanisms exist in the considered system that lead to the release of electrons, e.g. as an indirect consequence of photon absorption. The most prominent process known here is the Auger recombination: after photoionization, an unoccupied state (the “core hole”) with a specific lifetime remains in the atom. The core hole will typically be filled by the transition of a bound electron with a lower binding energy to this vacancy. In the same step, the energy released hereby can be transferred to another electron of the same atom, which, in consequence, is emitted as a so-called Auger electron. As a result of the discrete binding energies of the involved atomic levels, the kinetic energy of Auger electrons is basically discrete and depends only on the corresponding binding energies. Therefore, a unique spectrum of Auger kinetic energy exists for every atomic species.

Auger electrons do not provide information on the preceding ionization, so they are not suitable for diagnostics of photon energy. We are interested in the electrons from photoionization only, so a superposition of the photoemission spectrum with Auger electrons has to be avoided by a proper photon energy-dependent choice of the observed atomic level. For the transition of an electron from state  $j$  to the core hole  $i$  with the subsequent emission of an electron from level  $k$ , the kinetic energy of an Auger electron is given as a function of the binding energies  $E_i, E_j, E_k$ :

$$E_{kin}^{Auger} = E_i - E_j - E_k. \quad (2.6)$$

Obviously,  $E_{kin} > 0$  has to be satisfied for the process to happen. In the common notation, a certain transition is labelled as a sequence  $ijk$  with  $i, j, k \in \{K, L, M, N, \dots\}$ , where the letters denote the atomic shell. Numerical subscripts of the letters are sometimes used to specify the subshell. The actual yield of electrons varies strongly among the possible transitions and was reported in the literature for only some cases. Well-known Auger processes are of the type  $i, i+1, i+1$  (i.e. KLL, LMM, ...) or  $i, i+1, i+2$  (i.e. KLM, LMN, ...), which have also been studied in the rare gases Ne, Ar, Kr, and Xe in various publications [69–98]. The relevance of Auger electron spectroscopy in the scope of this design will be discussed later (Sections 4.2 and 2.3).

In order to determine photon energy ranges in which photoemission lines potentially overlap with Auger electrons, we determined the kinetic energy of every possible transition for the rare gases Ne, Ar, Kr, and Xe. Here, we used the binding energies of the neutral atoms in their ground states tabulated in [47]. Therefore, we can give only a rough estimate of the actually observed energies because the tabulated levels will most likely not be the same for the ions in an excited state under consideration here.

Following Equation 2.1, the expected kinetic energies of the photoelectrons is derived from the binding energies (e.g. [47]). They have been plotted as a function of photon energy for every element and energy level in the panels of Figure 2.2 (in blue). A compilation of the possible Auger transitions following Equation 2.6 was added (in red), so potential superpositions can easily be identified. Note that the relaxation through a specific Auger transition requires specific core holes, and therefore a specific minimum photon energy to produce these. If an observed photoemission line is in superposition with the indicated Auger lines, potential difficulties evaluating the spectrum due to the non-constant background arise.

Even if the Auger energies derived here give only a rough estimation, we can identify wide photon energy intervals where no superpositions are expected and others that at least need to be checked before being used in diagnostics. In any case, extended “safe” intervals without expected superpositions can be found in Figure 2.2 and have been indicated with double arrows. To what extent these intervals affect the choice of gas for the SASE beamlines will be discussed in Section 2.3.

In this section, we outlined the physical processes that will be exploited for X-ray beam diagnostics of spectral distribution and polarization properties, as is currently demanded by the project. Recent research has proven the experimental relevance of various non-linear processes in photoionization of atoms (e.g. [99–108]) involving





## 2.2

## Time-of-flight spectroscopy of photoelectrons

After giving an overview of the physics of the photoionization of rare gases, we will focus now on the fundamentals of the ToF spectrometer that will be employed to probe the kinetic energy spectrum of photoelectrons. Our goal to indirectly measure the spectrum of the photon beam can, in general, be achieved by observing the emission from any atomic orbital, but the actual choice has to be made under consideration of the individual experimental and technical difficulties faced here. In this section, we will outline these issues and describe our strategy to obtain optimal results.

The physical principle of measuring flight time over a well-known distance in order to determine a particle's velocity, and thus its kinetic energy, is trivial. A technical implementation of this is limited by the accuracy of time measurement, which can be seen by the following example. The classical flight time of an electron with energy  $E_{kin}$  over a distance  $s$  is given by

$$t = s \cdot \sqrt{\frac{m_e}{2eE_{kin}}} \quad (2.7)$$

Assuming  $s = 20$  cm, and  $E_{kin} = 1\,000$  eV, the equation results a flight time of  $\approx 11$  ns. Measurement of a time in this order of magnitude is not a general problem, but since we want to probe a distribution, relative changes of flight time with kinetic energy have to be considered. For technical reasons discussed later (see Section 3.2), the time resolution of our detector system will be on the order of  $\Delta t = 0.5$  ns (more details in Section 3.9). In this example, the energy resolution of an electron with  $E_{kin} = 1\,000$  eV amounts to

$$\frac{\Delta E}{E} = 1 - \left( \frac{t}{t + \Delta t} \right)^2 \approx 8.8 \cdot 10^{-2}, \quad (2.8)$$

which is much worse than the expected spectral width of the photon beam of  $10^{-3}$  [29]. This example becomes even worse when the full photon energy range of the XFEL is considered, which also yields even faster electrons. Note that Equation 2.7 is valid only in classical physics. A relativistic correction will most likely become necessary for the highest kinetic energies produced at the SASE 1 and SASE 2 beamlines because a 10 keV photoelectron already has a (classical) velocity of  $0.2 \cdot c$ . The required resolution can be achieved only when the kinetic energy is much smaller than the photon energy. Therefore, it is convenient to observe the photoemission from an atomic level with the highest binding energy that produces photoelectrons at a certain photon energy. This approach can at least provide a

reasonable resolution near the photoionization threshold of every atomic level. Since the levels are sparsely spread over the complete energy range to be produced at XFEL.EU, this would result in an intolerable confinement to small energy intervals.

Instead, the energy spread of fast photoelectrons can be mapped to a larger spread in flight time by a defined deceleration along the flight distance  $s$ , the retardation. This is achieved by applying a negative electrostatic potential between the location of photoemission and the detector. The general necessity for retardation makes up the strongest requirement to the design of the spectrometer. Details will be discussed in Section 3.1. Using retardation, the flight time of photoelectrons starting with a certain kinetic energy can in principle be extended to infinity. A reasonable limitation is given only by the pulse structure, which limits the highest flight time to the temporal spacing of 222 ns between two photon pulses in order to avoid unambiguities. When a retardation potential  $\Phi$  is applied along the trajectory of an electron, the flight time can be computed by the following equation:

$$T = \sqrt{\frac{m_e}{2e}} \cdot \int_0^L \frac{1}{\sqrt{E_{kin} - \Phi(\ell)}} d\ell, \quad (2.9)$$

where  $\ell$  is the spatial coordinate along the trajectory. This relation is especially useful for a straight trajectory on the symmetry axis of the flight tube, where the electrical field is always parallel to the electron's velocity vector. In that case,  $L$  is the perpendicular distance from the beam to the detector.

The actual choice of a retarding potential depends on the geometry of the spectrometer, and further requirements, e.g. to observe a certain kinetic energy range. Influences from electron-optical effects limit the achievable energy resolution and definitely need to be taken into account. In the actual spectrometer design, the retarding potential along the symmetry axis can be tuned with some degrees of freedom, so flight time as a function of kinetic energy can be tailored within certain boundaries. The first derivative of the flight time of a charged particle (here: electron) in a ToF spectrometer as a function of kinetic energy is called the “dispersion relation” and is a characteristic of its capability to distinguish small differences in kinetic energy. The design of retarding potentials raises a set of essential technical questions that will be treated by simulations in the scope of our feasibility studies presented in Section 4.1. A roadmap for experimental validation of our results is given in Section 3.11.

Figures A.1 and A.2 indicate huge variations of the photoionization cross sections with photon energy, which, accordingly, results in strong variations of the magnitude of the signal at the detector. These variations become even worse if photon

energy-dependent variations of photon flux from the beamlines are considered (see Figure A.4). Additionally, the photon flux can be tuned upon user request by modifications of, for instance, electron bunch charge. Since the partial pressure can easily be tuned and stabilized within some orders of magnitude, it is useful to align the signal with the detector's dynamic range. In general, the spectrometer has to be driven with the highest available photoemission signal at lowest possible gas pressure. Therefore, the “strongest” photoemission line for observations at every photon energy has to be chosen, i.e. to observe the emission from a core level with the highest partial photoionization cross section among the rare gases.

To achieve a good energy resolution of the analyser is essential for diagnostics, but one has to bear in mind that optimization in this field has a natural boundary given by the natural line width of the photoelectrons, which depends on the observed core level and grows with binding energy by trend. Values of the natural line width as observed in photoemission have been reported in the literature [110–121]. The following table shows a compilation of related data of selected levels in rare gases.

Element	Orbital	FWHM width eV	$E_B$ eV	Resolution limit $\cdot 10^{-4}$	Ref.
Ne	1s	0.24	870	2.76	[110, 121]
	2p	< 0.001	21.6	< 0.46	
Ar	1s	0.68	3206	2.12	[121] [110, 116–118]
	2p	0.11	249	4.42	
Kr	1s	2.75	14350	1.92	[121] [121]
	2p	1.31	1679	7.80	
	3d	94			
Xe	1s	11.4	34561	3.30	[121] [121] [121] [121] [119]
	2p <sub>1/2</sub>	3.4	5107	6.66	
	2p <sub>3/2</sub>	3.1	4786	6.48	
	3d		676		
	4p <sub>5/2</sub>	0.12	145.5	8.25	

**Table 2.1:** Natural linewidth of photoemission lines for the rare gases

Since the photon spectrum and the kinetic energy spectrum are connected via a convolution with the combined profile of the natural line width and the energy resolution of the analyser, the photon spectrum can be determined most reliably when both factors have a small width. Assuming a perfect analyser, the worst-case limits of the achievable resolution can be estimated by the ratio of the binding energy of a specific subshell and the natural width of the associated photoemission line.

Note that FWHM peak widths are given here and that the values denote the resolution limit when exclusively considering this criterion. The stated numbers decrease with higher photon energy with  $(h\nu)^{-1}$ . Much of the reference data, especially of the natural linewidth due to lifetime broadening of the photoemission peaks, will have to be checked in the actual setup. Methods to deconvolve lifetime broadening from a spectrum have been reported in the literature [120] and might be considered as a part of online data evaluation in the future.

The choice of a gas also has some specific consequences for absolute measurements of photon energy, which need to be taken into account here. As implemented in Equation 2.5, the momentum of the photon may significantly modify the emission characteristic of the photoelectron. Additionally, very fast electrons will be emitted at high photon energy, so the recoil on the photo-ion as required by momentum conservation may become significant. Therefore, the kinetic energy of the photoelectron will be slightly smaller than expected from Equation 2.1. This effect is exploited by the COLTRIMS technique [62], for instance. In our case, it can probably be neglected, since the ratio of kinetic energies of the electron and the ion equals the ratio of their respective masses. Still, for high kinetic energies ( $\geq 10$  keV) and light gases such as Ne, the deviation in kinetic energy of the electron, as derived from Equation 2.1, can be of the order of the specified energy resolution ( $10^{-4}$ ). Among other effects, this motivates the choice of heavy rare gases for higher photon energy, like at SASE 1 and SASE 2.

A well-known issue in photoemission experiments with high-intensity beams is the broadening of spectral features by space charge effects [51–54]. Interactions between the emitted photoelectrons can probably be ignored when using a gas target, since the total yield is rather small. A more significant effect is the accumulation of photo-ions during a pulse train. Since these mainly have thermal velocity (plus a contribution from recoil) on the order of some 100 m/s, the average travel distance between two pulses amounts to only 20–200  $\mu\text{m}$ . First studies of the magnitude of the electric potential created hereby during a pulse train will be presented in Section 4.2.

The emission of a photoelectron can be followed by the emission of an Auger electron with a higher kinetic energy (Figure 2.2) with a typical delay of some  $f.s.$  In this situation, post-collision interactions [55] between the photoelectron and the Auger electron have been observed, which may lead to a broadening of the photoelectron's kinetic energy distribution. Significant broadening was mainly reported for relatively low photon energy, but is expected to occur at higher energy as well because the important parameter here is the difference of kinetic energies of both participating electrons.

Many of the mentioned points are still subject to research, so we cannot provide explicit values for the general case. A detailed characterization for our application is planned during the upcoming commissioning beamtime.

---

## 2.3 Impact on technical design

The major physical processes and the resulting requirements for photon diagnostics from rare gases were discussed in the preceding chapters. In summary, the following criteria for the choice of an atomic orbital for measurements have been figured out:

- Binding energy only slightly smaller than photon energy
- High photoionization cross section
- Strong directional dependence of the emission with respect to the direction of linear polarization (i.e.  $\beta$  considerably different from zero)
- No interference of the emission line with Auger electrons on the kinetic energy axis

From the well-known atomic reference data compiled in Appendix A, the observation of the photoemission signal from specific atomic orbitals for each photon energy is strongly encouraged. Based on the aforementioned criteria, we suggest a choice according to Table 2.2.

2.2 lists all relevant atomic energy levels of the rare gases [47] sorted by binding energy, which can absorb photons in the energy range of SASE 1/2 (upper section) and SASE 3 (below). The associated photoionization cross section is provided in columns 5 and 6, where the mentioned interval refers to the photon energy interval stated in the first two columns. The higher value of the cross section always holds for the smaller photon energy. For a binding energy up to 1 500 eV, tabulated values of the subshell photoionization cross sections originate from [46]. At higher energy, the values were estimated from the tabulated total cross sections in [50]. The kinetic energy range obtained here is found in columns 7 and 8. The photon energy intervals were chosen such that they begin well above the respective ionization threshold, so the kinetic energy amounts to at least some 10 eV. The spectrum of slower electrons could be superposed by an inelastic background, or they could even be captured by an ion-induced space charge potential. Furthermore, the actual magnitudes of the cross section near the absorption edges are not well known. The actual interval

	Photon energy range keV		Atomic level	Binding energy eV	Photoionization cross section Mb = 10 <sup>-22</sup> m <sup>2</sup>		Kinetic energy eV	
	Min	Max			From	To	Min	Max
SASE 1 / 2 3-24.8 keV								
	3	3.3	Kr 2p	1679	0.6		1321	1621
			Kr 2s	1921	0.06			
	3.3	5.0	Ar 1s	3209	0.075		81	1481
	5.0	14.5	Xe 2p	4786 5107	0.1		114	9708
			Xe 2s	5453	0.024			
	14.5	24.8	Kr 1s	14350	0.014		150	14200
SASE 3 0.25 - 3 keV								
	0.25	0.9	Kr 3d	94 95	4	0.2	155	805
			Xe 4s	213	0.2			
			Kr 3p	214 222	0.8			
	0.28	0.9	Ar 2p	251 248	3	0.1	30	650
			Kr 3s	293	0.2			
			Ar 2s	326	0.3			
	0.7	1.75	Xe 3d	676 689	3	<0.5	34	1084
	0.9	1.75	Ne 1s	870	0.3	<0.07	30	880
			Xe 3p	941 1002	0.3			
			Xe 3s	1149	0.06			
	1.75	3.25	Kr 2p	1678 1730	0.6		72	1572
			Kr 2s	1921	0.06			
	3.25		Ar 1s	3206	0.075		44	

**Table 2.2:** Summary of the core levels of the rare gases Ne, Ar, Kr, and Xe for the photon energy ranges of SASE 1/2 and SASE 3. A combination of the highlighted atomic orbitals is suggested for photon diagnostics in order to satisfy the requirements discussed in the text.

boundaries will be subject to change as soon as more precise reference data are available. The levels we propose for diagnostics are highlighted, where the light colour indicates options. Knowing the sequence of levels, we can assign photon energy ranges to be probed with that level, so the complete interval for every beamline is covered.

Since only a few atomic levels can be found for the SASE 1/2 range, we excluded only those with a very small photoionization cross section, or with only a small binding energy difference to a stronger line. The low density of levels results in very large upper limits of kinetic energy, which has a strong influence on the design of the spectrometer (see Chapter 3). In comparison to the SASE 3 beamline, relatively small cross sections are found here, so the feasibility at the expected signal levels must be controlled with special care, including considerations of the lowest acceptable signal level (Sections 3.9.3 and 4.3) and measures to enhance the measured signal (e.g. sections Sections 3.1 and 3.4).

The table indicates that Kr and Xe are essential for the concept in this energy range. As the best energy resolution of the spectrometer is expected for slow electrons, the use of Argon for the indicated energy range is highly desirable in order to improve the accuracy of the total system, especially in the low energy-region of SASE 1/2.

For SASE 3, again basically the strongest lines have been selected, even though the weaker ones still provide sufficiently strong emission, especially because the flux from the beamline here is much stronger than in the high-energy regime (see Figure A.4). We reduced the set of lines to a reasonable size in order to avoid an excessive amount of calibration data for the device required for every setting. In case spectroscopy from slow electrons (on average) is required, additional lines can easily be integrated into this scheme. The kinetic energies obtained here can be handled with reasonable effort. We suggest to use Ne, Ar, and Kr here, while Xe should be avoided in order to reduce the complexity of the gas supply system (Section 3.4) and to avoid potential difficulties with pumping.

Figure A.3 shows a compilation of reference data for the anisotropy parameter  $\beta$  from [45]. For every core level that was suggested to use here, we find values which are much different from zero. Therefore, the anisotropy of the photoemission can be expected to be sufficiently strong to determine the polarization vector from angle-resolved spectra for any photon energy produced at the European XFEL. However, the important fact is that this can be granted for SASE 3, where an actual demand for polarization control is expected.

Collision of the photoemission lines with Auger electron lines are quite likely throughout the selected intervals, but it has to be stressed here that the marked regions in Figure 2.2 represent a worst-case scenario. Finally, we expect only small “blind spots” along the complete energy scale. The potential of post-collision interactions is expected to become relevant mainly at relatively small kinetic energies  $\leq 50$  eV. At least the (roughly outlined) preliminaries are almost always satisfied here, so dedicated experiments are motivated here. A noteworthy exception is the Xe 3d level, which is expected to emit faster electrons than all Augers emission channels in the associated photon energy range. From the figures, extended regions without interference with unwanted lines could be determined in case this issue gets higher priority in the future.

The data provided here will act as a reference for estimations of the device performance given in Section 3.1, where the actual number of detected photoelectrons per pulse will be derived.





---

## 3 System design

---

### 3.1 Flight tube

The major part of a ToF spectrometer is its flight tube, in which the photoelectrons travel a well-defined distance. The kinetic energy of an electron travelling this distance is determined by measuring its flight time. The design we propose for use at the SASE beamlines was developed by the P04 group at PETRA III, DESY [6–8]. A cross section of the flight tube design can be seen in Figure 3.1. In its usual mounting position perpendicular to the beam, its front aperture with a diameter of 3.2 mm is located at a distance of 14.75 mm from the beam centre. For low space consumption, the inner part has a conical shape, while it is cylindrical at the end. The flight tube is longitudinally split into four segments, which are mechanically aligned to each other by electrically insulating centring rings. It is terminated by the detector unit. The segments are made of aluminium, which is coated with gold in order to guarantee good electrical conductivity of the surface and to avoid surface corrosion. The complete assembly is mechanically stabilized and electrically screened by a housing made of gold-coated aluminium sheet metal. Every flight tube segment has an individual electrical connection, so electrical potentials can be applied.

The flight tube assembly is mounted inside the vacuum chamber on a frame and is connected to the electrical vacuum feedthrough via the detector assembly. The electrical contact between both is established by pin connectors. These can be disconnected and reconnected without unmounting the flight tube, so the detector unit can be removed from the flight tube easily.

The retardation potential inside the flight tube is defined by the voltages applied to every element. As described earlier (Section 2.2) the main purpose of retardation is to improve the energy resolution at the cost of a constrained kinetic energy interval that can be observed in one photon pulse. Therefore, the achievable energy resolution strongly depends on the geometry of the flight tube and on the configuration of voltages. The initial phase space distribution of photoelectrons finally hitting the detector plays an important role, especially in a non-zero retardation potential. The phase space element includes the distribution of the starting position and a certain solid angle. For the moment, we can assume the beam path as a source of photoelectrons with a longitudinally homogeneous intensity and a transverse emission profile in accordance with the intensity profile of the photon beam. In the simplified case without retardation, the “accepted” solid angle of the flight tube is constrained by

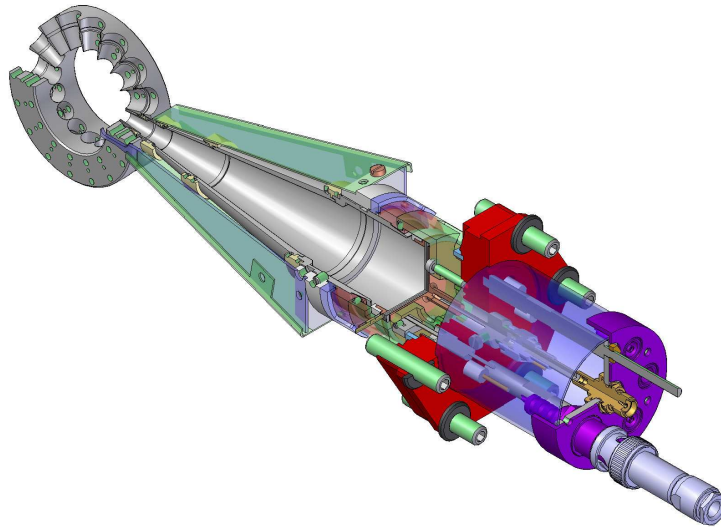


**Figure 3.1:** Cross section view of the flight tube and detector unit of the ToF spectrometer (courtesy of F. Scholz, DESY).

the entrance aperture. Still, the angular emission characteristic must be accounted for (see Section 2.1). Since the flight tube has to be treated as an electron-optical system, we can state qualitatively that a large phase space after emission leads to strong variations of the trajectories and large inhomogeneities upon detection (the phase space volume is preserved), in particular of the flight time and thus to a reduced energy resolution.

Moreover, the volume of the accepted phase space of a certain configuration determines the transmission, which is another crucial parameter of the spectrometer because it defines the number of photoelectrons that is detected per photon pulse. A suitable trade-off between the resolution and the transmission of the spectrometer is essential for effective application for diagnostics.

For the presented design, the transmission can be estimated under certain circumstances. Based on the physical reference data given in Appendix A, we provide an approximation of the expected signal strength for single-pulse diagnostics here. The realistic settings as outlined in the previous and the present chapter are assumed here, and we neglect the presence of a retardation potential in this first approach. The transmission is then exclusively determined by the geometry of the flight tube. Furthermore, we neglect the transverse dimension of the photon beam and assume

that the beam is perfectly aligned with the symmetry axis of the flight tube assembly in Figure 3.3. More realistic information on the transmission, especially taking into account the finite width of the photon beam, can be derived from electron-optical simulations presented in Section 4.1.

The longitudinal acceptance length along the beam direction can be estimated by the diameter of the aperture of the flight tube ( $D = 3.2$  mm). Higher distances would lead to a large angle versus the flight tube axis, so the detector could not be hit by an electron on a straight trajectory. The fraction of photoelectrons emitted into the solid angle of the entrance aperture  $\Omega_A$  is determined by integration of Figure 2.1:

$$\Delta\sigma = \int_{\Omega_A} \frac{d\sigma}{d\Omega} d\Omega \cdot \left( \int_{4\pi} \frac{d\sigma}{d\Omega} d\Omega \right)^{-1} \quad (3.1)$$

$$= 2\pi \cdot \int_0^{\alpha/2} (1 + \beta P_2(\cos(\theta)) \cdot \sin(\theta) d\theta \quad (3.2)$$

Here,  $\alpha$  is the opening angle of the aperture, which amounts to  $\approx 6.2^\circ$  for the current setup. The expression in Figure 3.2 is approximately valid for the complete acceptance length. It holds for the case that the linear polarization vector and the flight tube axis are parallel. For  $\beta = 2$ , the equation results a fraction of  $2.2 \cdot 10^{-3}$  of the emitted electrons hitting the detector. This number reduces to  $\approx 0.7 \cdot 10^{-3}$  in case of isotropic emission ( $\beta = 0$ ). Now, the absolute number of detected electrons can be calculated by

$$N = I_0 \cdot D \cdot \Delta\sigma \quad (3.3)$$

with  $I_0$  as defined in Equation 2.2. This has been applied to the configurations as seen in Table 2.2 for the SASE 1/2 and SASE 3 beamlines, assuming the number of photons per pulse as stated by Schneymiller and Yurkov [29]. Their values were linearly interpolated to provide data for the required photon energies. Hereby, we can derive an estimation of the highest signal levels we expect as a function of photon energy, as is shown in Figure 3.2. Note that, for several lines, the subshell ionization cross sections are not known and could only be estimated from total cross sections. Since this is only possible in the vicinity of the absorption edge, we state values for distinct pairs of photon energy and core levels. By introducing the vertical bars in the figure, we account for the variation of signal strength with bunch charge and electron energy. The partial pressure assumed in the calculations was  $10^{-5}$  mbar.

As we will discuss later (Section 3.9), a detected signal on the order of 100 – 1 000 electrons per pulse is sufficient for our applications. Therefore, almost the complete energy range of SASE 3 can easily be probed, even at low bunch charge. The

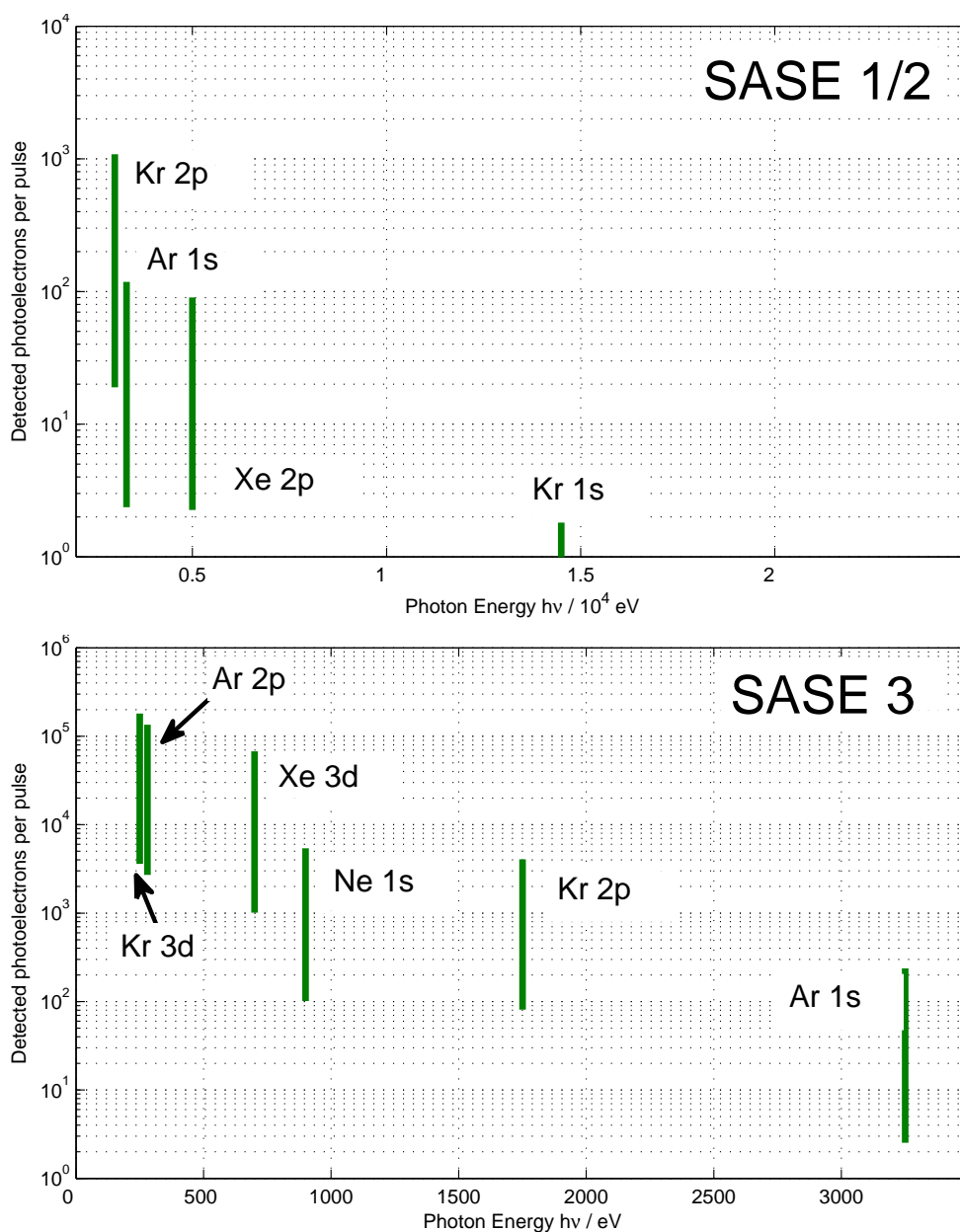


**Figure 3.2:** Number of photoelectrons hitting the detector per pulse for SASE 1/2 and SASE 3 beamlines using the simulated photon flux from [29] and the tabulated photoionization cross section from [46, 50]. A rare gas partial pressure of  $10^{-5}$  mbar is assumed.

extremely high maximum count rate at low energy calls for a reduction of the gas pressure during operation.

The situation at SASE 1/2 is slightly more difficult, mainly because of its higher photon energy. Ionization cross sections are known to decay with higher energy (Figures A.1 and A.2) and the photon flux at XFEL.EU does as well (Figure A.4). According to Section 3.4, the pressure in the interaction region can also be chosen much higher. Here, also a modification of the spectrometer geometry towards a higher acceptance angle has to be considered, but has to be well balanced with the requirements of energy resolution. Further simulation studies will be conducted in this field.

Note that the considerations made here can provide only a rough impression of the realistic situation. More detailed approaches taking into account, e.g. retardation potentials, will be presented in Section 4.1.

Some more aspects of flight tube design can be summarized as follows: The length basically determines the actual flight time, and therefore the sensitivity to small differences in kinetic energy, but spatial constraints apply here to the outer dimensions of the complete setup (Figure 3.7). An obvious reason for non-uniform flight time is the longer geometrical path length between source and detector for an electron entering the flight tube under an angle.

Furthermore, the local electric potential varies with the distance from the symmetry axis (see Section 4.1), so the actual instantaneous retardation acting on an electron depends on its actual trajectory. Especially at the transition between two electrodes, off-axis electrons are significantly deflected, which has an effect on flight time, for instance by an increase of the total length of the trajectory.

In a reasonable configuration, the total retardation is chosen such that the lowest kinetic energy of an electron to be observed amounts to approximately 1 eV at the end of the flight tube, as will be shown later in this section and in Section 4.1. Note that the stated minimum kinetic energy refers to the boundary of the observed kinetic energy interval. In an appropriate retardation setting, the centre kinetic energy of photoelectrons from a specific atomic subshell will therefore be mapped to 5–10 eV at the end of the flight tube, which appears to be sufficiently small to be tolerant towards small perturbations of the retarding potential.

In a given setting, this value has to be kept constant within narrow limits because small variations here will cause relatively large changes of the total flight time. As the energy after photoemission can easily amount to some keV, this requires very stable voltage supplies with an output voltage up to several kV, so the required relative

voltage stability amount to at least  $10^{-5}$ . High voltage modules for the MPod crate (ISeg/Wiener) have proven to provide a good solution of this issue and are therefore suggested here. For further reduction of high-frequency components of ripple and noise of the supply voltages, a low pass filter is connected between the voltage supply and every flight tube element, which is located directly at the electrical feedthrough.

Due to the fact that a detected electron can be uniquely assigned to a specific light pulse only when its flight time does not exceed the pulse spacing of 222 ns, the range of kinetic energies that can be detected with a single configuration of the spectrometer is limited. The absolute range is significantly altered when retardation is applied. For this reason, the width of the expected energy distribution has always to be taken into account when designing a retarding potential. The expected performance of the actual design has been studied extensively by numerical simulations of the electrical potentials and the dynamics of electrons therein. The general feasibility of achieving the required energy resolution has been demonstrated by these means. Selected results are discussed in Section 4.1.

This discussion of the major features of the flight tube is followed by an introduction to the details of the detector unit, which was especially designed to work together with the presented flight tube layout.

The cross section view in Figure 3.1 also includes the detector unit in its mounted position inside the vacuum chamber. In order to avoid stray fields from the detector surface to affect the field geometry inside the flight tube, a conductive mesh with four (optional eight) lines per mm and an open area ratio of  $\geq 80\%$  is mounted approximately 2 mm in front of the detector, which is usually kept at the same potential as the last flight tube segment.

The detector mainly consists of a triple stack (“Z-stack”) of microchannel plates (MCP). An MCP has a glass substrate with densely packed channels reaching from one face to the other with a typical diameter of  $10\ \mu\text{m}$  and centre-to-centre spacing of  $12\ \mu\text{m}$ . Open area ratios on the order of 60% are achieved here. A surface finish gives the faces and the inner walls of the channels a high, well-defined resistivity. MCPs basically act analogously to a secondary electron multiplier: When a high voltage of typically 1 kV is applied between the faces of the plate, an electron inside a channel is strongly accelerated and may emit secondary electrons after collisions with the channel wall. This process becomes more likely as the kinetic energy of the electron upon impact increases. Therefore, the retarded photoelectrons are reaccelerated by a positive voltage between mesh and MCP surface by several hundred volts.

An incident photoelectron initiates a charge-amplifying cascade, which results in a total amplification on the order of  $10^6 - 10^7$  of the complete Z-stack. The amplified charge pulse arriving at the back side of the MCP stack is collected by a thin copper electrode on a Kapton substrate, which is coupled capacitively to the signal output. This layout allows to decouple the signal from the DC potential at the rear side of the MCP stack. Both copper electrodes are connected to ground via  $M\Omega$  resistors. The MCPs from two different manufacturers, Hamamatsu and Photonis, were tested in this setup during experiments.

After amplification, single photoelectrons can be registered as macroscopic voltage pulses with typical amplitudes in the range of 10–20 mV. As a consequence of capacities and high resistances applied here, the signal readout has a considerable band-pass characteristic. Despite the presence of parasitic capacities, obtaining pulses with an FWHM  $\leq 1\ \text{ns}$  has been demonstrated using this design, which proved to be sufficiently short. Further difficulties of signal readout usually result from reflections of the fast electronic signal in cables. This usually leads to an “echo”, i.e. strong oscillations of the registered voltage while decaying. Here, this issue could be solved by appropriately matching cable lengths and resistances, so the observed oscillations were reduced to  $\leq 5\%$  of the peak voltage.



The essential requirement to the photoemission spectrometer is to provide reliable information on the spectrum of a single radiation pulse. In a statistical sense, this means providing a sufficiently large sample of the actual spectral distribution, i.e. to register a sufficient number of photoelectrons from every pulse. The detector output voltage as a function of (flight) time is then a superposition of the single-electron response, which needs to be sampled at a sufficient rate on the order of  $10^9$  samples per second ( $\approx 1$  GS/s). Detailed considerations on the requirements for data acquisition are given in Section 3.9.1. Our approach for online data evaluation as presented in Section 3.9.3.2 allows for extracting vital spectral information from as few as some hundred detected photoelectrons per shot, which is the lower limit of the expected signal for the complete range of photon energy and intensities of the XFEL. Simulations based on artificial ToF data for this scenario are discussed in Section 4.3.

The linearity of the detector system at high photoelectron flux is limited by the MCPs because a certain dead time of at least one channel or, more likely, a certain spatial environment of a channel, results after an amplification cascade. Therefore, the output signal saturates at high incident electron flux. To avoid non-linearities of the detector, spatial and temporal (i.e. within the dead time) coincidences have to be avoided in general. Obviously, a high count rate at a low number of coincidences can be achieved by spreading the electrons over the complete detector area by an appropriate choice of the electron-optical system of the flight tube.

That this can, in fact, be achieved is discussed by means of the electron-optical simulations presented in Section 4.1, even though a trade-off between detector linearity and optical aberrations becomes necessary. As mentioned before, best performance of the spectrometer is achieved when the flight time in the spectrometer is spread over the maximum possible interval of 222 ns. In principle, this contributes to avoiding coincidences as well. No information on dead time or sizes of “depleted” regions on an MCP could be obtained so far, so whether these measures significantly contribute to improve the linearity of the detector at high signal levels must be clarified by in-house experiments as proposed in Section 3.11.

In summary, the current design as developed by the P04 group (PETRA) has achieved a reasonable level of maturity concerning the mechanical and electronic design. It is a cost-efficient and space-saving solution, which especially matches the requirements of the ToF spectrometer and can compete with much more expensive, commercial solutions. The most important issues concerning performance at higher electron flux were addressed here, and will be solved during the upcoming phases of in-house development.

The design of the flight tube and detector unit have been introduced in the last sections. As has been discussed, a single instance of this design could already be used for diagnostics of X-ray pulses concerning their spectral composition. Here, we discuss how an arrangement of up to 16 flight tubes can extend the applicability of gas-based photoemission diagnostics to a much broader scope.

The outer dimensions of the flight tube housing are designed to have an opening angle of  $22.5^\circ$ , so up to 16 tubes can be arranged on a full circle, as shown in Figure 3.3. In this configuration, the alignment of flight tubes is granted by a central ring that has holes for the tips of every flight tube. In the current design, the open diameter of the ring is 29 mm, the smallest aperture of the system. The housings of the flight tubes are fixed to the ring. Hereby, all housings and the ring are in electrical contact, but still separated from ground. Alignment and fixation are independent of the flanges bearing the detector unit, so individual detectors can be replaced easily. The flight tubes are aligned such that the photon beam is directed in perpendicular to the plane of flight tubes and intersecting in the geometrical centre of the alignment ring.

The complete assembly fits into a custom-made cylindrical vacuum chamber with the outer dimensions of diameter  $\times$  length  $\leq 35 \times 30$  cm. The design of the 16 radial flanges is derived from CF40 specifications, but has a larger inner diameter to match the requirements from the outer dimensions of the detector unit. The flanges of the electrical feedthrough have been reduced to the smallest possible hexagonal shape in order to avoid collisions. CF caps at the front faces of the chamber assure good accessibility. The ports for the beamline and additional flanges for pumps, gauges, and the gas supply are located on the front caps, so vital parts of the complete chamber could easily be replaced by a newer design without the need for a new chamber.

An array of spectrometers equipped with 16 individual channels as described strongly enhances the potential for photon diagnostics. While a single channel mainly provides energy resolution, the angular resolution of the array can be used to probe the azimuthal emission characteristic over  $2\pi$ . In the dipole approximation introduced in Section 2.1, the intensity of photoemission is a function of the azimuth angle with respect to the direction of linear polarization of the photon beam. This relationship can be exploited assuming well-known  $\beta$ -parameters (e.g. Figure A.3) in Figure 2.1 in order to determine the direction of linear polarization from the measured, angular resolved intensities from every channel. Furthermore, the amplitude of the angular-dependent signal allows for a determination of the degree of linear

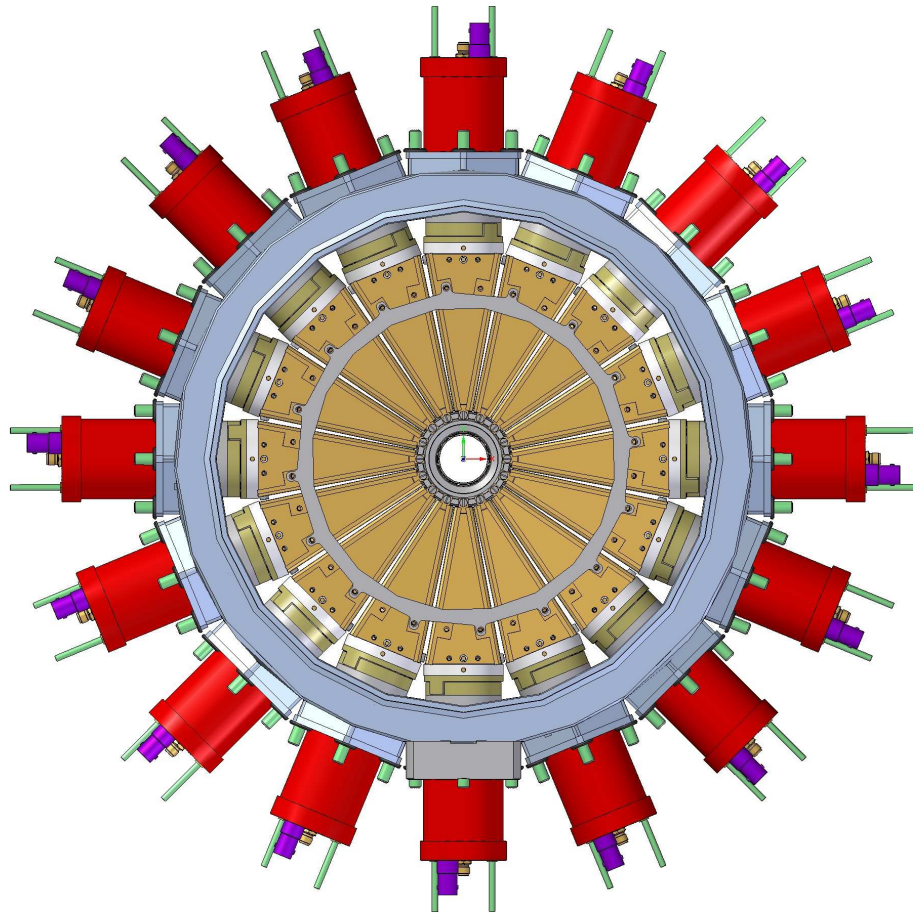


**Figure 3.3:** The complete spectrometer setup consists of up to 16 flight tubes as shown in Figure 3.1 (courtesy of F. Scholz, DESY).

polarization, because both circular polarized and unpolarized light contribute an isotropic signal. This option is of interest at beamlines where variable polarization may be established as a future option, i.e. at SASE 3 [10, 27]. This concept has been demonstrated to provide precise information with the proposed system.

Even though polarization measurement is the most obvious application of a multi-channel spectrometer, even beamlines with a fixed polarization (SASE 1/2) are expected to benefit from the availability of a number of independent channels. Former experiments by the P04 group have revealed a considerable sensitivity to the alignment of a flight tube with respect to the beam. Here, the measured difference of arrival time of two photoelectrons of a certain kinetic energy in two opposing detectors can be evaluated in order to determine the relative displacement of the beam along the axis of the two flight tubes from the geometric centre of the spectrometer array. Hence, the relative 2D position of the beam can be determined by using a horizontal and a vertical pair of flight tubes. However, the achieved sensitivity can be granted only for electrons with a low kinetic energy ( $\leq 100$  eV) because differences of flight time become smaller at higher velocities. For this case, an accuracy of  $\approx 10$   $\mu\text{m}$  has been demonstrated [6].

An alternative approach relies on the fact that the transmission of a single spectrometer decays quickly with the distance of the origin of photoelectrons from the symmetry axis of the flight tube (see Section 4.1). Provided the detector sensitivity is equalized well over all channels, this opens up another opportunity of measuring the beam position. However, this approach cannot compete the specifications of dedicated devices for beam position measurements such as the XBPM [42]. Here, it is only suggested to be used as an independent, auxiliary source of information which might be used for consistency checks or similar.

The position sensitivity of the spectrometer is basically an undesired side-effect because it complicates measurements in its major field of application, the distribution of photon energy. During regular operation, it must therefore be guaranteed that the actual beam position does not deviate significantly from the centre, say less than  $\pm 0.2$  mm. This requirement becomes important when taking into account that most likely neither the photon beam nor the spectrometer will have a constant position (see Section 3.7). By cross-checking the signal obtained in several channels under different azimuth angles, the spatial alignment can be validated.

Depending on the configuration of the retarding potential, the spectrometer allows for the simultaneous observation of a limited interval of kinetic energies at a given energy resolution. Especially when high energy resolution is required, the width of this interval typically amounts to some  $10^{-2}$  of the nominal kinetic energy, which is

sufficient to probe the spectral width of SASE radiation on the order of  $10^{-3}$ . Further applications are expected to require the simultaneous observation of much larger, continuous intervals, or around distinct energies at strongly different energy. This will be the case when spectral components besides the expected SASE emission are under consideration. For instance, the spontaneous background, different lasing modes, or higher harmonics would make up contributions at photon energies strongly apart from main SASE emission. Future extensions of the use case for the spectrometer might include further photoemission processes (for instance, non-linear effects) in order to extend the diagnostics capabilities to further characteristics of the photon beam, which would also require a certain flexibility of the experimental setup. All the mentioned points make the availability of several, independent spectrometer channels highly desirable.

Besides the mentioned benefits, a multi-channel design of the spectrometer could also improve its performance in the field of pure spectroscopy. Since the design size of the entrance aperture of the flight tube is limited by the achievable energy resolution, transmission and thus the available signal intensity, is limited. When XFEL.EU is operated at low bunch charge, or at highest photon energy, the signal quality will be limited by statistical noise. Here, two or more combined spectrometer channels with identical settings could provide sufficient signal levels.

A multi-channel design can also be justified from the technical point of view: Several components of the spectrometer are known to degrade with time, or even to fail. This mostly concerns vital parts of the detector unit, namely the MCPs, the signal pre-amplifier (Section 3.2), and potentially the voltage supplies. A high operating life of the diagnostics station is essential because of its foreseen position in the photon tunnels, which will be accessible for maintenance only during service days. Here, a reasonable redundancy must be introduced to the system layout.

A completely designed multi-channel layout of a ToF spectrometer has been introduced, which has already proven its capabilities in numerous applications. The rather long experience the developers in the P04 group at PETRA III have already gained makes us optimistic to employ it at the SASE 3 beamline without crucial modifications. In addition to polarization measurements, we discussed numerous reasons to set up a multi-channel layout at SASE 1/2 as well. Necessary modifications of this design for application at the high-energy beamlines for the European XFEL are summarized in Section 3.8. The radial configuration and the suggested number of independent channels is not mandatory in that case, but provides the most adept solution with the lowest space consumption. Future options might exploit physical effects that make the observation of photoelectrons from the same region mandatory.

---

## 3.4 Gas injection system

The ToF spectrometer will register photoelectrons emitted from rare gas after the absorption of X-ray photons. As outlined in Section 2.2, the best performance for diagnostics can be achieved when the observed atomic core level is chosen as a function of photon energy of the X-ray beam. According to Section 2.3, the complete energy range of every photon beamline can be probed best when Ar, Kr, and Xe are used for SASE 1/2 and Ne, Ar, and Kr for SASE 3. The partial pressure of the gas is of special importance here, since the flux of photoelectrons is proportional to the pressure. Therefore, it has to be kept as constant as possible. Furthermore, it must be chosen appropriately to grant sufficient signal strength at low intensity, on the one hand, and to avoid detector non-linearities and saturation effects at high intensity, on the other hand. Excessive pressure in the chamber would also potentially affect electrical insulation of the flight tube elements, or could even destroy the MCPs. From experience, an upper pressure limit for the MCPs of  $10^{-4}$  mbar can be stated. Note that a considerable stationary pressure gradient of 1–2 orders of magnitude can be established between the interaction centre and the MCPs by the layout of the injection geometry and the placing of vacuum pumps. When taking the transmission of the flight tubes into account, it can be shown that a sufficient signal level can be obtained over a wide range of SASE 3 with a pressure of  $10^{-6} - 10^{-5}$  mbar (Section 3.1). Especially for the high-energy region of SASE 1/2, an even higher partial pressure would be desirable, and also seems to be feasible without major modifications.

In this section, we describe the design of a dosing system for rare gas, which will be used to establish a well-controlled environment for the spectrometer. Its implementation will allow for the supply with different gases at a well-defined, stabilized partial pressure. Here, we give an outline of the mechanical layout, some questions of control and automation as well as a discussion of the requirements for gas containers. Safety issues of this subsystem are discussed in Section 5.2.

The most critical part of the gas dosing system is the inlet into the vacuum chamber. It is designed as a needle with a very small cross section, so the gas flow into the chamber is mainly limited by its aperture. During operation, the tip of the needle is located close to and pointing towards the centre of the spectrometer array (Figure 3.5). Simulations by J. Seltmann [13] indicated that the chosen geometry results in a well directed gas flow. In a stationary state, the partial pressure of the rare gas can therefore be kept highest in the region from which the spectrometers have highest acceptance. It is highly desirable to upkeep a stationary pressure gradient in the vacuum chamber because this allows for a higher pressure in the interaction region. Otherwise, it would be limited by the highest operating pressure of the MCPs.

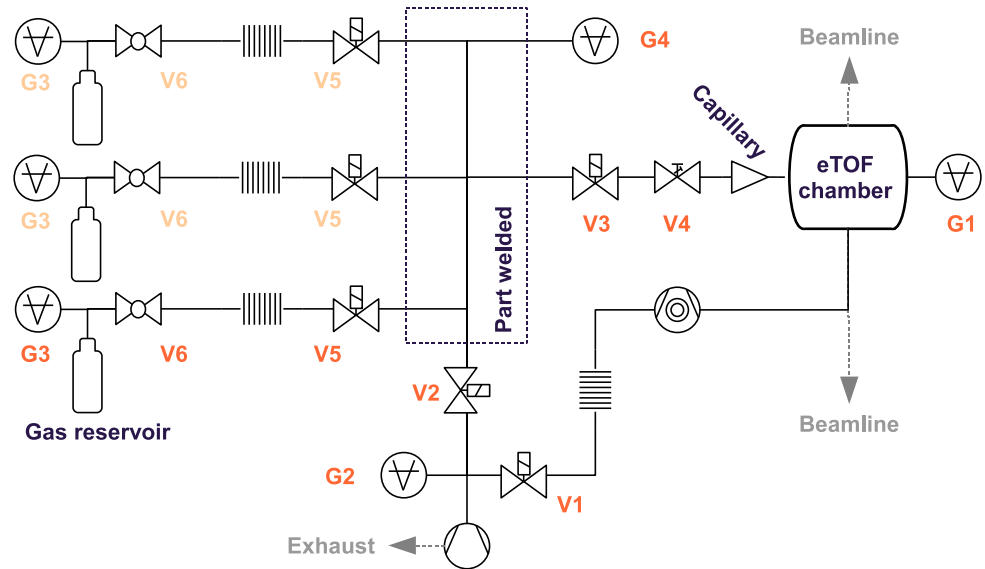


**Figure 3.4:** Layout of the gas injection system for gas-based diagnostics (symbols based on DIN 28401). Note that the forepump is shared among the vacuum chamber and the gas dosing system. The differential pumping stages upstream and downstream the chamber seen in Figure 3.6 have been omitted here. Explanation of symbols in Appendix B.

It can be concluded from further simulations [13] that this concept can be implemented in the best way when a circular symmetric arrangement of capillaries is used, which would enable the establishment of a “focus”, where the resulting pressure is limited only by the upper limit of the molecular flow regime. Another conclusion from [13] is that an asymmetric gas insertion leads to different pressure profiles along the flight tubes. Observations confirm that this affects the inelastic background measured in the spectrometers individually, so data evaluation is complicated. These considerations make us confident that the final design of the spectrometer will have an inlet which is symmetric with respect to the array of flight tubes.

The requirements outlined above lead to the design of a gas dosing system as depicted schematically in Figure 3.4. We assume three gas reservoirs at a high pressure, which is reduced to approximately atmospheric pressure. One gas at a time is guided towards the inlet via joint pipes. The needle valve located upstream of the gas inlet capillary is used for fine-tuning the gas flow. This type of valve usually has a limited number of operation cycles due to mechanical wear when being closed. Therefore, an optional gate valve is foreseen here for full closing of the connection.

The supply gas will be selected depending on the properties of the photon beam. This requires an option for switching between the gases during operation, especially upon a change of the photon energy. Since the gas flow through the capillary will



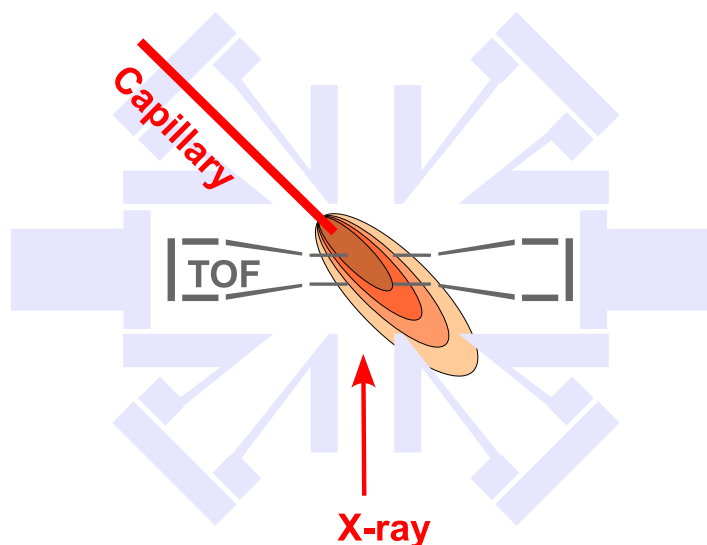


**Figure 3.5:** In the current layout, the gas is inserted continuously via a capillary under an angle of 45° against the photon beam. In effect, a stationary pressure gradient is established in the vacuum chamber.

be very small, it would take a long time until the intermediate volume that is shared among the gas reservoirs would be evacuated. In order to speed up the gas changing process, it can be directly pumped down using the regular vacuum pumps of the spectrometer chamber (see Section 3.5) by opening a bypass valve. This measure allows to evacuate the intermediate volume quickly down to  $10^{-2} - 10^{-3}$  mbar before the valves to the new gas reservoir are opened, so the purity of the supply gas should not be affected significantly after switching. The needle valve will have to be opened completely when the intermediate volume has reached a sufficiently low pressure of the forepump, so the dead volume between it and the capillary can be evacuated as well.

Every pipe segment throughout the system has its pressure monitor in order to avoid catastrophic failure during operation as a consequence of an unknown state. Here, a wide range of pressures needs to be covered, ranging from several bars at the reservoirs down to (ultra)high vacuum in the spectrometer chamber. Therefore, several types of pressure gauges need to be employed in the system, which need to be interfaced for surveillance and automation. We suggest using gauges from the Pfeiffer ActiveLine series here, which offers a big portfolio of gauge heads and provides a uniform interface via the MultiGauge controller. The actual gauges to be used here are found in Table 3.1



Position	Type	Pressure	Range
G1	Cold cathode full range	$10^{-3}$	$\leq 10^{-9}$
	Hot cathode full range	$10^{-3}$	$\leq 10^{-9}$
G2	Pirani	$10^{-3}$	1000
G3	High pressure	1000	5500
G4	Pirani	$10^{-3}$	1000

**Table 3.1:** Suggested gauge types in Figure 3.4

Here, “position” refers to Figure 3.4. Reasonable alternatives for the proposed gauge types at positions G2 and G4 would be capacitance gauges for more accurate readings in the mentioned range. For flexibility, the additional piping apart from the spectrometer chamber is planned to be based on “Kleinflansch” (KF) connections, which also allows for easiest interfacing of every attached component. The gas purity is potentially affected by the leak rate through the gaskets used here. The central part will thus be made up by a multi-port pipe with welded flanges in order to reduce the number of flexible connections and therefore to reduce the total leak rate of the system. The partial or exclusive use of VCR connections will have to be considered for best insulation from the environment. For general monitoring of gas purity, we suggest to place a residual gas analyser (RGA) permanently at a position equivalent to G1. The two gauge types mentioned in the table for that position are optional. Further details are given in Section 3.5.

The gas purity requirements also apply to the valves, which especially need to have a low leak rate towards the environment. Common right-angle valves available with KF flanges can usually be used here. A list of the valve types to be used in the system (referring to Figure 3.4) can be found in Table 3.2

Position	Type	Operation
V1	Right angle valve	electro-pneumatic
V2	Right angle valve	electro-pneumatic
V3	Right angle valve	electro-pneumatic
V4	Needle valve	servo-driven?
V5	Right angle valve	electro-pneumatic
V6	Stop cocks	manual

**Table 3.2:** Suggested valve types in Figure 3.4

Some manual valves are included in the design in order to grant safe isolation during maintenance or replacement of vital parts of the vacuum system. Every valve needed for regular operation must necessarily be remotely controlled and sensed. We prefer to use electro-pneumatic actuation, which is cost-efficient and can be implemented with relatively low switching power, so integration into the control system becomes easy.

Operation of the gas dosing subsystem must be widely automated. Here, we foresee mainly two processes that need to be handled by automatic controlling routines. During regular operation, the gas pressure in the spectrometer chamber needs to be stabilized by actuation of the dosing valve. A pressure set point and the choice of the gas have to be provided by a higher control instance or the user. Furthermore, exceptional cases, such as empty gas containers, must be recognized and handled. Since the system can cause critical failures in terms of machine safety, the control must be integrated well into the machine protection concept (see Section 5.2). The change of the operating gas will require opening and closing a series of valves while keeping the system in a safe state, i.e. pressure limits have to be obeyed before opening a valve etc.

We plan to implement the automation scheme of the gas dosing system in the device control framework defined by Work Package 76 (WP-76). Therefore, the communication protocol of the Pfeiffer MaxiGauge controller will be implemented in the TwinCAT software, which runs the EtherCAT field bus for remote control of arbitrary devices in the photon tunnels. A variety of valves exists on the market that can be operated by digital voltages of 12 V or 24 V, so integration into the control system can easily be done via digital output terminals of the EtherCAT bus by Beckhoff Automation GmbH. The related position read back will also be implemented on this hardware platform. The needle valve requires analogue control and readout. The integration of this component will be defined as soon as a specific product has been chosen.

Finally, the technical design of the term “gas reservoir” has to be specified. We have currently two possible solutions under consideration: The first option is to set up a local gas cabinet with high-pressure bottles close to the diagnostics station in the photon tunnel. At least at the currently planned position in the XTD2 section of the photon tunnel (see Section 3.7), sufficient space would be available for this option. If this holds for the other planned locations as well has yet to be clarified. The drawback of this solution is that a sufficiently large amount of gas would have to be kept in stock there, since the accessibility of the location for exchanging empty bottles will be limited to service days. The actual gas consumption and the resulting service intervals still have to be figured out, but an early estimation has been given

in [40]. Once a decision on the detailed layout of the complete vacuum system is made, dedicated software tools can be applied to simulate the gas flow through the system [15] and thus the consumption. Big amounts of gas in the tunnel are safety-relevant because immediate release of the gas could cause a critical oxygen depletion (see safety analysis in Section 5.1).

An alternative solution would be to place the gas containers in a well-accessible area, e.g. in the shaft buildings, and to guide the gas via welded stainless steel pipes to the spectrometer chamber. This would drastically reduce space consumption in the photon tunnel, but has some other effects on feasibility.

For instance, individual piping would be required for every gas here. Since the nearest shaft buildings are at a distance of up to 200 m from the foreseen positions of the spectrometers [24, 37], the pipes would have a considerable volume (e.g.  $\approx 5.6\ell$  for 200 m length and a diameter of 6 mm). Using only a single line would severely affect gas purity at the diagnostics chamber because it would be impossible to evacuate such a long pipe before switching the gas. In addition, every gas change would consume the gas volume in the pipe unused, which would lead to a considerable increase of operating costs. Prices for piping are expected to be considerable. Gas purity requirements force an initial analysis of leakages over such a long distance. A concept for the initial cleansing of such a supply system is yet to be created. Despite the challenges outlined here, the second solution might be the better one because it definitely avoids an interruption of service when gas runs out and will consume no space in the photon tunnels.

We conclude that the subsystem for gas supplies of the spectrometer has been developed far enough to start the implementation of a prototype soon. We recommend using it to use it as a showcase for the various tasks in the field of automation and operational safety that need to be absolved in a close collaboration between the work packages of the European XFEL. Some details are still open, but so far we have been able to develop options and to discuss their implications.

---

## 3.5 Vacuum system

The complete spectrometer setup will be contained in a vacuum chamber with dedicated equipment for vacuum generation and monitoring. In this section, we outline the basic requirements of the vacuum system and our concepts for implementation as shown in Figure 3.6. Compared to the regular sections of the photon beamlines, we face special conditions in terms of operating pressure, gas composition, and gas flow in our case.

According to the current design, all parts of the chamber interior are made of materials that are compatible with the requirements for the design of vacuum parts for the photon beamlines at the European XFEL defined by Martin Dommach [26]. The flight tubes mainly consist of gold-coated aluminium and polyether ether ketone (PEEK), a UHV-compatible plastic material. Selected parts of the framework are made of MACOR ceramics. Electrical connections are made by Kapton-coated copper wires. Even though the choice of materials would allow for higher temperatures, bake out at 80°C is usually sufficient. However, base pressures  $\leq 10^{-8}$  mbar have been demonstrated with the prototype by the P04 group at PETRA III, DESY [8]. All state-of-the-art design recommendations for good vacuum performance have been applied as far as possible. All drilled holes are bypassed to avoid virtual leaks. The design of the flight tubes demands a certain trade-off here, since holes in its walls with a reasonable pumping cross section would lead to strong distortions at the periphery of the retarding potential. Due to the design specifications of the spectrometer, these cannot be tolerated. Thus, in the current design, the entrance aperture of the flight tube is its only well-defined opening.

However, the base pressure in the chamber (i.e. when the rare gas inlet is completely closed) is supposed to be as small as possible in order to guarantee the highest purity of the gas during operation. This is especially important in case the photon beam has a significant low-energy component from e.g. spontaneous undulator radiation. The typical residual gas composition in a vacuum chamber is made up by the low-Z elements nitrogen and oxygen. Since these have much higher photoionization cross sections at low photon energy (some hundred eV range) than the rare gases at high photon energy (full SASE range), the total photoemission yield from the undesired residual gas might approach the one from the actual gas used for diagnostics, even when its partial pressure is relatively small. Large contributions to the photoelectron spectrum from anything but the rare gas is undesired for diagnostics and has to be reduced as much as possible.

During regular operation, the spectrometer chamber will be filled with rare gas (see Section 3.4), where the maximum operating pressure is limited by the MCP detectors and roughly amounts to  $\leq 10^{-5}$  mbar. Our design goal for the vacuum system is to grant well-controlled operation up to at least  $10^{-4}$  mbar. Upstream and downstream, the diagnostics station is connected to the photon beamline by windowless vacuum. The beamline specifications foresee a design pressure of  $\leq 10^{-9}$  mbar [28]. Moreover, the exclusive use of ion getter pumps is planned there. Therefore, a high stationary pressure gradient has to be maintained between the spectrometer and the beamline and, as a consequence of the limited pumping capacity of ion getter pumps, the gas flow into the beamline has to be as small as possible. The need for a high pressure gradient calls for a high pumping capacity located near the chamber.

The relatively high gas load in the mentioned pressure range is feasible by using turbomolecular pumps here. The actually needed specifications still have to be figured out. The prototype design introduced in Chapter 3 showed up to perform satisfactorily with two Leybold turbo pumps mounted to pipes at the face plates of the chamber. Due to the fact that relatively heavy elements are to be pumped here, we expect a good effective pumping speed with at least the ratings achieved for  $N_2$  or  $O_2$ . The choice of a specific pump model is limited by one important design feature: Some manufacturers (e.g. Pfeiffer) use magnetic bearings for their pumps, which are known to create considerable magnetostatic stray fields [9]. Because magnetic fields with the magnitude of the Earth's magnetic field can already introduce significant perturbations to the photoelectron trajectories in the flight tube (see also Section 3.6), they have to be avoided. This also includes products from Pfeiffer Vacuum GmbH, which would be preferred otherwise. We intend to use turbomolecular pumps from Adixen (a division of Pfeiffer) instead, which have only slightly worse specifications and make use of completely non-magnetic ceramic ball bearings.

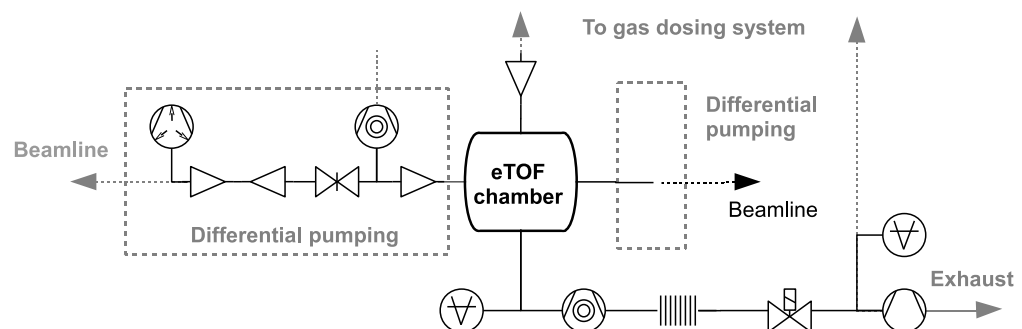


**Figure 3.6:** Layout of the vacuum system for the spectrometer. The setup is terminated upstream and downstream by differential pumping stages. The forepump is shared among the main chamber and the gas dosing system (see Figure 3.4). Symbols as in Appendix B.

Prevacuum will be established by dry scroll pumps, preferably by Edwards Ltd. The tip seals of scroll pumps need to be exchanged on an annual basis, which could make up the better part of the maintenance work of the vacuum system. Note that the pumps in Figure 3.6 are shared among the vacuum system of the main chamber and the gas dosing system.

In order to reduce the gas flow into the beamline, differential pumping stages will be employed at the terminals of the spectrometer chamber. Its layout basically consists of a series of small apertures with an intermediate volume, where independent vacuum pumps are attached. Here, we have to bridge a stationary pressure gradient of up to five or six orders of magnitude, which might require more than one differential pumping stage in a row, which potentially causes extra costs by requiring additional pumps. The fact that the design of the gas inlet already helps establishing a stationary pressure gradient slightly relaxes this requirement. A final assessment on the design the differential pumping stages can be given after gas-dynamic simulations of the actual vacuum chamber geometry.

Due to the relatively high expected gas flow, at least the first stage must be pumped by a turbomolecular pump. Good results have been achieved with a single stage at the prototype design [9]. A special design for the beamlines at XFEL.EU is currently under development by the “X-Ray Optics and Beam Transport Group” (WP-73) [15]. The ultimate lower limit of the aperture size is given by the design policy of WP-73 [28], which defines the smallest acceptable radius of any aperture as  $6 \cdot \sigma$  of the (assumed Gaussian) photon beam profile at a specific position along the beamline. The design to be developed here will also be used for the integration of the other gas-based diagnostics devices, such as XBPM [42] and XGMD [43].

Even a perfect differential pumping stage cannot block gas atoms on a straight path through all apertures, so a certain gas flow in molecular flow regime remains. More sophisticated approaches make use of Penning-type ion traps in order to establish a high density of atoms on the straight path and thereby deflect the remaining atoms by collisions. If our setup could benefit from such a design will be the subject of future studies.

In case of failure, a turbomolecular pump acts as a direct connection between the backing pressure and the beamline, so the two gate valves in Figure 3.6 have to be placed as a measure of vacuum protection. Remote operation and the integration into the machine-wide beam protection system is therefore mandatory. General safety implications of the vacuum system will be discussed in Section 5.2. The mentioned valves are also desirable for maintenance, when the spectrometer chamber needs to be vented or removed from the beamline.

In accordance to the gas dosing system (Section 3.4), our current design assumes pressure monitoring of the vacuum chamber to be implemented on the basis of components from the Pfeiffer ActiveLine series. Probing the total pressure in the main chamber is of central interest for automated gas dosing and safety as well. Our design pressure range  $10^{-4} - 10^{-9}$  mbar suggests the use of a combination of a Pirani gauge with either a hot or cold cathode gauge, which allows for operation between atmospheric pressure down to ultrahigh vacuum  $\leq 10^{-9}$  mbar. Both device types have specific advantages and disadvantages for our use case, which are discussed briefly now. Hot cathode gauges are basically designed for very low pressure, i.e. in the UHV regime.

A reduced lifetime of the hot filaments is expected in case of long-term operation at pressures around  $10^{-5}$  mbar and above, even in a rare gas atmosphere. This gauge type is known to emit electrons and ions, which might contribute to a background measured in the spectrometer, so sufficient distance to the flight tubes or electrostatic screening of emitted charged particles would have to be included into the design. In this case, potential fringe fields influence the well-defined field geometry of the spectrometer. Cold cathodes are assumed to experience no degradation of lifetime when operated at relatively high pressure. Unfortunately, their design includes permanent magnets, so a magnetostatic stray field is introduced to the system, which might, again, reduce the ultimate energy resolution of the ToF spectrometer. Emission of charged particles is also known for this gauge design, even though a smaller total emission can be expected.

Here, dedicated lab studies with a prototype have still to be carried out in order to determine the best choice for our setup. Because of the central role of pressure monitoring in the main chamber, we will consider a redundant setup at this position. More measuring points of the pressure are between the forepump and the main pump for pump diagnosis and beyond the differential pumping stages at the beamlines or even at the intermediate volume of the differential pumping stage.

Besides the gauges at the main chamber, we suggest to place a mass spectrometer (position G1 in Figure 3.4), preferably the MKS Microvision 2, which is currently developing to become a standard at the European XFEL. Hereby, gas purity could be determined frequently in order to validate the operating conditions of the spectrometer and to diagnose a potential contamination of the beamline from supply lines of the spectrometer early, mainly to avoid damage of any optical component by deposition of, for instance, carbon. The precise positioning is still subject to design. Any interference with the spectrometers and also the appropriate representation of the actual gas composition by the mass spectrometer in case of a remote position have to be considered here.

As an optional component of the vacuum system, we will consider to place a buffer volume of  $\geq 50 \ell$  between the forepump and the turbomolecular pump of the main chamber. By employing such a buffer, the scroll pump could be switched off after evacuation of this intermediate volume to a certain base pressure and switched on again when approaching the upper limit of the exhaust pressure of the turbo pump. Hereby, the net operating time and therefore the wear of the forepump could be reduced significantly, so service intervals could be extended. This solution has proven to be suitable in UHV applications where gas flow is small. Typical net pump times of the forepump achieved here are on the order of 5 min every 2 h. Whether our design could benefit from this depends on the actual gas flow through the system and has still to be checked thoroughly.

We presented an outline of the requirements and the design of the vacuum system for the photoemission spectrometer here. Some solutions have still to be worked out in detail, but, in conclusion, we are confident that the implementation of a final layout can be realized using commercially available products and well-proven concepts from the field of vacuum technology.



Optimal performance of the spectrometer can be achieved only when all significant forces acting on the electrons in the flight tube are taken into account. Besides the intentionally applied electrostatic forces from retardation as discussed in Sections 3.1 to 2.2, this mainly includes the effect of a magnetic field on the electron trajectories.

This naturally includes the Earth's magnetic field, but also inhomogeneous fields from numerous potential sources in the environment of the spectrometer, such as:

- **Turbo pumps**

Modern design of turbomolecular pumps makes use of bearings with permanent magnets. Furthermore, the incorporated electrical drive might create a fast AC field. In both cases, the potential proximity of the pump to the spectrometer makes this a critical topic. Therefore, we plan to use pumps with a conventional ball-bearing design.

- **Pressure gauges**

Cold cathode gauges have specific advantages (Section 3.5), but also rely on permanent magnets. Some manufacturers (e.g. Pfeiffer Vacuum GmbH) offer screenings in order to reduce the stray field.

- **Ion getter pumps**

Ion getter pumps will be employed to maintain the vacuum in the photon beamlines. They have strong magnetic stray fields, but are expected to have a sufficiently large distance from the spectrometer setup.

- **Steel**

Many alloys incorporating iron or nickel, which are generally considered non-magnetic, tend to show small remanent magnetic fields after mechanical processing. This is true for machined parts made of stainless steel, nuts, bolts etc. The supports of the beamline will be made of regular steel that can easily be magnetised.

- **Motors**

The windings of every electric motor under operation create AC stray fields. Note that, because of their holding current, stepper motors do not necessarily have to rotate to produce a magnetic field.

#### ■ Gold-coated aluminium parts of the flight tubes

Before an aluminium part, such as the flight tube elements, can be coated with gold, an intermediate Nickel layer has to be deposited. Lab measurements showed that a realistic overall thickness of a few ten nanometres is already sufficient to make the layer ferromagnetic [9].

In the presence of a magnetic field, the trajectory of an electron is bent by the Lorentz force, so it is reasonable to consider the bending radius obtained for a certain field acting on an electron at a given velocity. A suitable expression can be derived from the well-known equation for the cyclotron motion:

$$r = \frac{1}{B} \cdot \sqrt{\frac{m_e E}{e}}, \quad (3.4)$$

where  $E$  is the kinetic energy (in eV) and  $B$  is the magnitude of the field perpendicular to the velocity vector. In order to estimate the maximum tolerable magnetic field in the flight tubes, we claim that  $r$  must be much larger than the typical dimensions of the flight tube, for instance its length  $L$ :  $r \geq 10 \cdot L$ . For the Earth's magnetic field with 50 nT (magnitude in Northern Europe), this means that this criterion can be met only by electrons with more than 800 eV. Since in any configuration, retardation will always slow down the electrons far below this limit, the influence of the Earth's magnetic field has always to be considered.

Most of the sources of magnetic fields listed above can already be eliminated during design. Especially the interior of the actual spectrometer chamber will be made of strictly non-ferromagnetic materials. The issue of a potentially magnetized Nickel interlayer at the flight tube elements can probably be solved by reducing the layer thickness. Ongoing studies on alternative material combinations could allow to omit the Nickel layer. Despite a dedicated non-magnetic design, some active measures have to be implemented to reduce the remaining magnetic stray fields in the flight tube as much as possible. Two competing approaches have been made here.

First, an external magnetic field can be compensated by superposition with an intentionally applied field. Two identical, parallel-aligned coils with a Helmholtz geometry can be tuned such that the axial field in a considerable volume around their geometrical centre is reduced to approximately zero. Three perpendicular coil pairs can thus be used to compensate a homogeneous external field with arbitrary orientation, a method that has been applied with great success in the current prototypes of the spectrometer, especially because the coil currents can easily be tuned to match the local magnetic field vector, so a homogeneous field can always be compensated perfectly.

One fundamental disadvantage of this strategy is that the compensation in such a geometry works only for a limited volume around the centre, which could only be extended to match the dimensions of the spectrometer chamber if their diameter was chosen multiple times larger than the chamber diameter. As a consequence of the limited available space, the compensation at the end of each flight tube, i.e. where the electrons are slow, is expected to be less efficient. According to Equation 3.4, the strongest effect on the trajectories occurs there.

Alternatively to the compensation of a field, it could also be screened by enclosing critical parts into Mu-metal shields. Since this material is especially magnetically soft, it can be used to redirect the local field away from the flight tubes. This method is very well known in electron spectrometer design as it has been applied in numerous commercial products. Unfortunately, it works best as long as the shielding has no or only a few, small holes, so the high number of flanges needed for the current design would strongly reduce, or even reverse, the benefit of such a shielding. Enclosing the complete chamber with a closed Mu-metal housing is considered not suitable here, since this would require to avoid any sources of fields in the interior. In any case, a Mu-metal shielding must be designed with great care in order to avoid an unexpected field geometry.

Even though both approaches are in general known to lead to feasible solutions, a combination of both has proven to be counterproductive, because any compensation field will be redirected in parallel to the surface of any Mu-metal shielding. However, if applied individually, both potential solutions are reasonable and will therefore be considered in the future. The effect of residual fields will have to be checked in detail in the electron-optical simulations (as in Section 4.1) to support the future design process.

## 3.7 Integration into the facility

Integration of the spectrometer setup into the general layout of the photon beam systems at XFEL.EU raises several questions concerning the interfaces with numerous subsystems, which are outlined in this chapter. We mainly give a summary of the important issues here, since many details are discussed across the complete document. Here, we refer to the future mounting position in the photon tunnels as it is currently foreseen, according to the concurrent documents on beamline design [32–34], [24]. Various technical requirements can be derived directly from the planned location. Some necessities of the actual environment are included in the following considerations. Figure 6 in [37] gives an overview of all diagnostics components as they are currently planned at the SASE beamlines. According to this plan, the spectrometer will be located downstream the offset mirrors.

The following table contains the longitudinal position of the spectrometer in each beamline together with that of the offset mirrors and adjacent diagnostics as defined in [24]. The positions refer to the source point of SASE radiation [25] and denotes the centre of every device:

Beamline	Component	Section	Room	Position/m	Ref.
<b>SASE 1</b>	Second offset mirror	T9	XTD2	257.86	[28]
	Pop-In monitor	T9	XTD2	261.36	[38]
	PES	T9	XTD2, R14	265.24	–
	C-Monochromator	T9	XTD2	269.86	[28]
<b>SASE 2</b>	Second offset mirror	T6	XTD6	301.36	[28]
	Pop-In monitor	T6	XTD6	304.86	[38]
	PES	T6	XTD6, R1	308.74	–
	C-Monochromator	T6	XTD6	314.61	[28]
<b>SASE 3</b>	Second offset mirror	T10	XTD10	285.07	[28]
	Pop-In monitor	T10	XTD10	288.57	[38]
	PES	T10	XTD10, R2	292.45	–
	FEL beam absorber	T10	XTD10	298.32	[28]

**Table 3.3:** Currently planned positions of the PES and adjacent components as of spring 2012 (data from [24]).

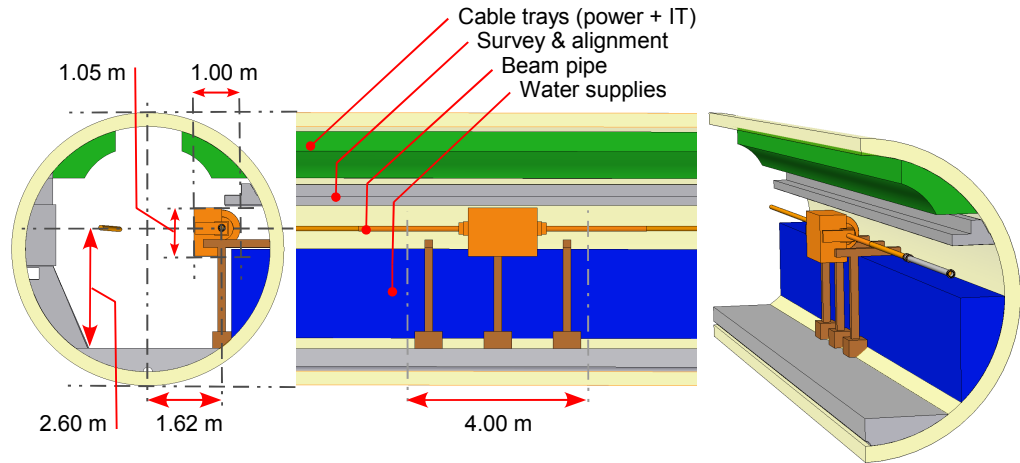


**Figure 3.7:** Cross sections of the XTD2 photon tunnel around the currently foreseen position of the spectrometer (shown in orange). All shown components are placeholder models at the current level of design. (geometry from SolidEdge CAD integration model by N. Kohlstrunk as of spring 2012).

Some specific or more general consequences of this choice are:

#### ■ Photon spectrum

We expect that the full SASE spectrum will arrive at this position, except for very hard X-rays ( $h\nu \gg 30$  keV), which are blocked by the offset mirror assembly. Features of the spectrum that might be inspected by the diagnostics stations therefore include the spontaneous background and the “regular” FEL radiation, as well as higher harmonics.

#### ■ Outer dimensions

Figure 3.7 shows a cross section of the photon tunnel at the position of the spectrometer. Anywhere in the photon tunnels, the most rigid constraints apply to the radial dimensions, which are confined to  $\approx 50$  cm here, according to the currently foreseen dimensions of the placeholders for the supplies of water and electricity. By the choice of a relatively short length of the flight tubes, the overall design of the spectrometer complies with this requirement. The longitudinal dimensions are made up by the spectrometer chamber itself and the length of the two neighbouring differential pumping stages. An overall longitudinal space of  $< 5$  m should suffice here.

#### ■ Rack space

In an updated version of the TGA documents [32–34], the equivalent of two full-sized racks for electronics has been reserved for:

Device	Number	HU
ISeg MPod voltage supply	1	9
Digitizer and FPGA module		6
Beckhoff EtherCAT terminals	1-2	4
Turbo pump power supplies	2-3	4
Pressure gauge controllers	1-2	4
Mass spectrometer controller	0-1	
Valve controllers	$\leq 10$	4
Reservation for external components	–	–
Cooling	–	–
Open Space	–	–

**Table 3.4:** Estimated rack space requirement for components of the ToF spectrometer.

Most of the heights given here are estimates, since an actual model has not been selected for most of the applications. Any hardware controllers might attach more than one device, so the actual space requirement cannot be estimated precisely. Including some open space for cooling (and the cooling devices themselves), and some reserved space for external contributions (e.g. the timing system), one full-sized rack with 42 height units (HU) can easily be filled. Whether this height can really be granted near the spectrometer strongly depends on the final location, so we currently foresee two racks for electronics.

#### ■ Further space requirements

Further space in the photon tunnel will be required by vacuum equipment, especially the pumps (Section 3.5) and, optionally, a buffer volume. Depending on the final layout of the gas dosing system, either some space for gas pipes to the nearest shaft building, or the space occupied by one or two gas cabinets, has to be reserved.

#### ■ Accessibility

The height of the photon beamline (Figure 3.7) makes the spectrometer assembly hard to access during installation and maintenance. A fixed or movable working platform would be required here. Furthermore, the device can be accessed from only one side in its mounted position, so we consider designing the support of the assembly such that the spectrometer chamber can be shifted away from the tunnel wall after disconnection from the beamline. In any case, the option

of removing and/or replacing the device for extended maintenance in the lab should be supported. Therefore, the gate valves upstream and downstream the spectrometer in the suggested positions as indicated in Figure 3.6 are also needed to isolate the device from the beamline, so the vacuum in the beamline will not be broken when the spectrometer chamber is removed. The gap which is left behind in such a case has to be closed with an appropriate pipe section, which is pumped by a mobile pumping station.

#### ■ Radiation background

An open issue for general instrumentation installed in the tunnel is the estimation of a radiation dose it receives in a certain position (Section 5.2), which is especially important in places where the photon beamline and the electron beamline are located in the same tunnel.

#### ■ Shifting Unit

At the planned location close to the offset mirrors, the beam position is expected to move up to  $\pm 30$  mm horizontally depending on the configuration of the mirrors. Since the spectrometer has to be aligned to the beam, the complete vacuum chamber has to be set up on rails, so it can be shifted accordingly. Such a device could easily be designed using standard machinery parts (e.g. Mdler company) such as off-the-shelf rails and spindle drives. Full automated actuation (servo or stepper motor) and position readout (industry standard encoders) can be realized on the basis of the Beckhoff EtherCAT field bus, which is also used for other applications in place. The relatively small aperture in the centre of the spectrometer array of 30 mm can potentially block the X-ray beam when moving, so the suggested design has a high safety relevance (Section 5.2). This requires that the shifting unit can provide input to the Machine Protection System and has sufficient reliability by placing redundant position sensors, for instance. The approach requires to move the differential pumping stages as well (Section 3.5), since these will most likely have the smallest apertures in the system ( $\geq 10$  mm at SASE 1/2 and  $\geq 15$  mm at SASE 3).

The great advantage of the actual position is that only one spectrometer array per SASE beamline is required to provide diagnostics data to every experimental end station. When reviewing the aforementioned consequences of that choice, one can conclude that several safety and cost issues are caused by this particular choice. Since the spectrometer does not rely on specific features of the photon beam, it could also be placed at alternative positions along the beamline. The highest impact on cost and safety of the associated subsystems could probably be achieved by placing the spectrometer at the last section of the beamline, i.e. in a close proximity

to the experimental end stations. There, the setup could benefit from the differential pumping stages that are already foreseen. The offset of the photon beam will be negligible there, so no moving stage would be required. Moreover, the gas supply systems and maybe even the electronics racks could be moved out of the tunnel, so their general accessibility could be improved. Finally, the fast shutters for vacuum protection could be used there to omit the safety valves (Section 3.5).

Moving the diagnostics station downstream of the distribution mirrors would, of course, require setting up a dedicated spectrometer for each end station, so the total investment would increase as long as a spectrometer is demanded by every end station. The final decision will have to include a detailed consideration of the costs of the mentioned subsystems with respect to the total cost of the spectrometer to figure out an optimal choice of its final position.



The current design of the spectrometer and its subsystems has already proven its baseline functionality during earlier experiments (Chapter 4), but we still see a high potential for future improvement. While the overall performance has still to be increased in some fields in order to meet the requirements at XFEL.EU, some other topics can be considered optional.

We give a summary of the scheduled topics here, roughly sorted by priority in descending order:

### ■ Adaptation to SASE 1/2 (Section 3.1)

While the design has been found to satisfy the needs at SASE 3 beamline widely, some mandatory modifications are indicated for use at SASE 1/2. The expected higher kinetic energies requires higher magnitudes of the applied retardation voltages. This results in higher stability requirements for the voltage supplies. At the present date, we assume that the ratings of ISeg modules allow for their application in a high-voltage version of the spectrometer as well. The attached circuitry has to stand higher voltages in this case, and the current design is already under review by DESY electronics workshop in order to increase the maximum applicable voltage to  $\geq 10$  kV. The flight tube elements probably need rounded edges and, in general, improved insulation from each other in order to avoid electrical breakdown. Some excess flight tube assemblies are available for related lab experiments.

### ■ Flight tube design (Section 3.1)

The general geometry of the flight tube will be subject to optimization in order to find an optimal solution, especially of the trade-off between transmission and best energy resolution. In particular, the size and shape of the opening aperture plays an essential role here. Since an updated flight tube geometry will require slightly different settings of the retardation potential, this topic will first be explored by parametric studies based on simulations according to those presented in Section 4.1. We expect that the tight requirements for magnitude and stability of the retardation potential can be relaxed when the total length of the flight tube is increased. Even though limitations to the outer dimensions of the spectrometer setup have to be respected (Section 3.7), this option will also be assessed by simulations in the future. New approaches, such as the application of resistive glass as a flight tube material, will be considered since, in this case, completely new opportunities of designing potentials could be opened.

Another important point comes from the problem that the gas pressure in the

interaction volume has to be highest possible, while it is confined to  $\leq 10^{-5}$  mbar near the detectors. One approach to maintain a high pressure gradient along the flight tube would be to establish a significant pumping cross section at its end. Possible solutions to this issue are still to be figured out.

#### ■ **Optimization of the flight tube settings (Section 4.1)**

The spectrometer is only as good as its optimal voltage settings. Therefore, we explored several options to optimize the settings of a certain flight tube geometry. For later operation, these settings will have to be optimized for the complete kinetic energy range obtained at a specific beamline. It would be convenient to provide different parameter sets to cover other competing needs as well, e.g. the size of the observed energy interval versus the energy resolution. Much of this work can be done using the simulation code developed in our group (Section 4.1), provided that it has been thoroughly checked and compared to reality. As a supporting measure, we already developed a strategy to optimize settings of the spectrometer during an experiment and demonstrated the general feasibility during beamtime.

#### ■ **Gas inlet (Section 3.4)**

As has been shown in [13], the stationary pressure gradient in the vacuum chamber is strongly influenced by the design of the gas inlet nozzle. It has particularly been shown that the setup might strongly benefit from placing an array of nozzles providing intersecting beams, so the pressure in the interaction centre can be maximized. Future developments will aim at an optimization of the geometry of the gas inlet.

#### ■ **Compensation of external magnetic fields (Section 3.6)**

Chapter Section 3.6 is dedicated to a discussion of approaches to minimize the effect of external magnetic fields acting on the electron trajectories. This essential topic will be discussed in detail on the basis of the arguments given there.

#### ■ **Removal of ions (Section 4.2)**

First simulations (Section 4.2) lead to the conclusion that the accumulation of ions in the interaction centre of the spectrometer might lead to critical concentrations of space charge with a significant electric potential. If this effect is validated, a strategy for the reduction of space charge has to be developed. A suitable approach would be to accelerate the ions along the beam direction by an external axial field. Here, it would be thinkable to apply an AC field, which is in phase with the pulse train. If the zero crossings of the field can be well-aligned with the pulse arrival, the electron-optical layout would not be perturbed. Considerations of such concepts are regarded as optional at the present date.

■ **Extended functionality of the spectrometer (Chapter 3)**

As mentioned in Section 2.2, only effects of photoemission in the dipole approximation are currently considered for diagnostics. As soon as understanding of, for instance certain non-linear processes, improves and has been validated, it could also be considered for application in the field of diagnostics in order to determine further physical properties of the photon beam. Especially the questions to which extent non-linear processes can be expected in the unfocused beam, i.e. at relatively low peak intensity, will have to be figured out.

## 3.9 Digitizer and online data processing

As presented in Section 3.2, photoelectrons are detected using microchannel plates (MCP) in a Z-stack configuration. Every electron hitting the detector is amplified by a typical factor of  $10^6 - 10^7$ , so a macroscopic voltage pulse can be measured for every electron. The number of registered photoelectrons per shot is a function of gas pressure, the number of photons per shot, and photon energy. The latter determines the relevant photoionization cross section, which varies by roughly 4 orders of magnitude over the full energy range of XFEL.EU, and of course depends on the currently used gas. The spectral distribution of XFEL.EU radiation might be represented by only 100 – 1 000 electrons detected during the maximum observation time of 222 ns after a pulse.

Therefore, the measured voltage over time has to be recorded with a reasonable sampling rate in order to obtain the full information available for a single FEL pulse. As has been shown during earlier beamtimes at synchrotron facilities, the typical response of the detector to a single photoelectron is an asymmetric voltage pulse (see Figure 3.8) with a steep raising flank and a relatively slow exponential decay. A full width at half maximum of the pulses in the range of 1 ns has been achieved with the current setup. Preamplifiers close to the detectors are applied to raise the amplitude of such a pulse to 100–200 mV typically, and a considerable individual spread of up to  $\pm 50\%$  has been observed here.

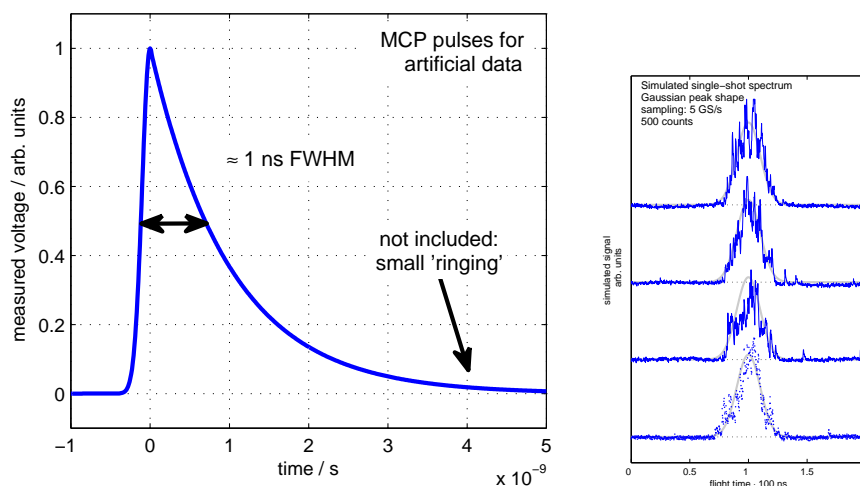


**Figure 3.8:** **Left:** Schematic shape of the single-electron response from the MCP detector as discussed in the text. **Right:** Artificial ToF spectrum as expected at count rates of 500 per photon pulse.

### 3.9.1 Digitizer requirements

The observed FWHM duration of single pulses from the MCP detectors gives a measure of a reasonable sampling rate. Since the integrated amplitude of a pulse contributes to the signal, it needs to be determined within a sufficiently small statistical uncertainty here. Thus, the sampling frequency of the digitizer has to be considerably greater than 1 GS/s. We find that a reasonable trade-off between the resulting data rate and the required precision would be provided by choosing a sampling rate of 4–5 GS/s.

The effective bit resolution of the digitizer defines the dynamic range of registered intensities. The relatively low number of events per single shot, spread over the bunch spacing of 222 ns, lets us expect a very spiky spectral structure (see Figure 4.10), where the amplitude of single pulses will consume a large part of the complete dynamic range of the digitizer. Furthermore, electronic noise of 10% of the spike amplitude is assumed in the artificial data.

The dipole characteristic of photoemission (see Section 2.1), which can be exploited for measurements of polarization, will cause an angular modulation of the detected signal between 0–300% of the average signal, depending the orientation of the spectrometer with respect to the vector of linear polarization. The SASE process will produce significant pulse energy (i.e. photon number per pulse) fluctuations, so some dynamic range of the detector system and electronics has to be reserved for this.

Taking all these effects into account, we conclude that a dynamic range of the digitizer of  $\geq 10$  Bit is necessary here. The range of voltages to be mapped by the digitizer can only be estimated roughly and should be on the order of 1–2 V. Drifts and temporary charging effects might result in a non-zero baseline, so a small bipolar range should also be covered. As an alternative, a small bias might be applied to the signal, so a unipolar operating range of the digitizer could be used. However, the signal level could still be adjusted to the input voltage range of the actually available digitizer by the choice of the pre-amplifier, its supply voltage, or the operating voltage of the MCPs.

Data Acquisition and Control group (WP-76) currently has digitizers with typical parameters 5 GS/s with 10 Bit nominal resolution or 3.5 GS/s at 12 Bit nominal resolution under consideration [23], so the final choice should give appropriate ratings for the needs of the photoemission spectrometer.

### 3.9.2 Expected raw data rate

A ToF spectrometer determines the kinetic energy of a photoelectron by measuring its flight time from the position of creation (the geometrical centre of the assembly) to the detector. By applying retardation potentials, the flight time as a function of kinetic energy is tuned such that small differences of energy give large differences in flight time. In practice, the relevant kinetic energy range is mapped to flight times between 0–222 ns, so the complete inter-pulse interval is covered. Limiting the time interval to a shorter period would introduce an unnecessary limitation, so the best choice is to sample the data continuously during a pulse train.

With the specifications given in the previous sections, the data rate per second can be estimated as shown in Table 3.5:

<ul style="list-style-type: none"><li>• 5 GS/s</li><li>• 12 Bit resolution</li><li>• 220 ns per TOF-spectrum</li><li>• (Up to) 16 channels</li></ul>	<b>Raw data rate per channel*</b>	
	1100	Samples / shot
	56.5	MB / s
	4.65	TB / d
	1.66	PB / y

\*Assuming 16 bit integer numbers and 24/7 operation

**Table 3.5:** Estimation of the single-channel data rate

Obviously, this data rate is extremely hard to handle and would lead to enormous amounts of required storage space, especially because this estimation includes only a single data channel and a fully equipped spectrometer would provide 16 of these data streams. Modern network technology would allow for real-time transport of this data to a remote computer. In the latest version of the TGA room book [32–34], four optical fibres with a capacity of 10 GB/s each are foreseen for this purpose per beamline. Still, the amount of information contained in this data would not justify occupying that amount of resources. In addition, the specifications of the device includes providing “nearly real-time” diagnostics to the user with lowest possible latency. The goal is to achieve values in the low  $\mu$ s-range, which calls for an effective way of processing these huge amounts of data. In conclusion, a low-level processing routine for the raw data is required to achieve a strong reduction of the data rate. An appropriate algorithm must not be too complex because it has to handle the full data stream in real time. In order to grant deterministic, low latency time, implementation of a simple processing scheme on a field programmable gate array (FPGA) chip is highly recommended. An approach to solve this issue will be presented in Section 3.9.3.2.

### 3.9.3 FPGA-based data processing

In this section, we show that essential tasks of online data processing can be done on an FPGA chip, so short and well-defined latency of the evaluation can be achieved. Some parts of the proposed methods are supposed to be performed on an external PC. This applies only to tasks that are not time-critical and can be performed asynchronously. Intermediate network bandwidth should suffice here, so the overall performance is expected not to be limited by the data transfer between the FPGA and a PC.

#### 3.9.3.1 Data binning

For any evaluation of a ToF spectrum, a conversion of measured flight time to kinetic energy is crucial. This will be performed by using a calibrated curve for the current spectrometer setting, which is, in general, similar to the relations obtained from Equation 2.7, or in the general case, Equation 2.9. A showcase configuration is also discussed in Section 4.1. Due to the non-linearity of this relation, the conversion to an equidistant, linear energy axis from the given time-of-flight axis would require an interpolation of the measured intensity. Besides the problem of requiring relatively large computation power, this method would fail when the data is noisy. In such a situation, binning of subsequent data points would be indicated anyway. The conversion from time to energy can easily be integrated into the binning process, when the individual bin sizes are chosen accordingly to the dispersion relation, so the bins represent equidistant energy steps. Data binning is a sequential process, so it could already start during data acquisition and should therefore cause only an insignificant latency in the processing chain. Integer bin sizes cannot map specific energy intervals perfectly, but the resulting round-off error becomes smaller with higher sampling rate. Here, binning would limit the amount of raw data to be processed and transported. While a reasonable temporal resolution was derived from the detector output before, this way of processing raw data could clearly benefit from a higher sampling rate.

#### 3.9.3.2 Data reduction

One main goal of low-level processing of spectroscopic data from the photoemission spectrometer is to reduce the amount of storage space and network capacity required to provide diagnostic data to the user end stations. In this section, we outline an effective method for compressing the data down to a fraction of its former volume without losing vital information. The method is based on an alternative representation

of the individual spectra in the scope of a large set of single shot spectra, e.g. from a full bunch train, as will be outlined in the following. The method originates from the field of data mining and is applied whenever the essentials of a large volume of noisy data has to be analysed. Introductions can be found in various textbooks from that area [16–22]. Especially for electron spectroscopic data, it has been successfully applied during spatially resolved photoemission spectroscopy studies (PEEM) from structured surfaces [14]. As the foundation of a discussion of a case study on data processing for artificial electron ToF spectra (Section 4.3), a brief summary of the mathematical background will be presented here.

Technically speaking, a spectrum is a sequence of  $N$  data points, so it can also be interpreted as components of a vector in  $N$ -dimensional space containing every possible spectrum. A set of single-pulse spectra, e.g. from a complete pulse train, including all known variations, makes up a statistical sample of the actual,  $N$ -dimensional distribution of data. The task is to find the essentials of this distribution and to give a reasonable representation of these in order to separate uncorrelated effects such as statistical noise, drift, etc. from systematic variations.

The most trivial feature of the distribution is its centre of gravity. Subsequently, the approach requires finding the directions with the highest variations among all samples, i.e. to determine the main “axes of inertia” of the given set. These can be determined iteratively by a well-known algorithm: Given the data set with the centre of gravity removed, it gives the spatial direction in which the standard deviation of all points is maximized. Afterwards, all data points are projected into a  $N-1$ -dimensional hyperplane perpendicular to this direction, and the procedure is iterated. The result is a set of perpendicular vectors representing the first main axes of the distribution. After  $N$  iterations, a complete affine basis with the centre of gravity as the origin has been determined. Every spectrum  $S$  is then represented exactly by the expansion

$$S = s_0 + \sum_{k=1}^N \beta_k \cdot s_k, \quad (3.5)$$

where  $s_0$  is the centre of gravity and  $s_k$  are the main axes of the distribution in a descending order of variance. In practice, i.e. in the presence of statistical noise and other uncorrelated side effects in the data, the standard deviation will not drop after a few (typically  $\leq 10$ ) iterations, indicating that the data set has a spherically symmetric distribution in a subspace with only a few dimensions less than  $N$ . This means that no further correlations can be extracted from the data, and that the rest is dominated by statistical noise. Therefore, this method offers an efficient way to separate the desired, systematic variations in a spectrum from the undesired, statistical ones just by truncating the expansion after a few terms.



An essential effect of this approach is that a complete spectrum is represented in the new, truncated basis by just a few coefficients  $\beta_k$  instead of  $N$  data points. This is where the high potential for a reduction of the complete amount of data results, as can be seen from the two examples found in Table 3.6. The reduced data is represented by the coefficients and the truncated set of basis vectors, so the amount of memory space required for the representation basically depends on the number of base vectors and the number of individual spectra that are represented in that basis. For the moment, we assume that the spectral distribution changes with time, so frequent updates of the basis become necessary for an optimal representation of the data. The parameters of data acquisition were chosen in accordance to the table in Section 3.9.2.

Realistic case		Worst case	
5 dim, 100 trains per basis		10 dim, 1 train per basis	
(i.e. new basis every 10 s)		(i.e. new basis for every train)	
<b>Memory space</b>			
Raw data	566.5 MB	5.67 MB	16 Bit integer
Basis set	5*1100	10*1100	double
Reduced spectra	5*2700*100	10*2700	double
Total	10.34 MB	0.29 MB	
Compression	1.8 %	5.1 %	

■ To compare: artificial data in binary file can be compressed to 44% using 7ZIP

**Table 3.6:** Expected ratios of data reduction

Even in the worst case with respect to data reduction, where one basis set is applied to the data obtained from only one pulse train and is updated for each pulse train, the combined amount of data from basis vectors and expansion coefficients is approximately 5% of the original data volume. Since the determination of a new basis requires a remote PC working asynchronously (which will cause a significant latency), the high update rate of the basis implied here is not realistic. Moreover, considerably better results are achieved with a much smaller update rate, so the spectra from many pulse trains are expanded in the same basis. For better comparability, it is desirable to reduce the number of basis updates as much as possible. Note that a new basis in general becomes necessary only to grant an optimal representation of the experimental data. As long as the free-electron laser works in a stationary state and the settings of the spectrometer are not changed, presumably no updates will be necessary at all.

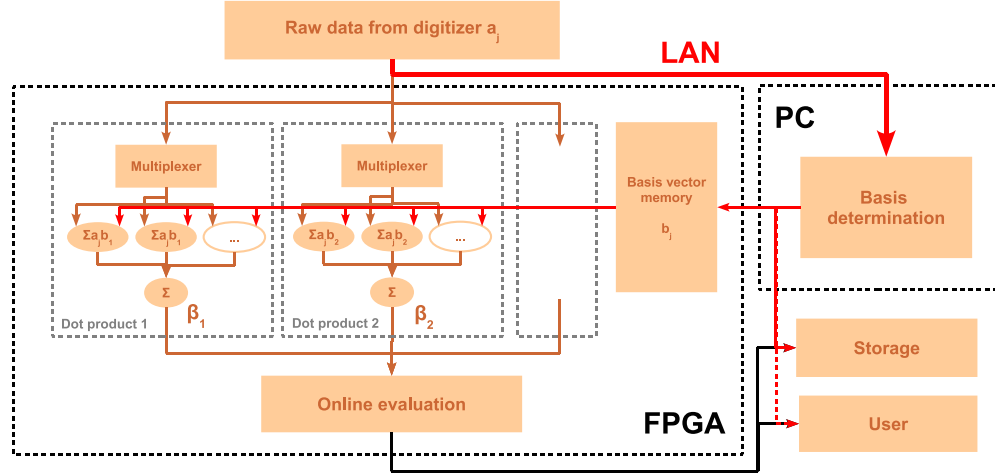


**Figure 3.9:** Schematic interplay of low-latency FPGA computing and asynchronous microprocessor-based computing for data reduction of the ToF spectra. Note that the raw data will need to be transported to the PC only during basis updates, i.e. in rare cases.

The results of the proposed processing scheme are presented in Section 4.3. Further implications are discussed on the basis of artificial data there. We will now focus on some details of the implementation of this scheme. The determination of an alternative basis of a given set of spectra is performed by an iterative algorithm that requires a reasonable amount of operations and therefore runtime. Furthermore, it does not terminate after a fixed time, which may be critical in a real-time environment. Due to its complexity, a PC platform rather than a FPGA chip is preferred here. The only requirement is to have then an option to transport the raw data of a reasonable number of spectra from the diagnostics station in the tunnel to the PC, which will most likely be located in the experiment hall. As mentioned above, the full data from selected pulse trains with 2 700 pulses can be expected to suffice here. For this purpose, dedicated high-capacity optical fibres will be installed in the tunnel [32–34]. A first, schematic layout of the complete data reduction system as described here can be seen in Figure 3.9, which has a focus on the simple software architecture implemented on the FPGA.

After a basis for the reduced representation of data is determined, a new spectrum  $r$  must be projected into that basis. Given normalized base vectors, the coefficients  $\beta_k$  can easily be determined by computing the dot product of that spectrum and the basis vectors:  $\beta_k = s_k \cdot r$ . This operation can be performed for every base vector in parallel, and it only applies multiplications and summations. In addition, it works strictly sequentially, and even the computation of a single dot product can easily be split into several parallel threads. Therefore, it is an ideal candidate for implementation on an FPGA chip. The fact that a single dot product can be parallelised allows for

matching the throughput of the chip with the data acquisition rate that would otherwise be significantly lower. This means that no FPGA-internal buffer memory would be necessary, but only a fast multiplexer to distribute the incoming data points on the parallel multiplying units. Since the computation of a dot product is strictly sequential, data processing can already start after the first value is passed from the digitizer, so this basic processing step can be realized with a very low total latency. Theoretically, the data reduction step could be over shortly after the spectrum is recorded. The low expected latency allows for the creation of VETO signals, which is discussed in Section 3.9.5. After the coefficients  $\beta_k$  are determined, they are sent to the adjacent layer of online data analysis or via the network to storage. Another option would be to supply the data to the user end stations for further processing. The arrival time of the reduced data at a remote recipient is expected to be dominated by the overhead of the networking infrastructure.

The complete flow diagram of this low level process is shown in Figure 3.9. Besides its connectivity and the parallelised calculations of dot products, the FPGA chip would need buffer memory for the currently applied basis vectors. A connection to the external PC would be needed for basis updates. As only the data reduction step has been outlined with the data so far, some strategies of data evaluation based on reduced data are introduced in the following sections.

### 3.9.4 Online analysis of spectroscopic data

The dramatic reduction of the data volume acquired per shot that can be achieved with the approach introduced in the previous section potentially allows the analysis of spectroscopic data within a very short time and with very low latency (A serious estimate of these values can be done as soon as the design of the data processing chain advances). To this end, any processing algorithm has to operate on the reduced representation of the data, so a reformulation of standard algorithms might become necessary. Analysis of spectroscopic data is often performed by fitting a known analytical line shape to the data in order to determine parameters such as line centre, line width etc. Due to the fact that this technique is based on iterative algorithms solving the problem of least-squares minimization, it cannot be implemented easily in a time-critical environment with a high level of automation, since convergence of the algorithm within a certain processing time cannot be granted. Furthermore, the assumption of an analytical profile would artificially constrain the results to a specific shape, which would obviously limit the amount of information that can be obtained from experimental data. In general, the stability of such an algorithm cannot be granted for arbitrary input, so user-provided supervision of the fit result would be mandatory.

Any approach to the spectral analysis that can be made here is highly recommended to be based on linear operations in a mathematical sense, so if the measured spectrum is represented in its reduced form, processing can be performed on its components, i.e. the basis vectors separately, which would then be necessary only once per basis set. Again, concepts from data mining and machine learning need to be considered here. For instance, arbitrary, non-linear relationships between the spectral components in the reduced basis and relevant quantities, such as spectral width, might be subject to a machine learning procedure, where the data that served for the determination of a reduced basis also acts as a training set. Subsequent data could easily be assessed in this scope without applying complex algorithms, so implementation on an FPGA platform becomes possible.

The computation platform for any operation has to be chosen depending on complexity and runtime requirements. Any iterative algorithm, for instance, will be executed on a microprocessor architecture, while any time-critical task is best executed on an FPGA. The complete implementation will most likely require both, so good connectivity between the two domains is essential for the successful design of an analysis procedure. The requirements and the actual features of such an analysis framework are still subject to discussion. The detailed design of procedures can start as soon as the demanded features have been figured out.

As was outlined earlier (Section 3.3), the spectrometer design allows for precise measurements of the linear polarization of the photon beam. From the perspective of data analysis, this requires only the determination of the phase of the sinusoidal modulation (Figure 2.1) of the total photoelectron yield across all spectrometer channels. The obvious solution to use curve fitting for this task can be replaced by a deterministic, non-iterative approach, which again has a high potential for FPGA implementation. Since all the required information is potentially available for a single photon pulse, it would even be possible to provide a single-pulse polarization analysis. We will give a detailed outline of the suggested method in a future design report.

In general, we can distinguish between concepts of data evaluation concerning the data from a single channel and those merging multi-channel information. Therefore, it would be conceptually convenient to run several layers of FPGA chips in order to separate low-level processing, such as data reduction, from high-level evaluation, such as the determination of the polarization vector. The FPGA and digitizer modules, which are currently under consideration by WP-76 to make up a future XFEL.EU standard, support cross-linking and would also include an interface to a microprocessor (PC) platform. Therefore, we are optimistic that a suitable hardware platform for the implementation of our concepts will be available in the future.

### 3.9.5 Generation of VETO signals

As a consequence of the statistical nature of the SASE process, the radiation pulses at XFEL.EU are expected to include statistical fluctuations, which motivates the establishment of single-pulse diagnostics. Since the buffer memory capacity of the imaging detectors at the experimental end stations is limited, only a fraction of the experimental data obtained during a full pulse train can be kept. Therefore, it is highly desirable to save only those data from individual pulses that promise a successful measurement. For photon diagnostics, this means to select pulses from the train with specific spectral features, i.e. to generate a request to the detector to dismiss the just acquired data in case a pulse does not satisfy a certain criterion. In this sense, the generation of VETO-pulses can be seen as a special case of online diagnostics, but with an even stronger focus on short response time, again calling for an implementation exclusively based on FPGAs.

The same requirements discussed in the previous section for the implementation of an algorithm apply here as well. In this case, the spectroscopic data will simply be used to generate a flag. A clustering technique operating on the reduced data is suggested here to define the volume of “accepted” pulses in the associated vector space. The actual clustering would be performed on an external microprocessor with given “training” data, while the rating of new spectra could again run on an FPGA chip (only deterministic, linear operations). The input of an appropriate algorithm is a set of reference spectra that are considered “accepted” and a complementary set that is “not accepted”. The criteria for this decision could also be defined dynamically by the user, which would allow for tweaking of the VETO generation system during operation. As a simple example, the user might want to use only “common” pulses, i.e. those which do not deviate too much from the mean spectrum. In that case, a criterion for VETO generation would read

$$\sum_{k=1} \beta_k^2 \leq R^2, \quad (3.6)$$

where  $R$  is the radius of a sphere around the mean spectrum in the vector space of reduced data. The fraction of accepted spectra per pulse train could be tuned here by the choice of  $R$ . We assume that the computing time for such a criterion executed on FPGA basis might lead to latencies in the  $\mu s$  range, which makes it fast enough for VETO generation.

Of course, diagnostics at the spectrometer supplies VETO signals derived from a limited perspective, but these signals could contribute to a larger system spanning any relevant available online diagnostics data.

### 3.9.6 Summary

We outlined the requirements for data acquisition electronics as derived from the demands to the connected hardware. Based on this, the expected raw data rate could be estimated. We discussed the feasibility of data transport and real-time processing of the spectroscopic data. Here, we demonstrated that severe problems with network bandwidth and computing power can be circumvented if data reduction is applied to the raw data. We presented a first draft of concepts for online data analysis, which is based on the reduced representation of the data. Special attention was paid to the demand for low latency processing, for instance for VETO generation. In conclusion, we are optimistic to provide this feature with single-pulse resolution by massive use of FPGA electronics. We presented first concepts for convenient algorithms on such a platform, which will be tailored to meet user-defined specifications in the future.

## 3.10 Breakdown structure of subsystems and automation

In the previous chapters, various technical issues to be solved for successful construction of a ToF spectrometer for photon beam diagnostics are figured out. The complete project is split into specific subsystems with specialized tasks, such as the gas dosing system, or the data acquisition system. In this chapter, we will focus on interactions between those subsystems and how they interface further components of the beamlines using standardized hardware and software interfaces to be developed by WP-76. At the current state of development, we can outline only dependencies because actual implementation of any infrastructure is pending. The chart in Figure 3.10 gives an overview of the vital components of the spectrometer and how they will be embedded in XFEL.EU. Despite being a specific piece of hardware, we refer to a subsystem here as the implementation of a specific functionality, including hardware and software.

The representation of hardware components of the spectrometer setup is found at the bottom of Figure 3.10. These components are obviously interfaced by dedicated software controls. Any interaction of control software with remote hardware is intended to be implemented on the basis of the beamline control system defined by WP-76, which itself is based on the EtherCAT field bus by Beckhoff Automation GmbH. The “Spectrometer Control Software” will control the entire functionality of the system and implement the external interfaces.

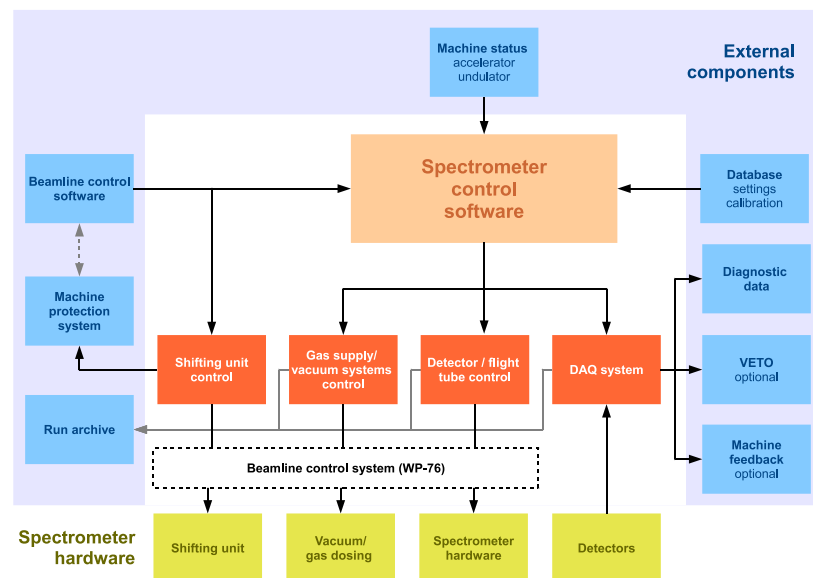


**Figure 3.10:** Outline of the modules of software control and automation for the ToF spectrometer, including required internal and external interfaces.

For every subsystem, we currently foresee both a representation by a graphical user interface (GUI) and a software interface. The GUI will not be required for user interaction during development only, but also for later operation in non-standard situations. Since the operation of every system will require certain expert knowledge of the technical details, we aim for a high level of automation. Both manual and automatic operation require a robust error handling (see also Section 5.2), which should be considered already at the stage of software architecture.

On the basis of the given chart, we will now give a summary of the relations between the components. Details of the functionality are given in the referenced chapters.

### 3.10.1 Shifting Unit Control (Section 3.7)

Includes any logic to drive motors and for position readout.

#### Interactions with ...

##### ■ Beamline Control System

Motion of the shifting unit must be harmonized with the settings of the offset mirrors, which is its essential input. The module does not depend on spectrometer operation or vice versa, so it conceptually belongs to beamline controls.

##### ■ Beam Protection System

The safety relevance (Section 5.2) of the spectrometer position calls for an integration of the control into the Beam Protection System.

### 3.10.2 Gas Supply and Vacuum Systems Control (Sections 3.4 to 3.5)

Implements gas dosing, i.e. control of valves and pumps, pressure readout, and feedback loop for pressure stabilization.

#### Interactions with ...

##### ■ Spectrometer Control Software

Via its interfaces, the subsystem receives input such as the selected target gas and a pressure set point.

##### ■ Run Archive

The state of valves, pressure readings, last commands, etc. could be logged on demand. Superior software modules, such as the main spectrometer software should be bypassed then.



### 3.10.3 Detector and Flight Tube control (Chapter 3)

Low-level communication with voltage supplies (flight tubes and detectors) and related functionality.

#### Interactions with ...

- **Spectrometer Control Software**

The module receives voltage settings and can be consulted for attached hardware. Logical voltage channels, such as “Tip segment of spectrometer N”, should be mapped internally to a physical channel.

- **Run Archive**

Diagnostics data can be evaluated later only if the configuration of the spectrometer is known. Therefore, low-level logging of the applied voltages is suggested.

### 3.10.4 DAQ System (Section 3.9)

The DAQ subsystem includes the digitizer and online data evaluation hardware, as well as the FPGA software. Additional microprocessor architecture is likely. Low-level parametrization of online processing via a software interface is highly desirable.

#### Interactions with ...

- **Spectrometer Control Software**

Essential parameters of the data evaluation process, such as the update rate of the data reduction basis, are received as input. Updates of this basis can also be triggered externally.

- **External Components**

Processed output of the diagnostics systems is directly sent to the outside world on a low hardware level in order to assure low latency.

- **Run Archive**

Diagnostics data will have to be uploaded to the run archive for later access by users.

### 3.10.5 Spectrometer Control Software

Provides high-level functionality and is the major interface to components of the beamline.

#### Interactions with ...

##### ■ Machine Status

The current status of the machine acts as essential input to the spectrometer because it provides an expected photon energy. The module will select suitable settings of the spectrometer depending on this input.

##### ■ Database

A database will be used to recall spectrometer settings for a specific machine status. These settings are then passed to the hardware-controlling subsystems. The settings therefore include a gas, its pressure, flight tube voltages, and energy calibration.

##### ■ Beamline control

Since the spectrometer provides a service to the users, it will most likely be remote-controlled by some future master beamline control software. Therefore, especially this main module has to implement external software interfaces.

##### ■ Subsystems

As discussed above, the subsystems mainly receive input from the main module. High-level functionality of the subsystems should be exposed via interfaces, while the microscopic functions, such as opening and closing of specific valves, should be possible only internally or through the graphical user interfaces.

The outline as given in Figure 3.10 and the specified interaction between the modules will be refined in the future in order to derive the actual software interfaces in a close collaboration with the responsible colleagues in WP-76. Control software will be needed as soon as the first commissioning beamtimes are scheduled. This will provide a good opportunity for testing under realistic conditions. Since all the subsystems will be developed in parallel, the general software architecture should be defined soon, so as much program code as possible can be reused in the final design.

---

## 3.11 Calibration procedure and planned commissioning

In this section, we give an outline of future commissioning procedures as far as we can foresee it today. Commissioning of the ToF spectrometer is interpreted in a wider sense, since this also includes dedicated beamtime at other light sources, such as synchrotrons and FEL facilities, during the development phase. First proposals for 2012 have been accepted, and the timeline is still developing. We give a summary of the planned steps here. During the operation at XFEL.EU, the spectrometer setup will require regular maintenance, which is also included in the relevant paragraphs.

### 3.11.1 In-lab testing procedures

Various issues related to the spectrometer can easily be tested in the lab without using a light source, so essential feedback to the design process can be given within a short time. The scheduled tasks are:

- **MCP detectors**

Essential properties of individual MCP stacks have to be assessed before using them at a light source. This especially includes a calibration of the gain curve, characterization of dead time, and non-linearities faced at high signal intensity. Strategies to equalize the performance of the detectors in every flight tube have to be developed and applied.

- **Long-term stability of detectors**

The final detector design including supplies must have a high stability concerning noise, drifts, and ageing. We will address questions of the long-term degradation of MCPs and possible effects of, e.g. laterally inhomogeneous ageing.

- **Electron optics**

Using a continuous or pulsed electron beam source, for instance a RHEED gun, the electron-optical performance of the flight tubes can be assessed in order to identify further limitations of energy resolution, i.e. any effects that have not been addressed during the simulations. In addition, this will also support the production process, e.g. by determining the effect of mechanical tolerances of the flight tube assembly.

- **Magnetic fields**

The compensation of external magnetic fields is a partially open issue. New approaches could be tested in the lab by employing the electron gun as a source.

#### ■ **High-voltage toughness**

The current flight tube design has to be tested with respect to its high-voltage toughness, since the SASE 1/2 version needs to stand significantly higher voltages than tested so far. If indicated, the layout will have to be updated.

### 3.11.2 **Synchrotron radiation (VUV and X-ray)**

First tests of the spectrometer at synchrotron radiation facilities have already been performed and are also scheduled in 2012. Related experiments will be conducted over the complete development phase because synchrotron beamtime can be expected to be available on a regular basis. Depending on the test case, the available photon energies and intensities are expected to be sufficient for tests of specific features. Planned experiments include:

#### ■ **Test subsystems**

Specific subsystems, such as the gas dosing system and the actual injection geometry, will be evaluated during regular spectrometer operation. The related measurements will be done in the context of our scheduled beamtimes.

#### ■ **Tests of fast DAQ systems**

Light pulses at a synchrotron have usually small time intervals and are produced continuously. Under these conditions, any timing-relevant topic can be tested reliably. Therefore, the development of the fast data acquisition system will be accompanied by tests at synchrotron facilities.

#### ■ **Validation of simulations**

The design of suitable settings of the flight tube can comfortably be done using electron-optical simulations. This approach is highly desirable because of the high number of degrees of freedom in the system. Previous and future comparisons with experimental data aim at a validation of the simulations.

#### ■ **Spatial alignment**

The spectrometer calibration is valid only for a well-defined source of the photoelectrons. At a larger scale, the transmission of a flight tube is reduced for large displacements. During an upcoming beamtime (scheduled first half of 2012), we will figure out the position sensitivity and resulting precision requirements of the spectrometer chamber for intermediate kinetic energy ( $\leq 1\,500$  eV).

- **Ultimate energy resolution**

The ultimately achievable energy resolution of the spectrometer can be determined only during an experiment, since simulations cannot account for all side effects such as magnetic fields, mechanical misalignment, beam profile, etc.

- **Validation of electron-optical configuration**

Settings of the flight tube for specific kinetic energies can easily be developed using simulations. However, they have to withstand the experiment.

- **Determination of spectrometer settings**

From an extremely simplified model of the electron-optical system, a semi-analytical expression for the flight time as a function of kinetic energy and retarding potential can be derived. As was shown earlier, this greatly supports the tuning of the retarding potential during experiments, i.e. without performing the full-featured simulation. Therefore, the optimization of the potentials will also be done during an experiment.

- **Energy calibration**

The essential calibration data of a spectrometer setting is the relation between measured flight time and the associated kinetic energy, for which high-precision calibration measurements are inevitable for later use at XFEL.EU.

### 3.11.3 Free-electron laser facilities

Some features of the spectrometer can be commissioned only under nearly-realistic conditions close to the expected photon beam properties at XFEL.EU concerning the unique combination of pulse energy and photon energy. Therefore, extended commissioning at FELs is planned. We suggest the following activities:

- **Non-dipole photoemission**

The breakdown of the dipole approximation of photoemission has been demonstrated for several special cases at low photon energy, and we expect strong effects at higher photon energy as well. The resulting effects on the emission geometry (Section 2.1) could be exploited to enhance the efficiency of the spectrometer: In case of a pronounced non-dipole characteristic of the emission, maximum emission can be observed at a considerable angle versus the azimuthal plane (i.e. the current geometry). This rather unexplored field opens up options for basic scientific research using the spectrometer.

#### ■ **Non-linear effects**

Non-linear effects of photoemission including multi-photon and/or multi-electron transitions have attracted much attention in the past years and are still subject to current research. Since the available references cannot easily be generalized, influences of non-linear photoemission will have to be characterized for our specific device. A certain scientific relevance of experiments in this field can be expected. Aside from the expected complications for diagnostics, the physics of non-linear photoemission also grants potential access to additional photon beam properties (such as pulse length), that cannot be probed with linear photoemission. As the physical understanding of these effects improves, the spectrometer might even be employed to probe a wider range of beam properties. As a preparatory measure, the relevance of non-linear effects in the unfocused XFEL beam, i.e. for the expected beam at the future position of the spectrometer, has to be estimated.

#### ■ **Space charge**

Space charge, as it is made up by an accumulation of relatively slow ions, becomes relevant at extremely high photon flux. First simulations show that the magnitude of the resulting potential strongly depends on the pulse structure of the source, so a pulse-train bunch pattern (e.g. FLASH, even though the intra-bunch pulse rate of XFEL.EU is not achieved [68]) is necessary here for dedicated measurements.

### 3.11.4 **During XFEL.EU commissioning**

After the spectrometer has passed the suggested testing and calibration procedures at other light sources, the device will have to be installed at its final position. Installation will be finalized by repeated checking of the performance. Due to uncertainties of the preceding development process, we can give only a preliminary, incomplete list here. Accessibility of the final position in the photon tunnel will be limited. Therefore, any essential component will have to undergo strict final performance tests. Our scheduled activities during commissioning are:

#### ■ **Spatial alignment**

Spatial alignment will have to be checked using the first beam. Before that, the shifting unit that moves the spectrometer chamber will have to be cross-calibrated and synchronized with the movement of the offset mirror in the beamline in order to avoid beam blocking.

#### ■ **Check calibration**

Besides effects of the individual beam profile at the final position of the spectrometer in the photon beamlines, the validity of the calibration will be affected by small effects from the environment, e.g. the local magnetic field. Therefore, any calibration data of the spectrometer will have to be checked and updated when the setup is in position. A reference source such as an electron gun integrated into the setup might be reasonable during the commissioning phase of the beamlines.

### 3.11.5 **Recurrent procedures**

Once the spectrometer setup is under operation, its performance has to be controlled regularly in order to grant machine safety and to update the calibration if necessary.

Therefore, the measures proposed here mainly cover maintenance:

#### ■ **Matching detector sensitivity**

The long-term degradation of the MCP calls for regular matching of the overall sensitivity of every detector in the spectrometer. After a certain operation period, MCPs will have to be exchanged. The detector design would allow for the replacement of a detector assembly during a service day, so, provided that sufficient spare parts are available, detector maintenance could be done in the lab.

#### ■ **Maintenance of spectrometer**

The preamplifiers used in the prototype of the spectrometer need to be checked and eventually replaced on a regular basis. The same holds for the high-voltage supply modules. Service recommendations will be derived from test operation during development.

#### ■ **Replacing gas containers**

Consumables, like gas bottles, will have to be replaced regularly. An adequate number of gas containers should always be kept in stock. Depending on the accessibility of the location in the final design, gas containers can be exchanged at any time or only during service days.

#### ■ **Maintenance of vacuum system**

Especially the gas dosing system will make use of numerous remote-controlled valves, which will have to be checked for proper functionality, especially leak tightness. From time to time, the calibration of the pressure gauges should be controlled and readjusted, since the automated gas dosing system will rely on their readings. We will most likely make use of scroll pumps, which need regular maintenance, such as a replacement of the tip seals on at least an annual basis.





---

# 4 Feasibility

---

## 4.1 Simulations of the time-of-flight spectrometer

### 4.1.1 Electrostatic potentials

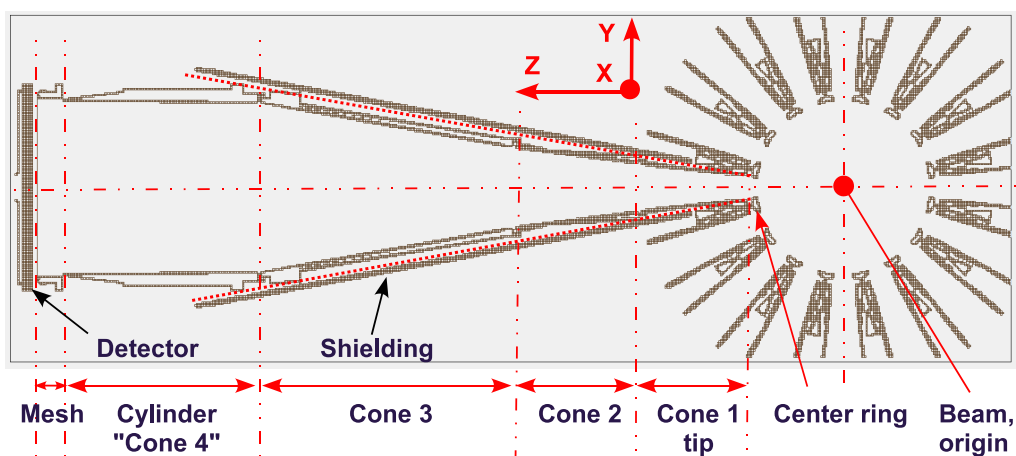
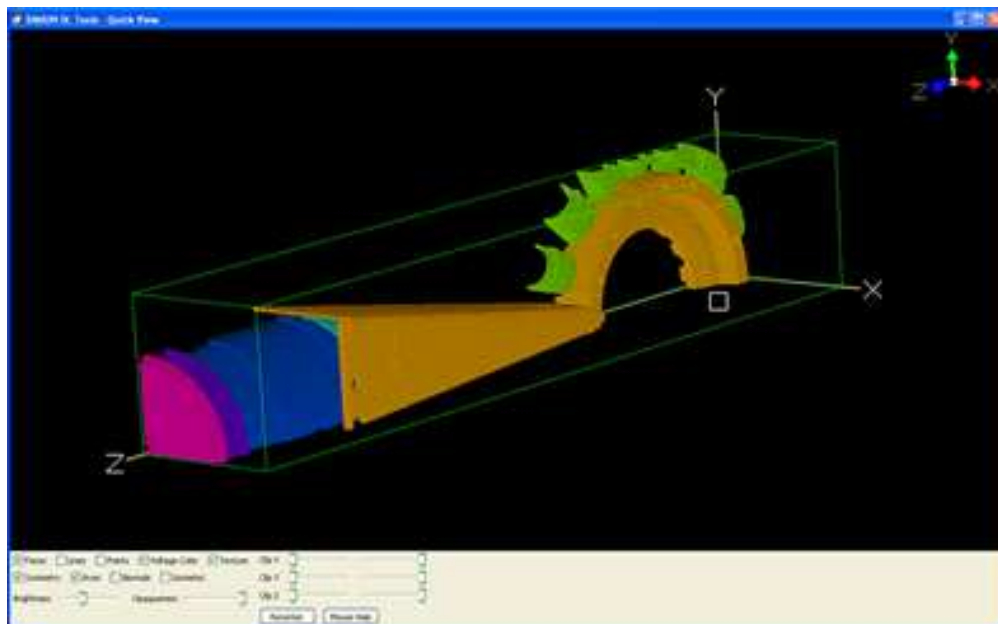
We now present simulations of the spectrometer, which are the basis of our development work. We will give an overview of past, and future work and discuss several aspects of the achievable performance based on recent work. Our studies were carried out with the SIMION electrostatics and particle optics simulation suite, which is a widespread tool in the field of electron analyser development. A SIMION model of the spectrometer could directly be derived from the existing CAD model by using the STL import feature of the software. Here, we exploit the double mirror geometry of the layout in order to save memory space.

Figure 4.1 shows the resulting quarter section after import into SIMION, from which the complete setup is derived internally. The bottom panel of Figure 4.1 shows the obtained cross section through the symmetry plane of the spectrometer, including the subsequently used notations and the definition of the coordinate system used throughout the simulations. The assembly was reduced to a single flight tube and the geometry around the centre ring. Including the correct geometry around the symmetry centre is essential to represent the nearby fields correctly. Since a significant stray field of the tip segments in the centre can be expected, all of its instances were included. Insulating parts of the assembly are omitted here.

The software provides numerical solutions of Poisson's equation of the individual parts of the given geometry. The electrically independent parts, also called electrodes below, are indicated in Figure 4.1. According to the linearity of the underlying equation, the electrostatic potential at every point in the model can be computed for any given voltage configuration of the flight tube by

$$\phi(z) = \sum_j c_j \cdot \phi_j(z). \quad (4.1)$$

Here,  $\phi_j$  are the independent, normalized solutions of Poisson's equations provided by SIMION, and  $c_j$  are the applied voltages of every electrode. Figure 4.2 gives an overview of the  $\phi_j$  along the symmetry axis of the flight tube.



**Figure 4.1: Top:** The model of the spectrometer after import into SIMION. Independent components of the electron-optical system are highlighted with different colours.

**Bottom:** Cross section of the flight tube model with applied symmetry.

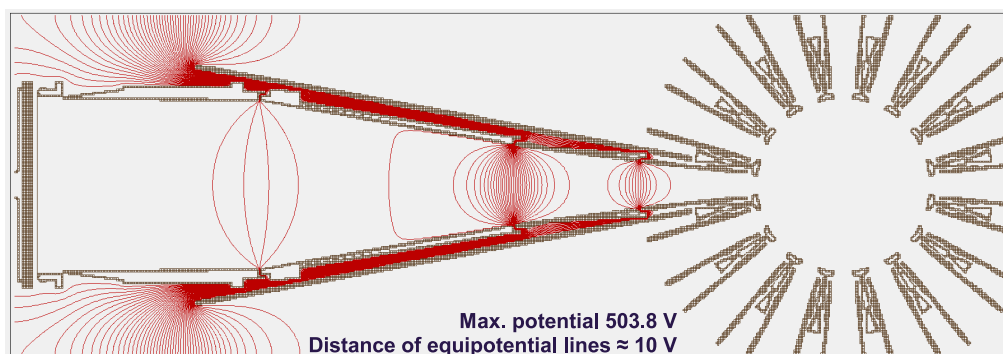
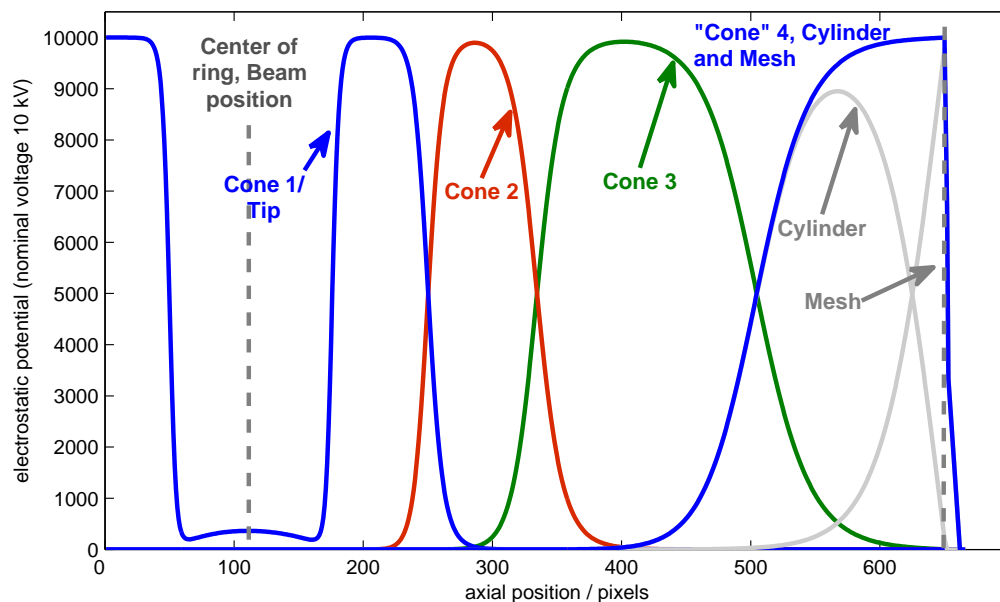


**Figure 4.2: Top:** Normalized potential distributions along the symmetry axis of the flight tube (Z-axis in Figure 4.1). The distance between the centre of interaction with the photon beam and the detector amounts to  $\approx 135$  mm (resolution of the model  $\approx 4$  pixels/mm).

**Bottom:** Equipotential lines of the electrostatic configuration mentioned in the text. The chosen geometry leads to strong curvature of the lines near the transitions between the elements, so electrons on off-axis trajectories are deflected.

For a given spectrometer layout, a suitable voltage configuration has to be found for every application in order to optimize the ratings like, for instance, energy resolution and transmission. Further issues will be discussed later in this chapter. Since every voltage in the spectrometer can be tuned individually, tuning the spectrometer to its best settings becomes an optimization problem in a high-dimensional space. To give an impression of the current status of this project, we discuss the performance of a specific setting in the following. The voltages given below were determined using a heuristic optimization algorithm with the given objective to optimize the performance of the flight tube for photo-electrons in the range  $505 \text{ eV} \leq E_{kin} \leq 520 \text{ eV}$ . Details of the method, including the definition of the objective, will be published elsewhere. The voltages applied to the electrodes are in this case:

Segment	Voltage / V
Inner ring	0
Cone 1(Tip)	-7.6
Cone 2	-130.8
Cone 3	-455.4
Cone 4 (Cylinder)	-503.8
Mesh	-503.8
Detector (front side)	-503.8

**Table 4.1:** Voltage settings of the ToF spectrometer for the showcase

Note that the screening is electrically connected to the inner ring in the current design. Cone 4 and the mesh in front of the detector could in principle have separate voltages, but are currently connected. In reality, an accelerating voltage is applied between the mesh and the detector front side, but the short distance between mesh and detector makes the flight time in this interval almost irrelevant. The chosen voltages have been determined during the development of the past year and have shown to perform quite well, as will be shown in the subsequent section. The potential distribution of the above mentioned configuration is visualized by equipotential lines in Figure 4.2. The lines have a spacing of roughly 10 V.

As can be seen in the figure, large gradients occur mostly near the transition between two electrodes. Their strong curvature is an inevitable consequence of the chosen mechanical layout. It can easily be seen that an electron on an off-axis trajectory in the flight tube will be deflected in this potential, so that flight time becomes trajectory-dependent. Since, in principle, electrons can travel from the interaction centre to the detector on various trajectories, the measured flight time becomes a distribution with a finite width, even for mono-energetic electrons. This effect is the major reason of limited energy resolution in the system. Therefore, we performed

detailed studies of the entity of electrons being detected in a certain configuration and their associated flight time distribution. This will be discussed in the next section.

#### **4.1.2 Electron-optical performance of a showcase configuration**

The main competence of the SIMION simulation suite is the simulation of electron trajectories in the potential of a given electrode configuration. Now, we will present a rating of the expected performance of the spectrometer in the configuration introduced in the previous section. This can naturally not be done with single electron trajectories, but with the entire set of possible trajectories ranging from the active centre (i.e. where photoemission takes place) to the detector. For any kinetic energy under consideration, the width of the flight time distribution has to be determined in order to derive values of the expected energy resolution.

Therefore, we need to choose a reasonable statistical sample from the accepted phase space volume of the spectrometer, i.e. the subset of starting points of electron trajectories that end at the detector. Since every spectral structure to be observed will have a finite energy spread, especially the resolution requirements must be satisfied within a certain range of kinetic energies. The complete simulation thus consists of a home-made MATLAB software that is capable of determining the boundaries of the accepted phase space volume as well as a representative set of start parameters. This software makes use of the SIMION simulation engine in order to determine the flight time and the end position of the electron, i.e. the position of a collision with either the spectrometer walls or the detector, but of course only the electrons hitting the detector are considered here.

Optimization of a flight tube setting is widely automated in the code and is basically a maximization algorithm for a score function implementing the different optimization criteria. Details of this framework will be published elsewhere. Using the mentioned MATLAB front end, computing efficiency is increased strongly, so we can easily assess a high number of configurations in order to find the optimum.

For the showcase presented here, we made the following assumptions for the model:

- The relative photon beam position is located in the origin of the model and parallel to the X-axis, so the spectrometer is perfectly aligned. We assume a flat-top beam with a circular cross section and a diameter of 3 mm. The pulse duration is assumed short with respect to the typical flight time in the ns range.

- Photoemission is assumed to be isotropic here (i.e.  $\beta=0$  in Figure 2.1, or unpolarized light). This also serves as an approximation of the relative intensity around the direction of maximum emission for  $\beta \neq 0$ .
- We assume a homogeneous pressure in the chamber.
- No additional potentials from space charge are included in the model.
- We assume a perfect detection efficiency over the complete detector area.
- Secondary electrons potentially emitted upon collisions of electrons with the inner walls of the flight tube are ignored. Instead, we assume a perfect absorption at the walls.
- Interactions between photoelectrons are ignored.

The phase space occupation of photoelectrons is made up by the beam dimensions and the emission characteristic (here: isotropic) defining the momentum distribution. The accepted phase space volume is a constant of the analyser given a specific configuration. The distribution of the detected photoelectrons can thus be computed by the integral photoelectron distribution inside the accepted phase space volume. The simulations require to find a representative set of trajectories from this constrained distribution. Features that obviously deviate from a true realistic setup can easily be included in the model in the future. For instance, the beam geometry represents a worst case configuration, since a more realistic, narrow, Gaussian beam would result in higher homogeneity of the trajectories and thus a potentially better resolution.

As can be seen from the table in the previous section, the retardation potential of the presented configuration is suited best for spectroscopy of electrons with a kinetic energy slightly above 500 eV. To give an impression of the setting for an appropriate kinetic energy, a visualization of the obtained electron trajectories in the flight tube is shown in Figure 4.3, where every panel is dedicated to monochromatic electrons of a certain energy. The starting positions are commensurate with the assumptions in the model, but not yet representative. The black areas indicate the area covered by 10 000 trajectories. The red markers indicate the positions in steps of 1 ns. Since the shown configuration is the preliminary result of our optimization process, it is found to perform satisfactorily, as can be seen from the relatively small spread of the arrival time at the detector on the order of 1 ns.

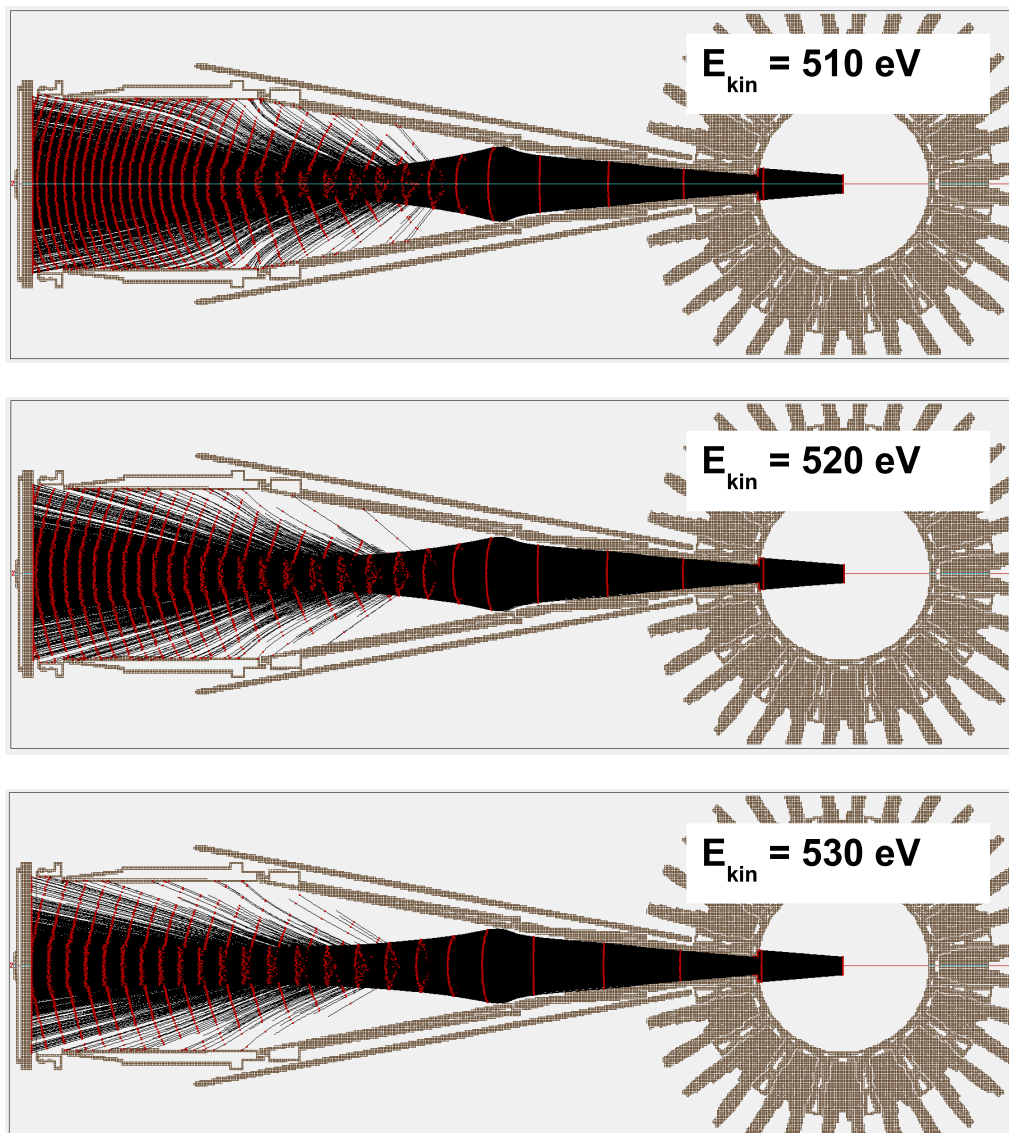


**Figure 4.3:** SIMION screen shot of electron trajectories in the flight tube potential discussed in the text for selected, relevant kinetic energies.



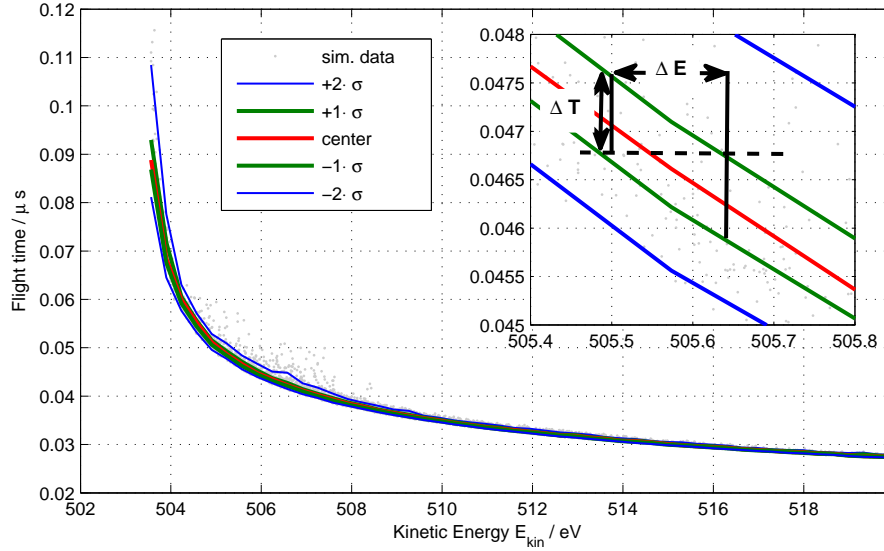


**Figure 4.4:** Flight time as a function of kinetic energy for the retardation potential discussed in the text.

In order to provide more resilient data, the simulation procedure as outlined above was applied to the shown setting. From the resulting statistical sample of detected electrons, a detailed analysis of the configuration is derived. Here, we find that significant information can already be derived from a set of as few as  $\approx 4\,500$  sample electrons, which demonstrates the high efficiency of the simulation code. At the present state of the simulation model, our representative data set is guaranteed to span the complete relevant phase space volume, but the samples do not represent exactly the same volume. Any statistical analysis, such as averaging, would therefore in principle require to apply weights according to the space represented by every point. This feature will be implemented by a future version. However, we expect only small variations here, so only small corrections of the shown data should be necessary.

The most important feature of the spectrometer, the relation between kinetic energy and flight time, is shown for the current example in Figure 4.4. Since the sample includes arbitrary combinations of deviating starting position, angle, and energy ( $500\text{ eV} \leq E_{kin} \leq 520\text{ eV}$ ), we observe a considerable, yet small, spread around the mean flight time at each energy.

The contribution to the energy resolution of the spectrometer can be derived from the width of the distribution in small energy intervals. Since we observe very asymmetric distributions (for instance, around 506 eV), we based our analysis on the quantiles as shown in the figure, which are also more tolerant towards statistical outliers.

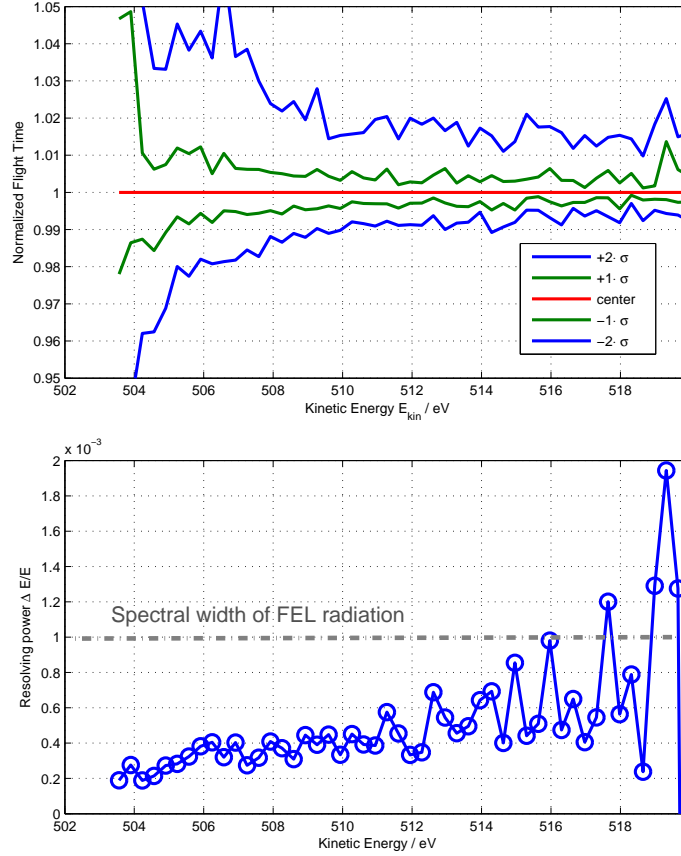


**Figure 4.5: Top:** Energy-resolved quantiles of the ToF distribution for a representative set of trajectories. The shown values were normalized to the median. **Bottom:** Resolving power for the relevant kinetic energy range as achieved with the discussed configuration.

Figure 4.5 shows the relative spread of the quantiles with respect to the median (= 50%-quantile) flight time.

We claim that two kinetic energies  $E$  and  $E + \Delta E$  can be distinguished experimentally if their representative flight time distributions are separated by the according  $\sigma$  quantiles, as shown in the inset of Figure 4.4. This criterion leads to the approximative equation

$$\frac{\Delta E}{E} = \frac{\Delta T}{\frac{\partial T}{\partial E} \cdot E} \quad (4.2)$$

for the energy-dependent resolving power of the spectrometer, which has been applied to the presented data set. For the energy range under consideration, we find a resolving power according to Figure 4.5. Common values found there are clearly better than the expected photon energy spread of SASE radiation and are already close to our goal of  $\Delta E/E = 10^{-4}$ . Note that we compare the relative spread

of kinetic energy with the relative spread of photon energy here. In the general case with a significant binding energy, the relative photon energy spread maps to a larger relative kinetic energy spread, so the requirement is relaxed.

The data set can also be used to assess the transmission properties, as is presented in Figure 4.6. The upper panel shows a histogram of the starting positions of all sample electrons in the three spatial directions. In X-direction (along the beam), we find a particularly broader distribution compared to Y and Z, where it is confined in width by the intensity distribution of the beam. In contrast to Y and Z, the relative transmission curve is cut off by the acceptance of the flight tube here. The observed width motivates the rule of thumb for the transmission, where the accepted length accords to the diameter of the entrance aperture. A slight extension of the simulation code will also allow for determining the absolute value of the transmission as a function of kinetic energy, i.e. the percentage of detected electrons with respect to the emitted photoelectrons. This will provide more precise information than the approximation given in Section 3.1.

However, we do not observe a strict cut-off here, because electrons entering the flight tube at certain angles are accepted as well. The overall distribution of accepted angles versus the flight tube-axis can be seen in the lower panel of Figure 4.6. The data has not been normalized to the respective solid angle. The majority of trajectories start at angles which are considerably smaller than half of the opening angle of the entrance aperture of  $\approx 6^\circ$ , which indicates a reduced transmission of this setup compared to the setting without any voltages applied (as approximated in Section 3.1).

As secondary requirement of a specific lens mode, the goal to achieve a homogeneous coverage of the detector was motivated in Section 3.2. The actual radial distribution of the simulation data can be found in the bottom panel of Figure 4.6. In accordance with Figure 4.3, we find a strong radial decrease of the density at the detector. This distribution is not optimal in case a high signal is to be detected, because the detector is expected to suffer from saturation in the centre, making its response non-linear. At the same time, there is much unused dynamic range at high radii. The lifetime-integral, local signal affects the ageing of the detector, so inhomogeneous wear of the detector plates can be expected.

Figure 4.3 also indicates that a high number of electrons exists that can enter the flight tube, but do not reach the detector. These electrons are suspected to contribute to a background of secondary electrons, which has to be avoided as much as possible. Unfortunately, this requirement is in direct competition with the goal to cover the detector area. Future experimental studies will have to clarify the best trade-off.

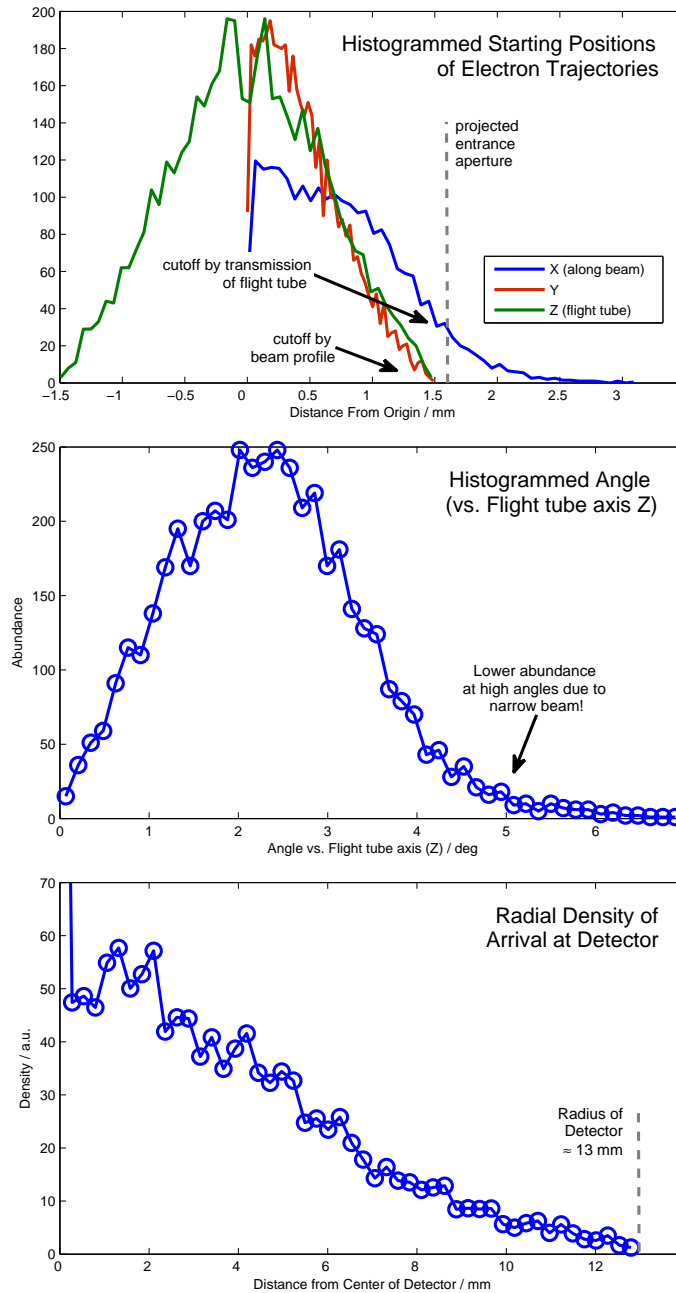


**Figure 4.6:** Transmission of the flight tube over starting position (**top**) and transmission over emission angles (**middle**). The actual distributions in X and Y are symmetric with respect to the origin. **Bottom:** Radial density of electrons on the detector.

Based on one specific example, we demonstrated the capabilities of the ToF spectrometer here. It was shown that a sufficient resolving power of the spectrometer can be achieved over a reasonably wide energy interval. Future simulations will assist in finding proper voltage settings for the complete relevant kinetic energy range. The employed simulation framework demonstrated good performance, so we are optimistic that this can be solved in a reasonable time on a desktop PC. The simulation code can in principle be employed to simulate the signal measured by the spectrometer with a level of detail. Besides a more realistic representation of the photon beam, the additional effects on spectral distribution to be included in future simulations will be natural line width and ion-induced space-charge effects.

Various applications of photoemission spectroscopy of solids have a long tradition over several generations of light sources. At modern, high-brilliance VUV facilities such as FLASH, this technique faces severe limitations arising from the high photon flux achieved there. Among other reasons, interactions between the very large amounts of emitted photoelectrons, so-called vacuum space charge effects, lead to blurred spectra with a strongly reduced energy resolution [51].

The much smaller amount of charge emitted from dilute gases, especially at a significantly higher photon energy, makes this effect insignificant in this case, even at the highest expected flux at XFEL.EU. Here, we will consider the potentials that can be made up by the ions created along the beam. We do not expect large contributions from the ions created in a single shot, since their typical axial density is found to be on the order of only  $10^7 \text{ m}^{-1}$ . Instead, we consider a potential accumulation of ions in the interaction centre of the spectrometer during a pulse train. On the one hand, a shot-by-shot accumulation of ionized gas becomes likely, since the charge can only be dissipated at the thermal velocity of the gas atoms, which in turn is on the order of some  $100 \text{ m/s}$ , which leads to only insignificant travel distances of an average atom between two photon pulses. On the other hand, the ions repel each other, so they should be accelerated out of the interaction region.

A simple semi-analytical model was created to simulate the dynamics of ions in an average field made up by their own charge. The outline of the model reads:

*“For a given distribution of charge, Laplace’s equation is solved. Classical test particles are accelerated in the resulting electric field during a small time step. The updated charge density is computed from the updated distribution of the test particles and the procedure is iterated”.*

In order to find an efficient solution, the following idealizations were applied:

- We consider an ideal gas with homogeneous pressure in a cylindrical pipe with grounded walls and a diameter of 100 mm.
- The beam is aligned axially to this tube and has a Gaussian cross section.
- The realistic pulse timing is used, but with zero pulse length.

- When created, the velocity distribution of the ions is commensurate with thermal equilibrium plus an isotropic recoil contribution from photoemission, which is also assumed to be isotropic for simplicity.
- Every ion has the same charge. This is, the broad distribution of individual charge states that is found after photoionization as an effect of multi-photon absorption or Auger cascades is neglected here and the mean charge is used instead.

The cylindrical symmetry of the setup causes the axial and azimuthal components of Poisson's equation to become trivial, and we need to solve the radial part only. The walls of the pipe act as a boundary condition here.

For a simulation of the space charge potentials we will discuss now, the following parameters were chosen:

Radius of pipe	100 mm
Photon beam $\sigma$	0.5 mm, 2 mm, 5 mm
Temperature	300 K
Axial ion density/ shot	$10^7 \text{ m}^{-1}$
Average charge per particle	4.5 e
Ion mass	83.798 u (Krypton)
Energy from recoil	0.1 eV
Probe particles per shot	100
Pulse spacing	222 ns
Time steps	10 ns

**Table 4.2:** Parameters used in the simulation of space charge effects

If known, the chosen parameters represent a possible situation at the beamlines of XFEL.EU. Various other parameters, such as the average charge of an ion, strongly depend on the properties of the photon beam. Here, we assumed multiply charged ions as a result of subsequent emission of several Auger electrons, for instance. The actual charge number is not backed with references, so all we can conclude from this showcase is that space charge might become an issue for the spectrometer, as can be seen from the results. Note that the simulation code and the theoretical background are still subject to review, so the absolute magnitude of the reported potentials, fields, etc. might still change. Therefore, we can give only a qualitative discussion here.

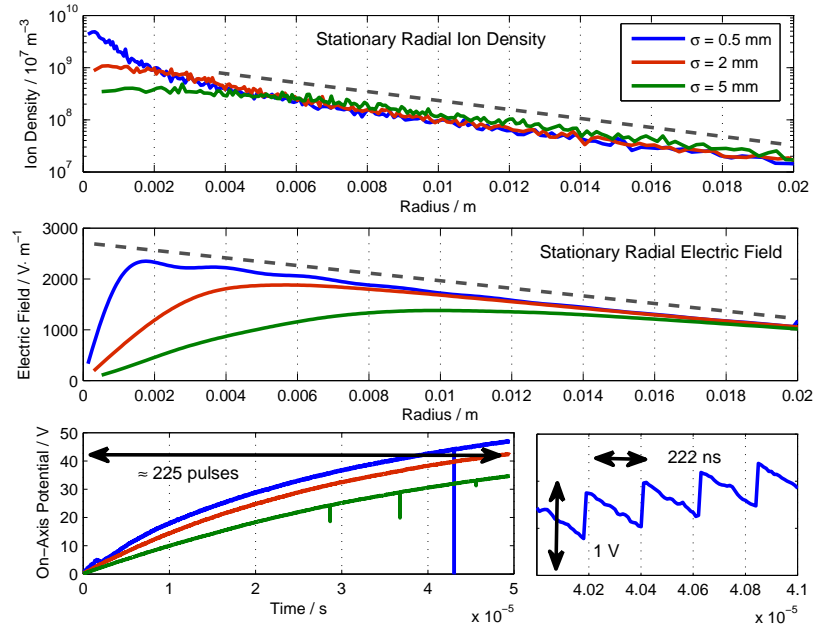


**Figure 4.7:** Near-stationary radial space charge  $5 \cdot 10^{-5}$  s after begin of pulse train.  
(PRELIMINARY DATA!)

The situation obtained for the chosen parameters after  $5 \cdot 10^{-5}$  s is shown in Figure 4.7. After this time (equivalent to roughly 225 pulses) from the beginning of a pulse train, a near-stationary state has been reached. The magnitude of the complete potential still increases with every pulse, but the relative radial field and charge density hardly change. The configuration near the beam axis turns out to depend strongly on the diameter of the photon beam, which defines the distribution of ions created at every pulse. As can be expected, the field and charge density at a certain radius  $\geq 1$  cm approach identical values. The large variations of the central ion density also has an impact on the magnitude of the space charge potential. A zoom in to the timescale between two pulses reveals the contributions from a single pulse and the decay of the potential due to charge dissipation between two pulses.

A considerable space charge potential would have a strong impact on the design of retardation potentials because photoemission lines would appear shifted, so the simultaneously observed energy interval would have to be designed sufficiently large, which is expected to affect the achievable energy resolution. Measurements of absolute photon energy can be carried out only as long as the space charge-induced potential can either be neglected or its magnitude is known. One spectrometer channel dedicated to the simultaneous observation of an Auger emission line could act as a probe of the instantaneous ion-induced potential, so the offset of the actual photon energy measurement could then be compensated.



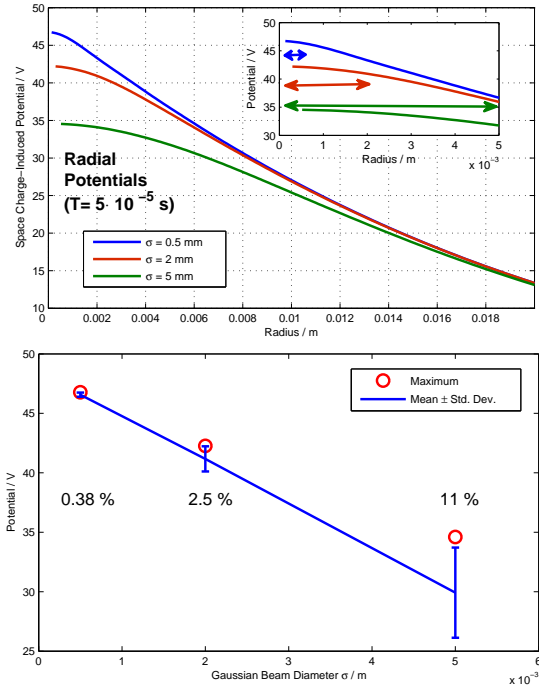


**Figure 4.8: Top:** Radial ion-induced potentials for different beam diameters.

**Bottom:** Effect of beam diameter on the variance of the potential across the active zone.

**(PRELIMINARY DATA!)**

Besides the discussed impact on absolute photon energy measurements, the energy resolution of the spectrometer could be reduced in presence of a space charge potential, as can be concluded from Figure 4.8. The left panel shows the radial potentials after  $5 \cdot 10^{-5}$  s of a pulse train. The Gaussian width of the photon beam is indicated in the inset. The potentials have a significant variation on the scale of the photon beam, especially for the widest beam. Therefore, a photoemission line under observation would appear not only shifted, but also blurred, i.e. with an increased width. For the same reasons as those for choosing a naturally narrow line for observation (Section 2.2), this has to be avoided to grant energy resolution. The right panel of Figure 4.8 gives an overview of the mean potential over the beam cross section and its RMS variation. Whether the resulting blurring of the spectrum is acceptable, still depends on the actual magnitude of the potential, as well as on the specific photon energy and photoemission line under observation. Here, this leads to the counter-intuitive conclusion that ion-induced degradation of energy resolution becomes smaller when the photon beam is narrow, even though charge densities and magnitude of the potential are higher.

The presence of a continuously growing space charge during a pulse train leads to the question of whether the accumulation of ions is dissipated completely after a

pulse train, before the next arrives. We simulated a short train with only 100 pulses and observed the decay of the axial potential afterwards. Figure 4.9 demonstrates a quick exponential decay with an initial time constant of  $3.73 \cdot 10^{-5}$  s after the last pulse has arrived. This timescale is more than sufficient to remove the potential completely before the following pulse train arrives after  $\approx 100$  ms.

In this section, we lined out a simple model of ion-induced space charge which we employed to estimate the on-axis potential that can occur during a pulse train, even though we have to stress again that the presented results are preliminary. We discussed the consequences of significant space charge potentials and showed possible solutions.

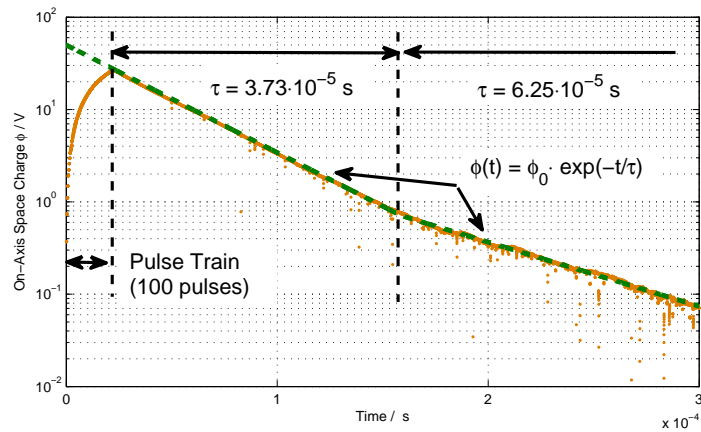


**Figure 4.9:** Decay of the on-axis space charge potential after a truncated pulse train.  
(PRELIMINARY DATA!)

## 4.3 Simulation of data reduction

We will now focus on the performance of the routine that was proposed for data reduction in Section 3.9.3.2. This method is intended for time-critical processing of the raw data obtained from the digitizers and will be the key feature of the data acquisition system that grants technical feasibility of real-time processing, mainly because it allows to source time-consuming processing steps out to a microprocessor and has only low requirements for FPGA processing.

Here, we give a first impression of the way the routine works by processing artificial data. The essential question to be answered in this field is how well the spectral information is transmitted through the routine, i.e. how well the features of the reconstructed spectra represent the “true”, physical spectrum concerning width, peak position, etc.

We consider a set of Gaussian spectra with certain variations of peak position and peak width. These two properties will essentially be evaluated in the future for an assessment of the spectral properties of the photon beam. Artificial data in the time-of-flight domain was created using a superposition of the model MCP pulse as seen in Figure 3.8. We assume a reasonable total number of 500 detected photoelectrons per shot here. Figure 4.10 shows five realizations of a single-shot spectrum from an identical Gaussian shape, which gives an impression of the statistical noise in the data. Note that such a single-shot spectrum contains much too high statistical noise to be evaluated properly.

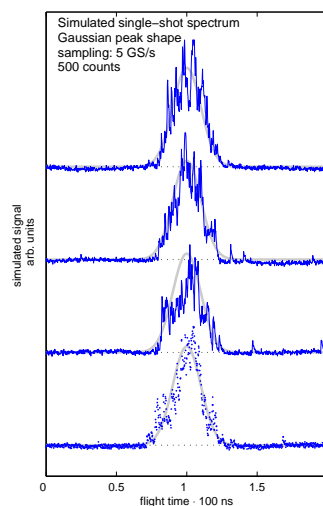


**Figure 4.10:** Artificial, single-shot ToF spectrum as expected at low count rates of 500/shot.

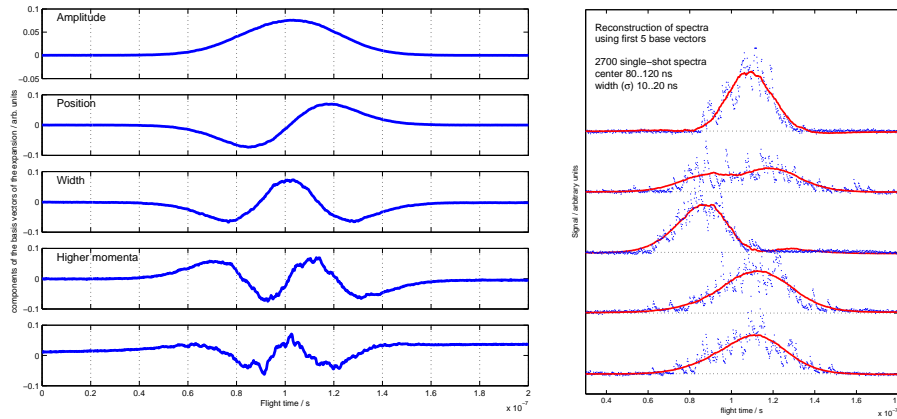


**Figure 4.11:** Showcase data for the data reduction algorithm (artificial data as in Figure 3.8 including random variations position and width ).

**Left:** First vectors of the basis as determined by the data reduction algorithm.

**Right:** Selection of artificial spectra (blue) and reconstruction as obtained from reduced data (red).

Following this procedure, we created artificial spectra of a complete pulse train and included random modifications of peak position and width to simulate statistical fluctuations of the photon beam. This data was fed into the data reduction algorithm as introduced in Section 3.9.3.2. The first five base vectors (Figure 4.11) determined here were used for the reconstruction of the data. The right panel in Figure 4.11 shows a comparison between the artificial raw data (blue) and the reconstructed spectrum (red) for five randomly selected cases of the complete train.

We find an excellent agreement between the momenta of the raw data and the reconstruction. Therefore, we conclude that the method is capable of reproducing the essential spectral properties, and that any results of evaluation of the reduced data can be assumed to represent the original data. To what extent this is true, will have to be figured out by a closer statistical analysis, i.e. by applying a  $\chi^2$ -test. For this demonstration, we claim that the method is appropriate compared to the statistical quality of the raw data.

Besides a good reproduction of the raw data, we find the excellent separation of the signal from statistical noise discussed before (Section 3.9.3.2). This has the outrageous side effect that no further smoothing procedures or similar need to be applied for a conventional spectral analysis. The attentive reader will most likely realize a certain discrepancy between the input and the output of the algorithm, since, in contradiction to the input, the results shown in Figure 4.11 obviously include non-Gaussian components. A closer examination of the raw data shows that those

non-Gaussian features are included in the artificial data as well and therefore cannot be an artefact of processing. Instead, they are a result of the statistical uncertainty of the single-pulse data. Obviously, the reconstructed spectra cannot become better than the data they rely on.

We considered a case, which we assume not be too far from a realistic situation at XFEL.EU. In this section, we focused on the question of the validity of conclusions drawn from reconstructed data. We can give only a first impression here, but the results make us optimistic to gain crucial spectral information from this procedure. The high potential this method has for handling the tough requirements for pulse-to-pulse spectroscopy at XFEL.EU lets us strongly recommend this technique for future use.

Even though the polarization of light produced in an undulator necessarily has a linear polarization, some proposals [63–67] have been made how the technical layout of the photon beamlines at XFEL.EU can be extended to produce light with variable polarization. In the best case, full control of the polarization is achieved, i.e. an arbitrary orientation of the polarization vector and arbitrary mixtures of linear and circular polarized light can be selected. The physics of radiative emission by a charged particle in an undulator always results a certain polarization, so unpolarized light cannot be produced by an ideal undulator. The current discussions on a controlled manipulation of the polarization of the photon beam also calls for an option to probe polarization by a diagnostics device. This potentially also includes the demand for single-pulse resolved information, because fast switching options or statistical fluctuations (in part of the proposed schemes) might also cause variations at this temporal level.

As introduced in Section 2.1, photoemission from rare gases is well-suited to probe the orientation of linear polarized light. The respective equations can easily be extended by a term for isotropic emission to include the effect of emission by circular polarized or unpolarized light. An evaluation of the angular resolved emission intensity can then be used to determine not only the direction, but also the linear polarized content of the photon beam. The general demand is to determine the degree of circular polarization, but since any potential technical implementation of polarization modification always affects the relative weight of linear versus circular polarization (and in theory, no unpolarized radiation is produced at all), determining the degree of linear polarization provides a suitable, though indirect, measure of circular polarization.

Using photoionization, circular polarization can be measured directly only by detecting coincident emission of photoelectrons under different angles. From a technical point of view, this requires the detection of at most one electron per pulse and analyser channel, which is obviously not sufficient to obtain spectroscopic information at the same time. In this section, we will present the physical background and a suggested technical implementation for the diagnostics of polarization. A study of the expected performance based on artificial data will be discussed.

The requirements and specifications of the photoelectron spectrometer with respect to polarization analysis can be summarized as follows:

■ **Degree of linear polarization**

The angular-dependent emission signal can be expected to be a superposition of isotropic and dipole components. 1% has been defined as the minimum specification.

■ **Direction of linear polarization**

Depending on the actual method of modifying the polarization, the orientation of the linearly polarized part could be changed. This can, for instance, be achieved when using an undulator of APPLE-type. Measurements of this quantity are expected to be determined within a 1°-accuracy.

■ **Work on reduced data**

Data reduction can in general only be employed efficiently only when the used data evaluation techniques can work on reduced data, as described in Section 3.9.3.

■ **FPGA-compliant algorithm**

Even though not mandatory, the demand for short response time of the system translates to an implementation on an FPGA board (see Section 3.9.5).

■ **Statistical stability**

Statistical uncertainty of the results concerns polarization analysis on the same level as spectroscopy. In general, any proposed method must be capable of providing precise, statistically stable results with the same signal levels as considered for spectroscopic applications in Section 4.1.

We provide a rough outline of the proposed method here. For brevity, we omit some prefactors. The precise model will be published elsewhere. In case part of the photon beam is linearly polarized and has an unpolarized or circularly polarized content, the angular dependence of the photoemission signal can be derived from Figure 2.1 including an isotropic term.

$$I(\phi) = \frac{\sigma}{4\pi} \left( I_0 \left( 1 + \frac{\beta}{2} (3 \cos^2 \phi - 1) \right) + I_u \right) \quad (4.3)$$

For  $\beta > 0$ , the expressions for the minimum and maximum intensity read as follows. The prefactor  $\sigma/4\pi$  has been omitted here for brevity. Note that it would cancel in the final result (Equation 4.10) in any case.

$$I_{max} = I(\phi = 0) = (1 + \beta) \cdot I_0 + I_u, \quad (4.4)$$

$$I_{min} = I(\phi = \frac{\pi}{2}) = \left(1 - \frac{\beta}{2}\right) \cdot I_0 + I_u. \quad (4.5)$$

In order to relate this to experimental data, equivalents of  $I_{max}$  and  $I_{min}$  could easily be determined from a hypothetical measurement of angular-dependent intensity. But since the average number of detected photo-electrons in an individual channel may be as low as 100 per shot, the statistical error of  $I_{max}$  and  $I_{min}$  due to Poissonian noise would be unacceptable high.

#### 4.4.1 Degree of linear polarization

A statistical more robust way of finding these quantities is to express them in terms of mean value and standard deviation. For a sinusoidal modulation with unit amplitude, the standard deviation is

$$\langle (\cos \phi - \langle \cos \phi \rangle)^2 \rangle = \sqrt{2}. \quad (4.6)$$

This value holds in case of continuous angles. In the actual design of the spectrometer, the intensity can only be probed at discrete angles, which in consequence requires a slight modification of this value. For the moment, this can be considered to provide a sufficiently good approximation. Using Equation 4.6, the maximum and minimum values of the experimental data can be written as

$$I_{max} = \langle I \rangle + \sqrt{2} \langle (I - \langle I \rangle)^2 \rangle, \quad (4.7)$$

$$I_{min} = \langle I \rangle - \sqrt{2} \langle (I - \langle I \rangle)^2 \rangle. \quad (4.8)$$

Combining Equations (4.3), (4.3), (4.6) and (4.6), and resolving for  $I_0$  and  $I_u$ , results:

$$\begin{pmatrix} I_0 \\ I_u \end{pmatrix} = \begin{bmatrix} 1 + \beta & 1 \\ 1 - \frac{\beta}{2} & 1 \end{bmatrix}^{-1} \cdot \begin{pmatrix} \langle I \rangle + \sqrt{2} \langle (I - \langle I \rangle)^2 \rangle \\ \langle I \rangle - \sqrt{2} \langle (I - \langle I \rangle)^2 \rangle \end{pmatrix} \quad (4.9)$$

The degree of linear polarization  $\zeta$  is hence determined by

$$\zeta = \frac{I_0}{I_0 + I_u}. \quad (4.10)$$



### 4.4.2 Direction of linear polarization

We now focus on the determination of the direction of polarization. With respect to some arbitrary, but fixed reference angle, the direction has to be introduced to Equation 4.3 by a phase factor  $\Delta$  in the argument of the sine-function. Using Equations (4.6) and (4.6), the experimental data  $I(\phi)$  can be normalized to a sinusoidal function using information from the experimental data only:

$$\tilde{I}(\phi) = \frac{I - \langle I \rangle}{\sqrt{2} \langle (I - \langle I \rangle)^2 \rangle} = \sin(2\phi + \Delta) \quad (4.11)$$

$\tilde{I}$  obviously has an average of zero and unit amplitude, so the only unknown quantity remaining is  $\Delta$ , which has to be determined from the experimental data. Therefore, the expression below is evaluated and solved for  $\Delta$ :

$$\begin{aligned} \int_0^{2\pi} \sin(\phi) \cdot \tilde{I}(\phi) d\phi &= \int_0^{2\pi} \sin(\phi) \cdot \sin(\phi + \Delta) d\phi \\ \Rightarrow \Delta &= \cos^{-1} \left\{ -\frac{1}{\pi} \int_0^{2\pi} \sin(\phi) \cdot \tilde{I}(\phi) d\phi \right\} \end{aligned} \quad (4.12)$$

Every analyser channel provides a probe of  $\tilde{I}$  at equidistant angles  $\phi_j$ . Neglecting the fact that an analyser provides the weighted average of the angle-dependent intensity over its solid angle of acceptance by using

$$\int_0^{2\pi} \sin(\phi) \cdot \tilde{I}(\phi) d\phi \approx \frac{2\pi}{N} \sum_{j=1}^N \sin(\phi_j) \cdot \tilde{I}(\phi_j), \quad (4.13)$$

where  $N$  is the number of analysers (here:  $N = 16$ ), we can rewrite Equation 4.11 as

$$\Delta = \cos^{-1} \left\{ -\frac{1}{\pi} \sum_j \sin(\phi_j) \cdot \tilde{I}(\phi_j) \right\}. \quad (4.14)$$

which provides a measure of the orientation of linear polarization that depends only on measured intensities. Because it includes all available data, i.e. every analyser, a certain statistical robustness of the determined angle can be expected. Here, we derived statistical estimators of the degree and the direction of linear polarization, which are given by explicit equations. With regard to a future implementation on an FPGA architecture (see Section 3.9) for low latency, single-pulse processing, such a representation is mandatory. Especially the application of an iterative algorithm, e.g. least-squares minimization as used in curve fitting, is very detrimental for various reasons and should therefore be avoided by any means.

### 4.4.3 Performance with artificial data

The following feasibility study is dedicated to an assessment of the performance of the proposed techniques in presence of statistical uncertainties of the measured intensities in each channel. The question to be addressed here is not only the statistical uncertainty of the determined values of direction and degree of linear polarization, but also if mean values are represented correctly, i.e. without a noteworthy bias, by the method.

We assumed intensity distributions according to Equation 4.3 with certain nominal intensities  $I_0$  and  $I_u$ , as well as a given direction of linear polarization. Every individual analyser channel was assumed to provide a signal including independent Poissonian noise, which was used as input to Equations (4.10) and (4.14) in order to perform the polarization analysis.

For a specific setting, multiple random realizations were computed, so the mean value and standard deviation of the degree and direction of linear polarization can be estimated. Figure 4.12 shows the results of the analysis for a variable intensity of the linear-polarized part. A fixed ratio  $I_0/I_u = 2$  was assumed throughout this case study. The upper panel shows the effect on the determined polarization angle for nominal directions  $0^\circ$ ,  $15^\circ$ , ...,  $90^\circ$ . It can easily be seen that the determined angle approaches the nominal angle for high intensities, i.e. when relative uncertainties in the signals become small. At low signal levels, we observe a small systematic deviation from the nominal angles, especially for  $0^\circ$  and  $90^\circ$ , of a few degrees. However, in the experimentally relevant range above 100 counts per channel (i.e. detected electrons per pulse), this bias is negligible. Note that problems at certain angles could always be avoided because the choice of the reference is free. From the standard deviations found in the figure, it can be concluded that at least a few hundred counts per channel are necessary in order to determine the polarization angle within the specified statistical uncertainty of  $1^\circ$ .

The second feature to be extracted from the angle-resolved data is the degree of linear polarization. The results for artificial data with polarization degrees of 0.33, 0.5, 0.67, 0.8 and 0.91, are shown in the bottom panel of Figure 4.12. For signal intensities we consider realistic for spectroscopy (i.e. 100 – 1 000 counts, compare Section 4.3), we find statistical fluctuations  $\leq 0.03$  of the degree with a tendency towards smaller values at higher signal strength. This result makes us confident to provide this value within the demanded precision at least as an average value of 10 – 100 pulses. Again, systematic deviations become important only for a very low signal level and have a tendency to overestimate the degree of linear polarization.

The angular dependency of the artificial data was created assuming an anisotropy parameter of  $\beta = 2$ . In order to assess the performance for the general case, the polarization analysis was done for a given artificial signal as a function of  $\beta$ . The results are shown in Figure 4.13. The general, trivial finding is that the relevant features of the polarization can be determined better the higher the anisotropy of emission is ( $\beta \rightarrow 2$ ), which can be seen here by the statistical uncertainties. Potential difficulties, again, arise from the systematic deviations of the estimated values from the nominal values for low anisotropy ( $\beta < 0.5$ ). According to the reference values in Figure A.3, these cases have no practical relevance. For realistic cases, the general applicability of the suggested method is not affected by the actual value of  $\beta$ .

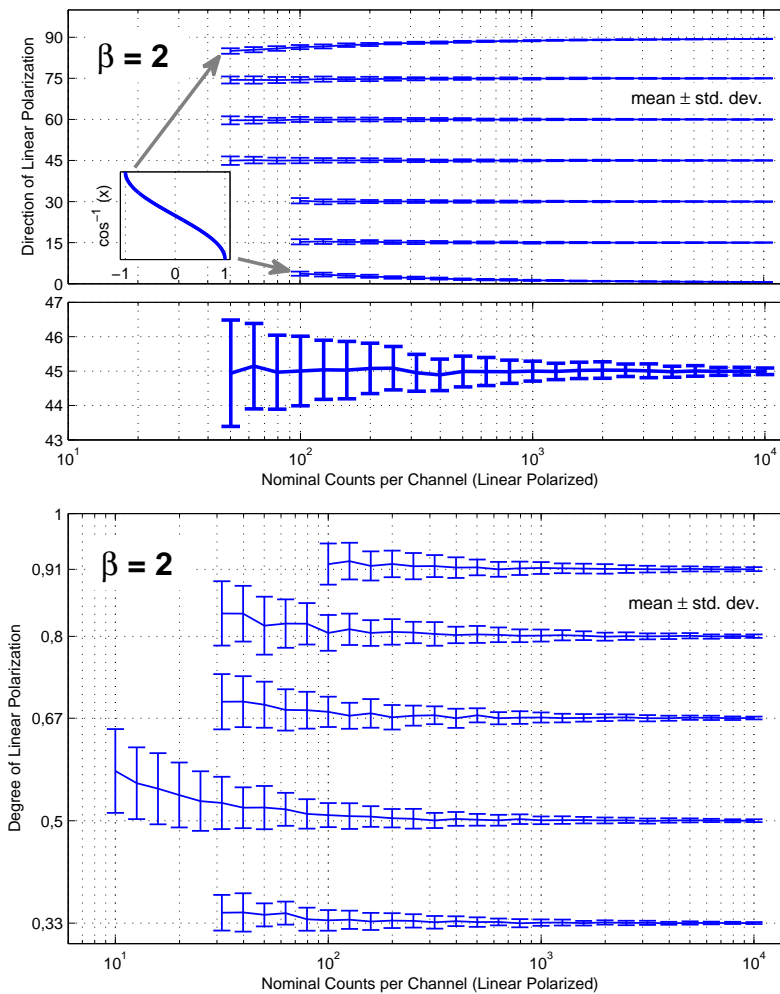


**Figure 4.12:** Statistical uncertainty of the direction and the degree of linear polarization as determined from artificial data. **Top:** Direction of polarization vector as a function of detected electrons per analyser. **Bottom:** Degree of linear polarization as a function of detected electrons per analyser.

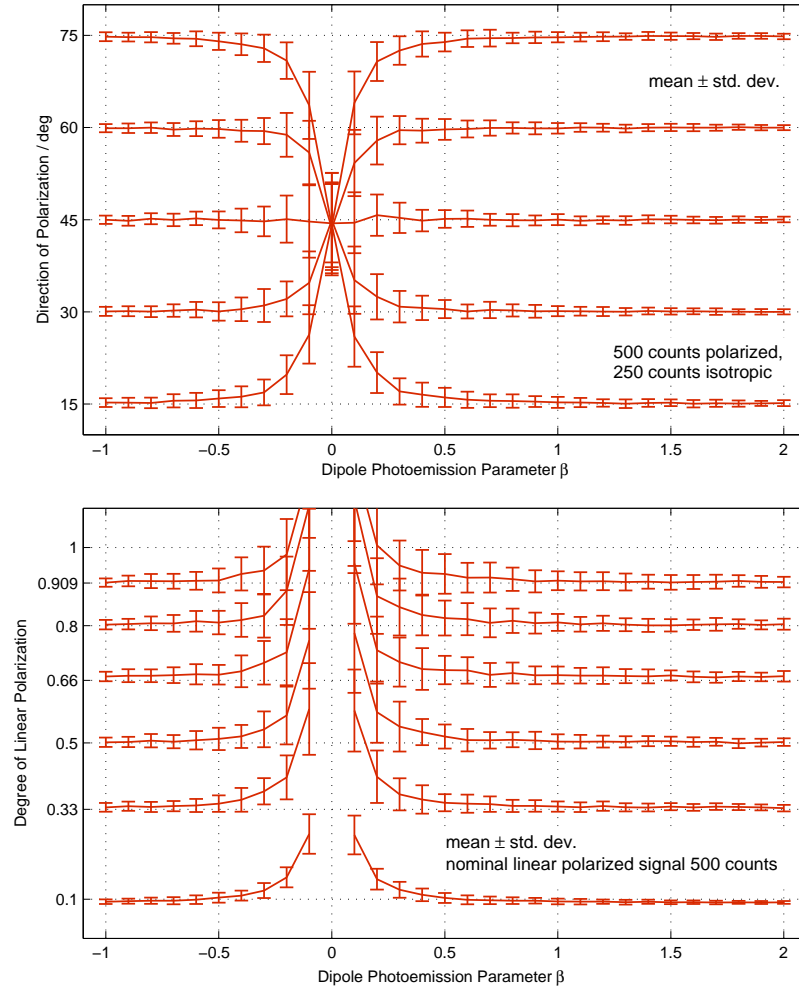


**Figure 4.13:** A value of the anisotropy parameter  $\beta \geq 0.5$  is sufficient to achieve a reasonable statistical confidence of the degree and direction of the polarization vector. **Top:** “Measured” direction of linear polarization as a function of  $\beta$ . **Bottom:** “Measured” direction of linear polarization as a function of  $\beta$ .

#### 4.4.4 Discussion

We presented study using artificial data demonstrates that the parameters of linear polarization can be determined from the angular resolved photoemission signal in the presence of statistical noise. The uncertainties determined here show that, for reasonable signal levels, the specified precision appears in range. The implementation of the suggested method is based on the evaluation of explicit formulas, so an FPGA implementation with sufficient throughput and low latency as needed for single-shot analysis is possible. Note that in case of low signal levels, the signal might optionally also be accumulated over several photon pulses to provide average values with lower uncertainty.

Here, we assumed Poissonian noise in the signal of every individual analyser. According to the requirements for high-level data evaluation (Section 3.9.4), polarization analysis would be done using reduced data. Obtaining the required single-channel intensities from the reduced representation is trivial. A well-known fact is that statistical noise is removed efficiently from the reduced data, so even smaller statistical errors of the results than presented here can be expected in that case. In the future, dedicated start-to-end simulations of the data evaluation chain can provide more realistic information. For practical applications, the origin of the systematic deviations as seen in the simulations has still to be figured out. The asymmetry of the Poisson distribution is suspected to lead to the observed artifacts in the estimated values, especially at low signal levels. During operation as a diagnostics device, it might be subject to correction by calibration data.

In conclusion, the characterization of the degree and the direction of linear polarization of the photon beam can in general be determined using the method we introduced here. In a study on the effect of statistical noise in individual analyser channels, we demonstrated that the specified values for the precision are most likely limited by counting statistics, but can nearly be reached. The technical implementation we foresee for the method complies with any other requirements discussed in the beginning of this section.

---

# 5 Safety implications

In this chapter, we will give a first analysis of safety issues of the complete setup that need to be solved. They can roughly be divided into measures that guarantee the safety of humans operating the devices and those preventing damage from the hardware.

---

## 5.1 Human safety

### 5.1.1 High Voltage

The high voltage applied to the flight tubes and detectors can have a magnitude on the order of 10 kV, so it is potentially lethal. The voltage will be delivered from the supply to the spectrometer using suitable cabling and SHV connectors, so the high voltage can never be touched in the mounted state. Further protection against unauthorized or accidental unmounting of the plugs when under high voltage will have to be discussed. Damaged or broken cables should be detected by the voltage supply. Considerably lower voltages of a few hundred volts occur at the interface between the MPod crate (ISeg/Wiener) and the attached modules, so it has to be ensured that empty slots in the crate are covered well before operation. Moreover, the design of the vacuum chamber and the frame must ensure well-defined grounding.

### 5.1.2 Gas supplies

Another potential danger arises from the presence of compressed gases in the confined space of the photon tunnel. Failure of pipings, or even gas containers, can potentially release a large amount of gas instantaneously, which might lead to a critical depletion of oxygen in the tunnel air. Early estimations showed that even the content of a complete, 50 ℓ, 200 bar gas bottle (i.e. 10 m<sup>3</sup>) cannot cause this situation because the tunnel ventilation will quickly dilute the released gas. We intend to use only non-toxic rare gases, so other effects on human health are not expected. In any case, the continuous tunnel ventilation provides sufficient flow to dilute the gas quickly. Since all personnel will have to leave the tunnel before operation, the actual necessity for special safety measures has still to be figured out.

---

## 5.2 Machine protection system

Safety measures for the protection of the hardware can basically be separated into those that are already implemented in the technical layout of the system (“built-in protection”), and those that are applied during operation, so they need interaction with the machine controls (“protection by procedures”). The passive measures mainly aim at preventing radiation damage of electronics. Here, the design has to assure that the time to absorb a fatal dose under regular operation becomes as large as possible. This concerns especially electronics mounted close to the beam pipe, where the highest radiation levels over the tunnel cross section are expected.

Among the critical components are:

- Turbo pump controllers attached directly to the pump housing
- Residual gas analysers
- Active pressure gauges
- Preamplifiers, which are necessarily located near the detectors

As a rule of thumb, electronic devices become more sensitive to radiation damage as the structure size of the circuitry decreases, but the actual lethal dose has to be determined for every individual device. Since only commercial products are to be used here, no alternatives exist, and tolerable radiation doses are rarely known. The feasibility of shielding individual devices to a great extent depends on the photon energy distribution of the background. Only first estimations of expected radiation background have been given to date, so it is not possible to decide if doses might become critical.

Where possible, any electronic circuitry should be removed as far as possible from the beam pipe. If necessary, general electronics will be placed in shielded racks, so hardware solutions that allow for separating a device and its control electronics by a cable of several meters length should be preferred in general. Especially the choice of active pressure gauges will have to be reviewed when more reliable data is available.

During operation, the systems state will have to be observed continuously in order to detect failures of critical components and to trigger appropriate reactions, which is an inevitable feature of the intended high level of automation. Because of the rather high complexity of the spectrometer and its subsystems, various scenarios

for system failures have to be considered. Some of them affect only the internal state of diagnostics, but others may become a serious threat to the safety of other components in the beamline. Furthermore, errors occurring at remote locations might affect the state of the diagnostics station, so they must be handled locally. For our case, we can figure out three main topics with safety relevance, as outlined below.

## 5.2.1 Vacuum

### ■ Failure of turbo pumps

A turbo pump not running at its nominal speed is a potential leak and must be handled accordingly, e.g. by fast shutters. Gate valves should be foreseen along the beamline to isolate the affected section.

### ■ Valve failure at gas dosing system

The loss of control over the gas flux entering the vacuum chamber will definitely cause a severe problem, so the maximum flux into the chamber must be limited mechanically.

### ■ Catastrophic failure of vacuum components

For instance, the moving stage of the spectrometer requires flexible bellows, which may become leaky under excessive deformation or after long operation.

## 5.2.2 Beam protection

### ■ Uncontrolled or undefined position of the shifting unit

The relatively small aperture (29.5 mm) of the spectrometer, in combination with the large transverse travel range (up to 10 cm) of the photon beam, potentially leads to dumping of the beam at the spectrometer, resulting in a very large instantaneous radiation dose in the environment with a potentially fatal permanent damage to instrumentation.

### ■ Undefined mirror configuration with beam

When detected externally, this case possibly has to be handled locally.

### ■ Excessive beam drift

Due to the high photon flux, even the absorption of the beam's halo near the spectrometer can cause an excessive photoemission signal that might deal damage to the highly sensitive detectors.



### 5.2.3 Software

Critical parts of the spectrometer are controlled by software, partially within feedback loops. Therefore, software malfunction should be treated with the same priority as faults of the attached hardware.

- **Shifting Unit**

Undefined movement and states with an unknown position of the unit definitely have to be prevented .

- **Gas insertion**

A crashed or non-responsive feedback loop might leave the gas inlet in an undefined state.

We will now discuss two possible scenarios requiring error handling, that we assume to be the most relevant. Here, we face the problem of error handling from the point of view of a routine, which has to decide on appropriate measures. These two showcases will be used to derive mandatory features of a safety system. The suggestions made here might be beyond the scope of the machine protection system (MPS), but at least a subset of the required functionality will be possible to solve on that level. We cannot give a detailed layout of our future systems here, since it strongly depends on the later design of the MPS.

Critical situation

## High or unknown pressure in vacuum chamber

### Possible reasons

- **Gauge switched off**  
temporarily high pressure
- **Gauge broken**  
(filament,...)
- **Turbo pump failed**  
excessive gas load
- **Dosing valve malfunction**
- **Software crashed**  
or non-responsive
- **Leak in chamber**

### Reactions

#### In order of severity

- Issue warning
- Close gas dosing system
- Shutdown detectors
- Shutdown gate valves  
to beam line,  
trigger error to MPS

#### Context specific

- Check status of local  
pumps and valves
- Restart turbo
- Restart gauge
- Kill application, restart

Critical situation

## Shifting unit in bad or unknown position

### Possible reasons

- **Encoder failed**
- **Motors failed**
- **Communication failed**
- **Software crashed**  
or non-responsive
- **Unexpected behavior**  
of beamline control system
- **Beam drifting**

### Reactions

#### In order of severity

- Issue warning
- Dump beam

#### OR

- Prevent beamshutter  
from opening

#### Context specific

- Readjust position  
(move to reference)
- Reset motors and encoders
- Restart software,  
reset communication

An analysis of the details assessed of the two examples in Section 5.2.3 leads to the following conclusions:

- **Need for software implementation**

Unlike the first approach of a hardware-only solution for the beam protection system, the complexity of some error handling routines requires a software implementation. The need to access a variety of devices on the PLC subsystem encourages the decision for software as well.

- **Need to access diagnostics**

Especially other photon beam diagnostics might have to be accessed to monitor certain states of XFEL.EU. Since these usually involve software for data acquisition and processing, the advantage of an implementation purely in hardware does not apply then.

- **Treat exceptional situations locally and globally**

Local non-critical, exceptional cases, such as a moderate increase of gas pressure, can be handled locally and do not affect the rest of the machine. More critical states will require to communicate an error to the outside world, for example in order to shut down injection. Incoming error events triggered somewhere else might require local actions in order to protect the spectrometer.

- **Specification of critical state**

The specific situation that caused an error and the origin of the error message must be recognizable by, e.g. "error codes".

- **Rating of severity**

Different levels of severity must be distinguishable (e.g. "warning", "error", "fatal error"), so the appropriate action can be executed.

- **Hardware connection**

Since at least part of the BPS will run on hardware, a bidirectional interface to software controls must be established.

- **Reliability of software modules**

The implementation of safety-relevant functionality in software raises new problems, which must be handled. Our suggestion is to put every critical software module under surveillance of a watchdog process, which has the authority to shut down and restart non-responsive applications. Redundant execution of the same process (on different machines) should also be considered.

- **Access priority to actuators**

Actuators, such as valves and motors, are commonly used by some piece of control software, whose operation might interfere with the actions performed by a safety routine. Therefore, access priorities to hardware components that are not read-only (gauges, etc.), must be implemented on a low level.

- **Relation to regular control software**

The general software architecture of the control system should allow for the coexistence of “control” software for regular operation and “safety routines” for exceptional cases. The relation between implementations from both fields must be clarified.

- **Inhibition of illegal operations**

The preceding points mainly unexpected events. The contrary case is that an action performed by an automated routine or a user might result an undefined or critical state of the machine, e.g. by opening a valve as long as the pressure is not known on both sides and inside a reasonable range. These “illegal” operations have to caught by an intermediate layer between control applications and drivers.

---

## 6 Interfaces to other work packages

A successful implementation of the ToF spectrometer also depends on how it fits into the context of the machine. Various issues demand for a good collaboration with the neighbouring work packages. Interfacing between work packages has been mentioned wherever applicable throughout this document, and we give only a brief summary here. More details can be found in the referenced passages.

---

### 6.1 DAQ and Control (WP-76)

As was outlined in Chapter 3 on the general layout of the system, the spectrometer can only be operated efficiently under massive use of automation, networking, and computing. All these issues fall under the responsibility of WP-76.

- **Connectivity (Section 3.9.2)**

DAQ group defines the networking infrastructure in the photon tunnels for readout and remote control of diagnostics. Based on a worst-case estimation of the data transport rate, the total dedicated bandwidth for the spectrometer could be defined.

- **Machine status information (Section 3.10)**

The status of the machine is an inevitable input for diagnostics, since actual settings for a specific situation have to be made. We assume that status inquiries, especially of the accelerator and the undulators will be implemented on the basis of the global control network.

- **Use of databases (Section 3.10)**

Operation of the spectrometer will heavily rely on calibration data, especially for settings of the flight tube, so some database infrastructure will be required to store and recall such data upon request.

- **Use of archive system (Section 3.10)**

Diagnostics will provide essential information, which defines the context of experimental data from the end stations. Therefore, it has to be stored in a central run archive to grant later access by users.

■ **Low-level data processing (Section 3.9.3)**

The high data rate acquired by the spectrometer requires sophisticated methods of data reduction. Moreover, data processing is time critical. Both motivates an FPGA-based implementation. WP-76 defines the hardware components and architecture in this field and will provide expertise for the realization of FPGA-based computing.

■ **Timing**

The spectrometer requires an input trigger signal as a time reference. WP-76 will define the hardware architecture to be applied here. As currently foreseen, a user front end for timing on the basis of the  $\mu$ TCA crate specifications will be provided, which is also the standard for digitizers and FPGA processing.

■ **Software architecture (Section 3.10 and Chapter 5)**

The software architecture of the photon beam systems at XFEL.EU is to be defined by WP-76. Diagnostics-related software applications have to fit into this framework. Furthermore, global concepts for specific tasks such as operational safety have to be developed on the level of general software architecture. The upcoming initiative for an MPS including more work packages from the photon beam section will be a first steps towards architectural design. Software interfaces to the global software system are expected in the near future.

■ **Software engineering (Section 3.10)**

The spectrometer requires modular software controls for every subsystem, as well as controls for the complete system. Every subsystems is intended to provide graphical user interfaces as well as software interfaces. Vital support in software development will be given by WP-76.

■ **Standards (Section 3.10)**

The choice of electronic components is currently based on an approval by WP-76, who also promise their support in case of a positive decision.

---

## 6.2 X-Ray Optics and Transport (WP-73)

### ■ Definition of location (Section 3.7)

The location where the spectrometer will be installed defines vital boundary conditions for its expected performance and use case. Potential locations depend to a great extent on the overall layout of the beamlines, which have to be discussed in close collaboration with WP-73.

### ■ Vacuum compatibility (Section 3.5)

The vacuum conditions under operation of the spectrometer have to be harmonized with the requirements of the vacuum system at the beamline. This especially concerns the specifications of the differential pumping stages upstream and downstream the spectrometer section. Vital developments by WP-73 will contribute to solve this issue.

### ■ Beam protection system (Chapter 5)

The spectrometer has to be integrated into the global beam protection system, because it could potentially cause failures with an impact on the complete system. An upcoming inter-work group initiative involving, among others, WP-73 and WP-74, will deal with topics arising from safety considerations.

### ■ Standards (Section 3.5)

Our goal is to keep the set of vacuum components deployed in the beamlines as small as possible. As a heavy user of vacuum technology, WP-73 can provide valuable input for the definition of standards in this field.

### ■ Beamline status information (Section 3.10)

The exchange of status information between the beamline and the diagnostics stations in general is expected to happen on a basis of the beamline control systems, so a rather indirect interface exists here.

---

## 6.3 Detector design (WP-75)

- The diagnostics-based creation of VETO signals can significantly enhance the overall efficiency of detectors at the experiment end stations, because it would allow for an early selection of single-shot data. As outlined in Section 3.9.5, the ToF spectrometer has a high potential to contribute information to a VETO system. Our current understanding is that VETO signals will be handled on a very low hardware level, so a potential future interface with detector group is expected.

---

## 6.4 Machine status information (Section 3.10)

- The spectrometer can only work efficiently if its settings are aligned with the current status of the machine, so input from this field is an essential requirement, which we expect to solve by interfacing the machine via the beamline control system.

---

## 6.5 Accelerator control

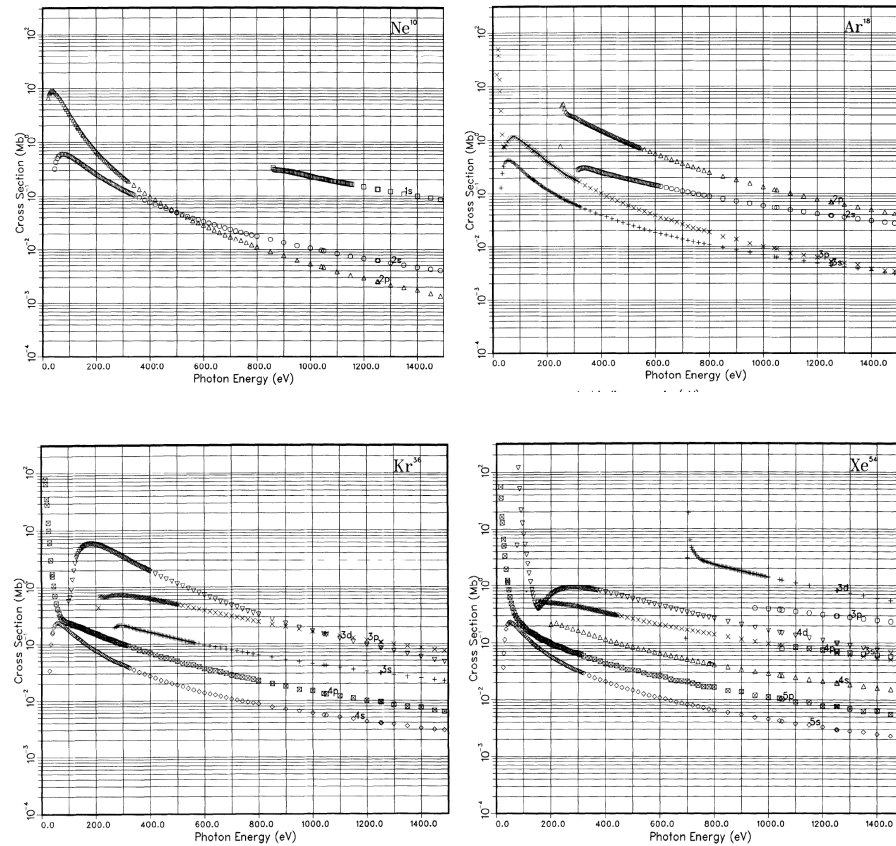
- As an interesting future option, photon diagnostics has been considered as source of feedback information for the accelerator systems. Due to the fact that we expect a comparatively low latency of the local flow of information, feedback data could potentially be provided intra-pulse train. Possible applications of such a feature will be discussed in the future.

More interfaces to other work packages in the framework of the European XFEL project are indirect, since it basically means to exchange diagnostics information. At the current stage of the project, we assume that this can be done within the DAQ and control network, which is under development in WP-76, and that there will be no reason to bypass this system.

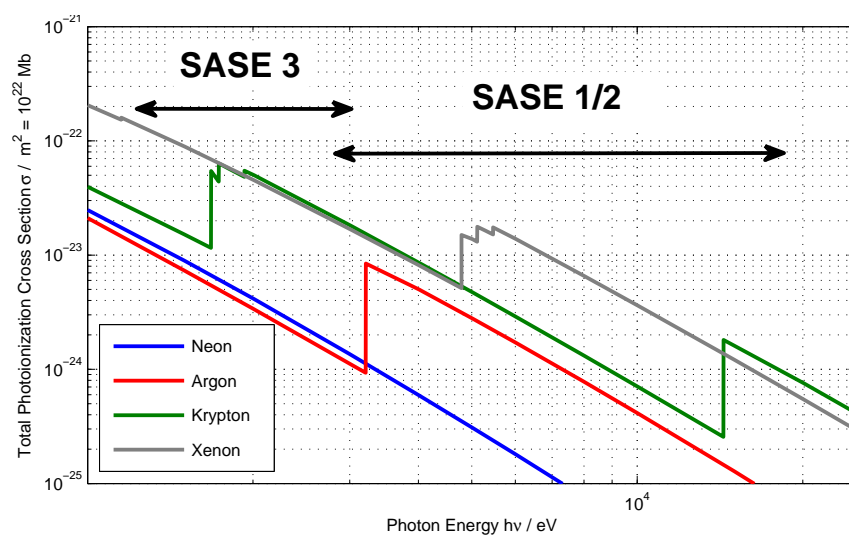




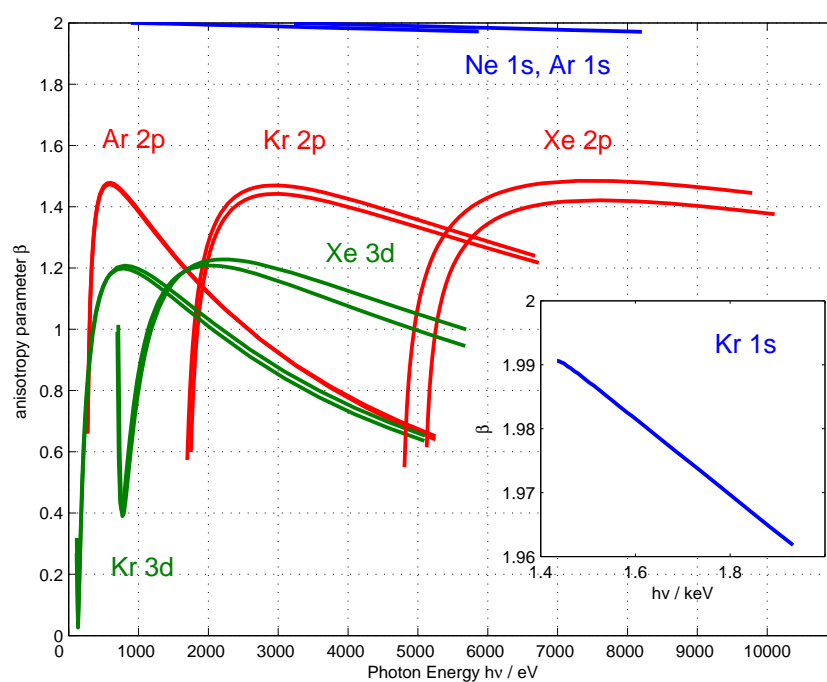
# A Physical reference data



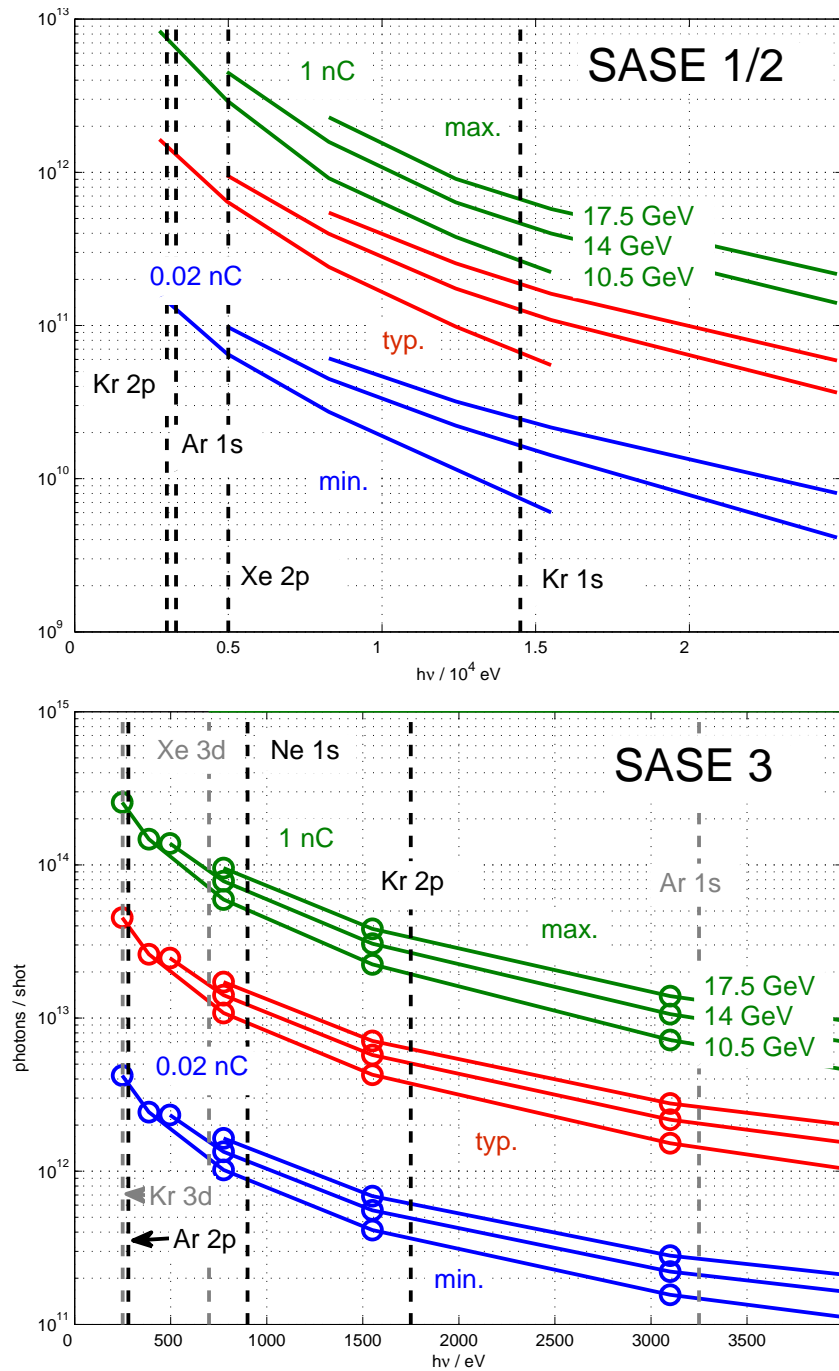
**Figure A.1:** Subshell photoionization cross sections for the rare gases in the range 0-1 500 eV (excerpt from [46]).



**Figure A.2:** Total photo-ionisation cross section of the rare gases for the complete energy range of all SASE beamlines (from [50]).



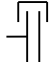




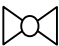











**Figure A.3:** Anisotropy parameter  $\beta$  for selected core levels of rare gases (data from [45]).



**Figure A.4:** Number of photons per pulse as a function of photon energy for SASE 1/2 (top) and SASE 3 (bottom); (Data from [29]).

# B Symbols used in vacuum technology

ducts & joints	valves	pumps
 vacuum chamber  flanged connection  clamped flange  bellow / hose  change in cross section	 general valve  gate valve  stop cock  right angle valve  variable leak valve  electro-magnetic valve	 general pump  turbomolecular pump  ion getter pump  Ti sublimation pump <b>gauges</b>  pressure gauge head  pressure gauge controller
Symbols comply with DIN 28401 („symbols in vacuum technology“)		

## C List of abbreviations

<b>BPS</b>	Beam protection system
<b>CF</b>	ConFlat flange
<b>COLTRIMS</b>	Target recoil-ion momentum spectroscopy
<b>CPS</b>	Counts per shot/second
<b>DESY</b>	Deutsches Elektronen-Synchrotron
<b>EtherCAT</b>	field bus system by Beckhoff Automation GmbH
<b>FEL</b>	Free-electron laser
<b>FLASH</b>	Free-electron laser in Hamburg
<b>FPGA</b>	Field-programmable gate array
<b>GUI</b>	Graphical user interface
<b>KF</b>	Kleinflansch, “Kwik flange”
<b>MCP</b>	Microchannel plate
<b><math>\mu</math>TCA</b>	“Micro-” Telecom computing architecture
<b>MPS</b>	Machine protection system
<b>OPIS</b>	Online photoionization spectrometer
<b>PEEK</b>	Polyether ether ketone
<b>PETRA</b>	Positron-electron tandem ring accelerator

<b>PLC</b>	Programmable logic controller
<b>RGA</b>	Residual gas analyser
<b>RHEED</b>	Reflection high energy electron diffraction
<b>SASE</b>	Self-amplified spontaneous emission
<b>ToF</b>	Time of flight
<b>TWINCAT</b>	Control software for the EtherCAT field bus
<b>UHV</b>	Ultrahigh vacuum
<b>VCR</b>	Pipe fitting system
<b>WP-73</b>	work package 73: X-Ray Optics and Beam transport
<b>WP-74</b>	work package 74: X-Ray Photon Diagnostics
<b>WP-75</b>	work package 75: Detector Development
<b>WP-76</b>	work package 76: Data Acquisition and Control
<b>XBPM</b>	X-ray beam position monitor
<b>XFEL.EU</b>	The European X-Ray Free-Electron Laser Project
<b>XGMD</b>	X-ray gas monitor detector

---

# Bibliography

- [1] M. Altarelli et al., "XFEL: The European X-Ray Free-Electron Laser - Technical Design Report",  
<http://xfel.desy.de/tdr/tdr/>.
- [2] A. Mancuso: "Conceptual Design Report: Scientific Instrument SPB", XFEL.EU TN-2011-007, in preparation.
- [3] A. Madsen: "Conceptual Design Report: Scientific Instrument SPB", XFEL.EU TN-2011-008. [http://www.xfel.eu/documents/technical\\_documents/](http://www.xfel.eu/documents/technical_documents/)
- [4] C. Bressler, "Conceptual Design Report: Scientific Instrument FXE", XFEL.EU TN-2011-005.  
[http://www.xfel.eu/documents/technical\\_documents/](http://www.xfel.eu/documents/technical_documents/)
- [5] M. Meyer, "Conceptual Design Report: Scientific Instrument SQS", XFEL.EU TN-2011-003.  
[http://www.xfel.eu/documents/technical\\_documents/](http://www.xfel.eu/documents/technical_documents/).
- [6] Frank Scholz, Sascha Deinert, Leif Glaser, Markus Ilchen, Jörn Seltmann, Peter Walter, and Jens Viefhaus, "The P04 Universal Diagnostic Unit for XUV and Soft X-Ray Radiation", DESY User Meeting (2011).
- [7] J. Viefhaus, "Online polarisation analysis via photoelectron spectroscopy at P09", DESY Annual Report 2009, p. 86.  
[http://hasylab.desy.de/e81/e245/e74812/e74816/infoboxContent74817/PhotonScience\\_2009-web\\_2010-01-05\\_Final\\_HB\\_eng.pdf](http://hasylab.desy.de/e81/e245/e74812/e74816/infoboxContent74817/PhotonScience_2009-web_2010-01-05_Final_HB_eng.pdf)
- [8] P04 beamline at PETRA III Online:  
[http://hasylab.desy.de/facilities/petra\\_iii/beamlines/p04\\_xuv\\_beamline/index\\_eng.html](http://hasylab.desy.de/facilities/petra_iii/beamlines/p04_xuv_beamline/index_eng.html)
- [9] J. Viefhaus, personal correspondence (2011).
- [10] G. Geloni, V. Kocharyan, E. Saldin, "Circular polarization control for the European XFEL in the soft X-Ray regime", internal report (2011).
- [11] P. Juranic, J. Viefhaus, S. Bonfigt, M. Ilchen, K. Tiedtke (DESY, Hamburg, Germany), M. Martins, L. Jahn, S. Klumpp (University of Hamburg, Hamburg, Germany), "Online Photoionization Spectrometer at FLASH", SRI Conference (2009).
- [12] P. N. Juranic, PhD Thesis.



- [13]J. Seltmann, Diploma thesis, DESY(2011).
- [14]J. Buck, PhD thesis, Christian-Albrechts-Universität zu Kiel (2010).
- [15]H. Sinn, personal correspondence(2011).
- [16]I. Witten and E. Frank, *Data mining: practical machine learning tools and techniques*, Morgan Kaufmann, San Francisco (2005).
- [17]V. Vapnik, *Statistical learning theory*, Wiley, New York (1998).
- [18]J. O'Rourke, *Computational Geometry in C*, Cambridge University Press (1994).
- [19]F. Aurenhammer, *Voronoi diagrams – A survey of a fundamental geometric data structure*, ACM Computing Surveys, **23**,345-405 (1991).
- [20]C. B. Barber, D.P. Dobkin, and H.T. Huhdanpaa, ACM Transactions on Mathematical Software **22**, 4, (1996).  
<http://www.acm.org/pubs/citations/journals/toms/1996-22-4/p469-barber/>
- [21]Homepage of the QHull project.  
<http://www.qhull.org/>
- [22]N. Nilsson, *Introduction to Machine Learning*, “An early draft of a proposed textbook”.  
<http://robotics.stanford.edu/~nilsson/mlbook.html>.
- [23]P. Gessler, personal correspondence (2011).
- [24]N. Kohlstrunk, List of beamline components at the European XFEL, internal document (19.12.2011).  
EDMS-No. D00000002629421,A,1,1
- [25]N. Kohlstrunk, “CAD Integration Guidelines for Photon Beamline Components”, XFEL.EU TN-2012-001-01 (2012).
- [26]M. Dommach, “UHV Guidelines for X-Ray Beam Transport Systems”, XFEL.EU TN-2011-004.  
<http://pubdb.desy.de/fulltext/getfulltext.php?uid=16928-44145>
- [27]Th. Tschentscher, “Layout of the X-Ray Systems at the European XFEL”, XFEL.EU TN-2011-001 (2011).  
<http://pubdb.desy.de/fulltext/getfulltext.php?lid=16925&fid=44125>
- [28]H. Sinn, J. Gaudin, L. Samoylova, A. Trapp, G. Galasso, “Conceptual Design Report: X-Ray Optics and Beam Transport”, XFEL.EU TN-11-002.  
<http://edmsdirect.desy.de/edmsdirect/file.jsp?edmsid=2081421>

- [29]E.A. Schneidmiller, M.V. Yurkov, "Photon beam properties at the European XFEL", XFEL.EU TN-2011-006.  
<http://pubdb.desy.de/fulltext/getfulltext.php?uid=17034-44650>.
- [30]J. Grünert et al., "Workshop on XFEL Diagnostics and Applications, 14-17 February 2010, Ryn, Poland. Report from WG I - Measurement of spatial profiles, wavefront, coherence" (2010).  
EDMS-No. D00000001786841,A,1,1
- [31]J. Grünert et al., "International Workshop on X-Ray Diagnostics and Scientific Application of the European XFEL 14-17 February 2010, Ryn, Poland Report from Work Group 2: Measurement of Spectral Properties" (2010).  
EDMS-No. D00000001786891,A,1,1
- [32]H. Sinn, "TGA requirements for SASE1 photon beamline".  
EDMS-No. D00000001516681,A,1,1
- [33]H. Sinn, "TGA requirements for SASE2 photon beamline".  
EDMS-No. D00000001516741,A,1,1
- [34]H. Sinn, "TGA requirements for SASE3 photon beamline".  
EDMS-No. D00000001516801,A,1,1
- [35]W. Decking, XFEL Lattice List 15.7.2011.  
EDMS-No. D00000001892711,F,1,1
- [36]J.Grünert, Proc. FEL09, Liverpool (2009).
- [37]J.Grünert, "CDR Framework Document: X-Ray Photon Diagnostics at the European XFEL", TR-2012-003 (2012).
- [38]C. Ozkan, "Imaging Station for Invasive X-Ray Photon Diagnostics at the European XFEL", TR-2012-004 (2012), in preparation.
- [39]W. Freund, Conceptual Design Description - K-Mono.  
EDMS-No. D00000001940181,B,1,3
- [40]J. Grünert, "Gas supply requirements for the X-Ray photon diagnostics along the beamlines of the European XFEL", Specification Document (2010).  
EDMS-No. D00000001786971,A,1,1.
- [41]J.Grünert, K.Tiedtke, A.Sorokin: "Considerations concerning the position of the XGMDs and XBPMs along the beamlines of the European XFEL", internal report, 02 SEP 2009.

- [42]K. Tiedtke et al., “X- Ray Gas Monitor Detector for the European XFEL”, Meeting Minutes (2011).  
EDMS-No. D00000002379531,A,1,1.
- [43]A.A. Sorokin, U. Jastrow, S. Bonfigt, and K. Tiedtke: “XGMD final design”, European XFEL / DESY Internal Report (2011).
- [44]K. Tiedtke et al.: “Gas detectors for X-Ray lasers”, J. Appl. Phys. 103, 094511 (2008).
- [45]A. DEREVIANKO, W. R. JOHNSON, and K. T. CHENG, Atomic Data and Nuclear Data Tables 73, 153-211 (1999).
- [46]J. J. Yeh and I. Lindau, Atomic Data and Nuclear Data Tables **32**, 1-155 (1985).
- [47]A. Thompson, I. Lindau, D. Attwood, P. Pianetta, E. Gullikson, A. Robinson, M. Howells, J. Scofield, K.-J. Kim, J. Underwood, K. Kirz, D. Vaughan, J. Kortright, G. Williams, and H. Winnick, *X-Ray Data Booklet*, Center for X-ray Optics and Advanced Light Source, Lawrence Berkeley National Laboratory.  
<http://xdb.lbl.gov/xdb.pdf>.
- [48]M. Ilchen et al., in preparation.
- [49]“XUV Photoionization Phenomena of Dilute Species / Joint German-Russian ‘Kick-Off’ Workshop” (2011).  
<https://indico.desy.de/conferenceDisplay.py?confId=3801>.
- [50]Physical Reference Databases of the National Institute of Standards and Technology (NIST).  
<http://www.nist.gov/pml/data/index.cfm>.
- [51]J. Graf, S. Hellmann, C. Jozwiak, C. L. Smallwood, Z. Hussain, R. A. Kaindl, L. Kipp, K. Rossnagel, and A. Lanzara, J. Appl. Phys. 107, 014912 (2010).
- [52]A. Pietzsch, A. Föhlisch, M. Beye, M. Deppe, F. Hennies, M. Naga-sono, E. Suljoti, W. Wurth, C. Gahl, K. Döbrich, et al., N. J. Phys 10, 033004 (2008).
- [53]M. Wellhöfer, J.T. Hoeft, M. Martins, W. Wurth, M. Braune, J. Viefhaus, and M. Richter, J. Inst. 3, 02003 (2008).
- [54]P. Radcliffe et al., Nucl. Instrum. Meth. A 582 (2-3), 516-525 (2007).
- [55]B. Schütte, S. Bauch, U. Frühling, M. Wieland, M. Gensch, E. Plönjes, T. Gaumnitz, A. Azima, M. Bonitz, and M. Drescher, “Evidence for chirped Auger electron emission”, submitted to Physical Review Letters (2011).
- [56]S. A. Sheinerman and V. Schmidt, J. Phys. B: At. Mol. Opt. Phys. 30, 1677-1690 (1997).

- [57]V. Schmidt, Rep. Prog. Phys. 55, 1483 (1992).
- [58]Cooper, J.W., Phys. Rev. A 47, 1841.
- [59]A. Bechler and R. H. Pratt, Phys. Rev. A 42, 6400 (1990).
- [60]J. H. Scofield, Phys. Rev. A 40, 3054 (1989); Phys. Scr. 41, 59 (1990).
- [61]M. Y. Amusia and N. A. Cherepkov, Case Studies in Atomic Physics (North-Holland, Amsterdam, 1975, Vol. 5, pp. 154-157.
- [62]J. Ullrich et al. Rep. Prog. Phys. 66 (2003) 1463-1545.
- [63]G. Geloni, V. Kocharyan, E. Saldin, Red Report (2011), DESY 11-096, <http://arxiv.org/abs/1106.1776>
- [64]G. Geloni, V. Kocharyan, E. Saldin, Red Report (2011), DESY 11-083, <http://arxiv.org/abs/1105.4783>
- [65]G. Geloni, V. Kocharyan, E. Saldin, Red Report (2011), DESY 11-009, <http://arxiv.org/abs/1101.4085>
- [66]G. Geloni, V. Kocharyan, E. Saldin, Red Report (2010), DESY 10-252, <http://arxiv.org/abs/1012.5154>
- [67]Y. Li, B. Faatz, J. Pflueger, Nucl. Instrum. Methods A 613 (2010) , 163-168
- [68]FLASH – Free-Electron Laser in Hamburg: Accelerator, <http://flash.desy.de/accelerator/>
- [69]Valeri, S., Liberi, M., & Verucchi, R. 1997, PRB, 56, 15272.
- [70]Guo, P., Ghebremedhin, A., Ariyasinghe, W. M., & Powers, D. 1995, PRA, 51, 2117.
- [71]Cooper, J. W., Southworth, S. H., MacDonald, M. A., & Lebrun, T. 1994, PRA, 50, 405.
- [72]Tulkki, J., Åberg, T., Mäntykenttä, A., & Aksela, H. 1992, PRA, 46, 1357.
- [73]Bonanno, A., Xu, F., Camarca, M., Siciliano, R., & Oliva, A. 1990, PRB, 41, 12590.
- [74]Colle, R., Fortunelli, A., & Simonucci, S. 1988, Nuovo Cimento D Serie, 10, 355.
- [75]Iketaki, Y., Takayanagi, T., Wakiya, K., Suzuki, H., & Koike, F. 1988, Journal of the Physical Society of Japan, 57, 391.
- [76]Huster, R., Sandner, W., & Mehlhorn, W. 1987, Journal of Physics B Atomic Molecular Physics, 20, L287.

- [77]Saiki, K., Rittaporn, I., & Tanaka, S. 1987, Japanese Journal of Applied Physics, 26, 45.
- [78]Vayrynen, J., Sodhi, R. N., & Cavell, R. G. 1983, jcp, 79, 5329.
- [79]Helenelund, K., Hedman, S., Asplund, L., Gelius, U., & Siegbahn, K. 1983, physscr, 27, 245.
- [80]Hedman, S., Helenelund, K., Asplund, L., Gelius, U., & Siegbahn, K. 1982, Journal of Physics B Atomic Molecular Physics, 15, L799.
- [81]Petrini, D. 1982, Canadian Journal of Physics, 60, 644.
- [82]Darko, T., Siegbahn, H., & Kelfve, P. 1981, Chemical Physics Letters, 81, 475.
- [83]Iwami, M., Kim, S. C., Kataoka, Y., et al. 1980, Japanese Journal of Applied Physics, 19, 1627.
- [84]Hanashiro, H., Suzuki, Y., Susaki, T., et al. 1979, J. Phys. B: Atomic & Molecular Pysics
- [85]Hanashiro, H., Suzuki, Y., Mikuni, A., et al. 1979, Unknown.
- [86]Hiraki, A., Kim, S. C., Imura, T., & Iwami, M. 1979, Japanese Journal of Applied Physics, 18, 1767.
- [87]Zehner, D. M. 1979, Journal of Vacuum Science Technology, 16, 562.
- [88]Hanashiro, H., Suzuki, Y., Mikuni, A., et al. 1979, Physics of Electronic and Atomic Collisions: ICPEAC XI, 28.
- [89]Asplund, L., Kelfve, P., Blomster, B., Siegbahn, H., & Siegbahn, K. 1977, physscr, 16, 268.
- [90]Howat, G., Åberg, T., Goscinski, O., et al. 1977, Physics Letters A, 60, 404.
- [91]Schumann, S., Groeneveld, K. O., Sevier, K. D., & Fricke, B. 1977, Physics Letters A, 60, 289.
- [92]Schneider, D., Johnson, B. M., Hodge, B., & Moore, C. F. 1976, Physics Letters A, 59, 25.
- [93]Krause, M. O. 1975, Physical Review Letters, 34, 633.
- [94]Johnson, B. M., Matthews, D. L., Smith, L. E., & Moore, C. F. 1973, Journal of Physics B Atomic Molecular Physics, 6, L369.
- [95]Matthews, D. L., Johnson, B. M., Mackey, J. J., & Moore, C. F. 1973, Physics Letters A, 45, 447.

- [96]Fastrup, B., & Larsen, G. A. 1971, Physics of Electronic and Atomic Collisions: ICPEAC VII, 392.
- [97]Krause, M. O. 1965, Physics Letters, 19, 14.
- [98]Körber, H., & Mehlhorn, W. 1964, Physics Letters, 13, 129.
- [99]M. Martins, M. Wellhöfer, A. A. Sorokin, M. Richter, K. Tiedtke, and W. Wurth, Phys. Rev. A 80, 023411 (2009)
- [100]A.A. Sorokin, S.V. Bobashev, K. Tiedtke and M. Richter, J.Phys.B 39, L299-L304 (2006)
- [101]A.A. Sorokin, M. Wellhöfer, S.V. Bobashev, K. Tiedtke, M. Richter, Phys. Rev. A 75, 051402(R) (2007)
- [102]A.A. Sorokin, S.V. Bobashev, T.Feigl, K. Tiedtke, H.Wabnitz and M. Richter, PRL 99, 213002 (2007)
- [103]P. Lambropoulos, P. Zoller, Phys. Rev. A 24, 379 - 397 (1981)
- [104]Takahashi, E., Kato, S., Okuda, I., & Matsumoto, Y. 2009, Applied Physics B: Lasers and Optics, 97, 511
- [105]Rossi, B., Badhress, I., Ereditato, A., et al. 2009, Journal of Instrumentation, 4, 7011
- [106]Zhang, H., Lu, Z., Fan, R., & Chen, D. 2009, Laser Physics, 19, 947
- [107]Stellpflug, M., Johnsson, M., Petrov, I. D., & Halfmann, T. 2003, European Physical Journal D, 23, 35
- [108]Martin, S., Denis, A., Ouerdane, Y., & Carré, M. 1992, Physics Letters A, 165, 441
- [109]Viefhaus, J. et al. PRL 80 (1998) 1618.
- [110]Prince, K.c., J. El. Spectr. 101-103 (1999) 141-147.
- [111]Lindblad, A., Fink, R. F., Bergersen, H., et al. 2005, jcp, 123, 211101 .
- [112]Becker, U., Prescher, T., Schmidt, E., Sonntag, B., & Wetzel, H.-E. 1986, pra, 33, 3891 .
- [113]Shirley, D. A., Kobrin, P. H., Lindle, D. W., et al. 1982, X-Ray and Atomic Inner-Shell Physics, 94, 569 .
- [114]Hoefler, U., Breitschaffer, M. J., & Umbach, E. 1990, Physical Review Letters, 64, 3050 .

- [115]Gadzuk, J. W., Holloway, S., Mariani, C., & Horn, K. 1982, Physical Review Letters, 48, 1288 .
- [116]G. King, F. Read, M. Tronc, Chem. Phys. Lett. 52 (1977) 50.
- [117]W.C. Stolte et al., J. Phys. B: At. Mol. Opt. Phys. 30 (1997) 4489.
- [118]O.-P. Sairanen et al., Rev. Sci. Instrum. 66 (1995) 1621.
- [119]A. Ausmees, S. J. Osborne, R. Moberg, S. Svensson, S. Aksela, O.-P. Sairanen, A. Kivimäki, A. Naves de Brito, E. Nommiste, J. Jauhiainen, and H. Aksela, Phys. Rev. A 51, 855 (1995).
- [120]Adriano Filipponi 2000 J. Phys. B: At. Mol. Opt. Phys. 33 2835.
- [121]Krause M O and Oliver J H 1979 J. Phys. Chem. Ref. Data 8 329.

---

# Acknowledgement

The development of this conceptual design report would not have been possible without the support of the following people and groups:

- Our special thanks go to Jens Viefhaus and his work group at PETRA III (DESY) — Leif Glaser, Frank Scholz, Markus Ilchen, Sascha Deinert, Jörn Seltmann, and Peter Walter — for sharing their design, experience, and infrastructure and for many fruitful discussions during this early stage of development.
- The author wants to thank his co-workers in WP-74: X-Ray Photon Diagnostics — Jan Grünert, Wolfgang Freund, Cigdem Ozkan, and Bin Li — for valuable support and discussions during the refining process of numerous ideas and approaches during the past year.
- We appreciate the valuable feedback we obtained during the review process, especially during the review meeting, of this conceptual design report. Especially the assessment by the internal and external reviewers and stakeholders — Markus Braune (DESY), Patrick Geßler (WP-76), Michael Martins (University of Hamburg), Michael Meyer (WP-85), Harald Sinn (WP-73), and Christopher Youngman (WP-76) — is highly acknowledged and provides us excellent input for the ongoing development process.
- We would like to thank the colleagues from WP-76, especially Christopher Youngman and Nicola Coppola, for good collaboration in the wide field of beamline control and data acquisition.
- We thank the members of WP-73, among them Harald Sinn and Martin Dommach, for good discussions on various topics concerning standards, location of our devices, etc.
- We thank Patrick Geßler for giving his advice during discussion of digitizer and FPGA requirements.



- We acknowledge Kurt Ament for assistance in formatting and proofreading this manuscript. His style guide gave valuable answers in many difficult situations.
- We acknowledge Dirk Rathje for implementing the  $\LaTeX$  template used for this document and for valuable support during its beta-testing phase.
- The work of WP-74 is carried out under the responsibility of Serguei Molodtsov, Scientific Director and member of the Management Board of the European XFEL.
- Part of this work was supported by the Pre-XFEL grant.
- We acknowledge the financial support by the European XFEL GmbH and its international shareholders.

